DOCTORAL SCHOOL
MEDITERRANEA UNIVERSITY OF REGGIO CALABRIA

INGEGNERIA DELL'INFORMAZIONE, DELLE INFRASTRUTTURE
E DELL'ENERGIA SOSTENIBILE
(DIIES)

PhD IN
INFORMATION ENGINEERING

S.S.D. ING-INF/01
XXVI CYCLE

RADIO FREQUENCY AND SOLAR ENERGY HARVESTING SYSTEMS FOR ULTRA LOW POWER SENSORS

CANDIDATE
Domenico PAVONE

ADVISORS
Prof. Francesco DELLA CORTE

Dott. Michele D'URSO

COORDINATOR
Prof. Claudio DE CAPUA

REGGIO CALABRIA, FEBRUARY 2015

Finito di stampare nel mese di **Febbraio 2015**

Edizione CSdA Centro Stampa d'Ateneo

Collana *Quaderni del Dottorato di Ricerca in Ingegneria dell'Informazione*
Curatore *Prof. Claudio De Capua*

ISBN

Università degli Studi *Mediterranea* di Reggio Calabria
Salita Melissari, Feo di Vito, Reggio Calabria

Domenico Pavone

RADIO FREQUENCY AND SOLAR ENERGY HARVESTING SYSTEMS FOR ULTRA LOW POWER SENSORS

The Teaching Staff of the PhD course in
INFORMATION ENGINEERING
consists of:

Claudio DE CAPUA(coordinator)
Raffaele ALBANESE
Francesco BUCCAFURRI
Salvatore COCO
Francesco DELLA CORTE
Domenico GATTUSO
Giovanna IDONE
Antonio IERA
Tommaso ISERNIA
Andrea MORABITO
Giovanni LEONE
Massimiliano MATTEI
Francesco Carlo MORABITO
Francesco RUSSO
Riccardo CAROTENUTO
Antonella MOLINARO
Maria Nadia POSTORINO
Francesco RICCIARDELLI
Domenico URSINO
Mario VERSACI
Giovanni ANGIULLI
Giuseppe ARANITI
Giacomo CAPIZZI
Rosario CARBONE
Sofia GIUFFRÈ
Fabio LA FORESTA
Gianluca LAX
Roberta NIPOTI
Valerio SCORDAMAGKIA
Lorenzo CROCCO
Mariantonia COTRONEI
Fortunato PEZZIMENTI
Giuseppe MUSOLINO
Domenico ROSACI
Giuseppe RUGGERI
Giuseppe SARNÈ
Ivo RENDINA
Lubomir DOBOS

A mia moglie Merirosa:
colonna portante della mia vita.
Senza di lei, oggi,
non sarei quello che sono diventato!

Acknowledgments

This thesis would not have been possible without the help and support of many people to whom I would like to express my gratefulness.
I would like to thank my advisors Prof. Francesco Della Corte and Dott. Michele D'Urso for their scientific guidance and support during these years.
I am very grateful to all the group of "Innovative Solutions, Applied Electromagnetism & Siting" SELEX-Electronic Systems, Naples (Maurizio, Gabriella, Flavio; Marcello, Aniello, Giancarlo, Pietro and Roberto) for their help and encouragement, especially during the writing of this work.
Moreover, I am also grateful to all colleagues of the Consortium Optel–Naples (Salvatore and Francesco)
Finally, I am deeply thankful to my family for their support and encouragement over these years.

Contents

List of Figures

List of Tables

1
Introduction

1.1 Motivation

Energy harvesting (also known as energy scavenging) is the process of generating electrical energy from environmental energy sources, such as electromagnetic energy, kinetic energy, or thermal energy. The term has been frequently applied in the context of small autonomous devices such as the nodes of a wireless sensor network..

Wireless sensor network (WSN) is an emerging wireless technique which have drawn many research interests over last decades. This has been used in diverse fields, employing a number of sensor nodes for environmental sensing (temperature, pressure, humidity, etc.) and monitoring (structural, health, etc.). Battery is a traditional option to supply power for remote devices.

Depending on the application, battery can support the remote devices for a certain life-time. Recharging or changing the battery is a repeated maintenance work which is quite human-resource consuming, being even impossible for devices located in places hard to be reached. Therefore, energy autonomous sensor nodes has been proposed.

With the aid of the auxiliary energy transducers, the remote device is able to harvest the power from the ambient/dedicated energy source, such as solar and Radio Frequency (RF) waves, to self-support the communication with other nodes for a lifetime unlimited by the battery capacity.

Energy sources have been explored since years, and energy transducers have been designed for various sources. Hybrid energy harvesting systems, which aim to utilize different energy sources in one remote device, are proposed to supplement the single ambient energy source, the strength of which is limited by the environmental situation, e.g. no sunshine available during night. Energy source like dedicated RF radiation is a promising option when ambient energy sources are insufficient.

1.2 Research Objectives

A possible solution to the problems outlined above is the use of a multi-sources energy harvesting architecture which is presented in figure 1.1. In particular, the Ultra Low Power (ULP) wireless sensor gas [1] and temperature [2] were selected as wireless sensor node.

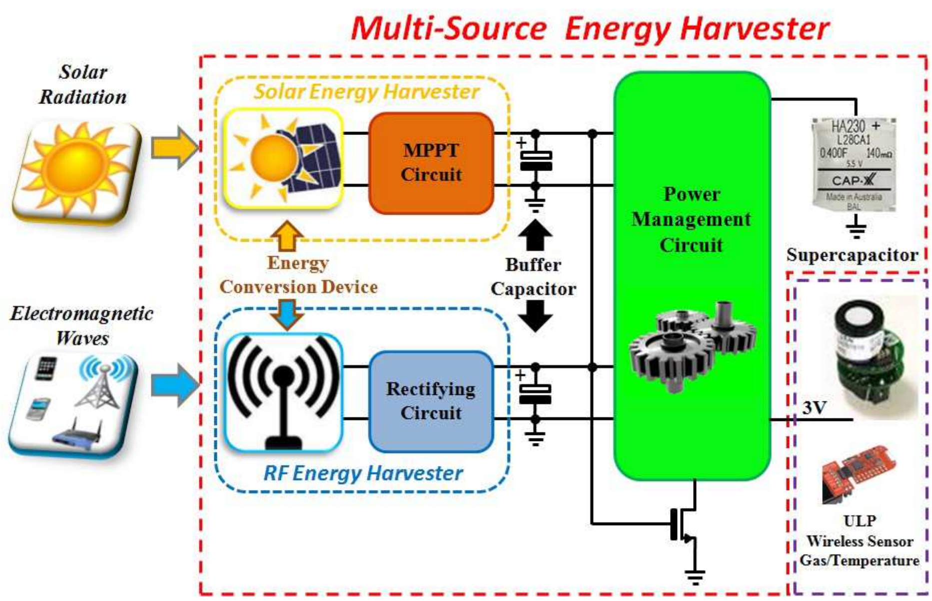

Fig. 1.1 Multi-source energy harvesting architecture.

This architecture is composed mainly of the two harvester circuit (one relating to Solar Energy Harvesting (SEH), the other to RF Energy Harvesting (RFEH)) and the power management circuit which is responsible to manage the energy previously recovered. Also, there is a supercapacitor, which, once loaded from power management, has to feed the wireless senor node when the energy sources references are not present. This capacitor is loaded when there is a surplus of energy, that is when the sensor is inactive and at same time it is possible to harvest energy by means of harvester circuits.

The goals of this work are to improve the RF energy harvesting efficiency RF/DC using a new wideband rectifier topology (in this way it is possible to harvest energy from many RF sources), to maximize the output power of the small solar cells by MPPT circuit, and to manage the total power harvested in order to supply the sensor node by means of power management circuit and supercapacitor.

1.3 Thesis Outline

This Thesis is organized as explained below. The Thesis structure is also shown in Figure 1.2.

An overview of wireless sensor networks is given in Chapter 2, where limitations of battery operated sensor nodes and energy reservoirs are given. Moreover, feasible energy harvesting techniques for wireless sensor node applications are covered.

In Chapter 3, the wideband RF energy harvesting system is presented. In particular, a flexible meta-material inspired antenna and a new multi-band rectifier topology is proposed as *rectenna* (antenna with the rectifier circuit).

In Chapter 4, solar energy harvesting is discussed highlighting photovoltaic fundamentals, maximum power point tracking and the architecture used for the Solar Energy Harvesting.

Chapter 5 reviews the hybrid power management system architecture, design and performance. Starting from this analysis, the prototype has been realized and evaluated empirically.

Finally, in Chapter 6, conclusions and future recommendations are presented.

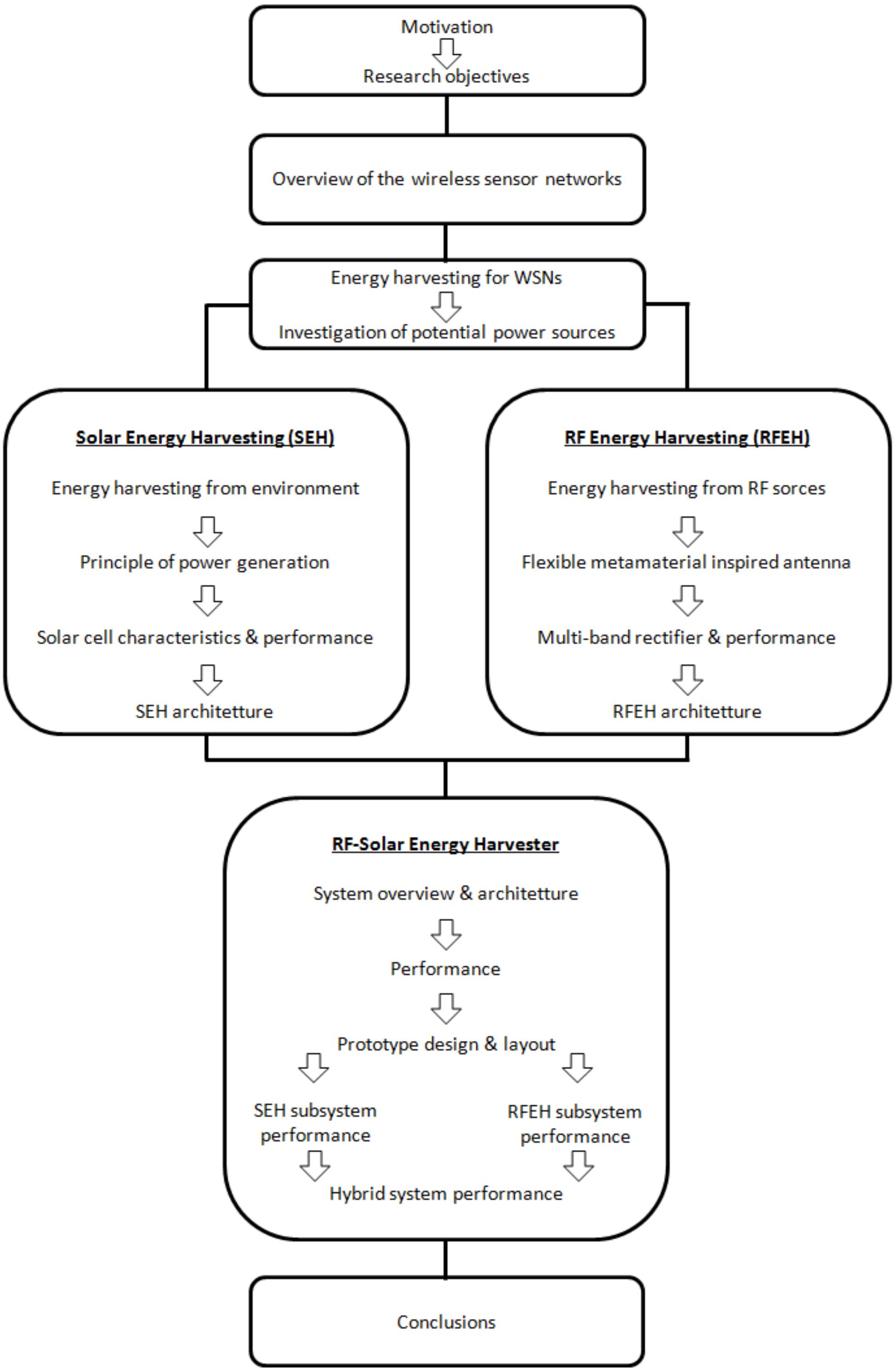

Fig. 1.2 Thesis structure.

2
Energy Harvesting for Wireless Sensor Networks

A Wireless Sensor Network (WSN) is a network that contains sensors nodes that work together to monitor physical or environment conditions linked by wireless connections. The operating lifetime of WSN is a crucial design parameter. It is possible increase the autonomy of the nodes introducing the specific energy transducers able to harvest energy from surroundings.

The extension of the battery lifetime is the most critical challenge concerning the implementation of WSNs. This problem is more crucial for all applications where the periodical node battery replacement is impractical or difficult. Several works have been addressed to the design of autonomous sensor nodes, extending of the battery lifetime thanks energy harvesting system [3-15].

In this chapter, energy harvesting solutions to resolve the problematic of lifetime battery of the WSN are discussed.

2.1 Outline of Wireless Sensor Networks

A WSN is a network consisting of low power and small sensors, linked by wireless connections, that allow to monitor and control of the particular surroundings from remote locations.

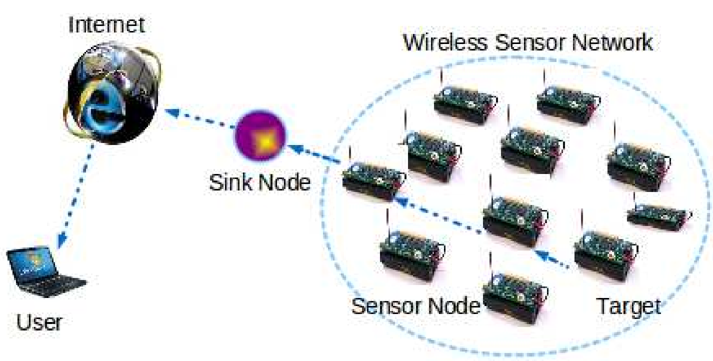

Fig. 2.1 Wireless sensor network.

These wireless sensing devices are called wireless sensor motes [16] and each of them has the limited processing capabilities.

The design of autonomous WSNs requires both the minimization of the power consumption of the node hardware and a power management strategies. The ability to operate with a generic infrastructure, is one of the main advantages. In fact, the WSN have the capability to send data from remote and inaccessible locations not requiring infrastructure such as mains power. A sensor node is composed of four parts: sensing unit, processing unit, transceiver unit and a power unit [17].

It is possible to note in figure 1.1 that, the node information is sent to sink node through the RF transceiver unit. The power unit contains a power storage unit (battery or supercapacitor) and a power management circuitry which has the task to manage and to improve the energy needed of the node. To power up a sensor node, a energy storage device like battery can be used to extend the lifetime of the node. Since the battery have a finite energy density or power density, the maximum lifetime of the sensor node can be achieved is one year. Unfortunately, with a limited battery capability, the sensor node can communicate only limited distance.

2.2 Significance of energy harvesting for WSNs

In order to extend the lifetime and to improve the energy autonomy of the wireless sensor nodes, energy harvesting techniques are investigated. The energy harvested is used to recharge the energy storage device as battery or supercapacitors of the sensor node.

Potential energy sources from the ambient environment are: sunshine, vibration, heat, wind, RF waves etc. For different energy sources corresponds different energy harvester transducer (solar panel, antenna, Seebeck thermal-electrical generator, piezoelectric) that converting harvested power to electricity able to supply sensor nodes.

Figure 1.2 shows the approximate amount of energy per unit available from four micro-harvesting sources.

Energy Source	Harvested Power
Vibration/Motion	
Human	4 μW/cm^2
Industry	100 μW/cm^2
Temperature Difference	
Human	25 μW/cm^2
Industry	1–10 mW/cm^2
Light	
Indoor	10 μW/cm^2
Outdoor	10 mW/cm^2
RF	
GSM	0.1 μW/cm^2
WiFi	0.001 mW/cm^2

Fig. 2.2 Energy harvesting estimate [18].

In order to realize sensor node self-sustained, techniques of the energy harvesting were examined. Various feasible energy harvesting methods for sensor nodes already exist as reported in [19-22].

For the WSM battery- powered, the task of the power management is to minimize energy consumed [23] but introducing energy harvesting system for each sensor node, the operating life sensor can be extended reducing also the energy demand from the battery.

2.3 Energy storage

Energy storage plays an important role in energy harvesting applications. An important parameter for all energy storage systems is the storage capacity. The storage capacity refers to the amount of energy that can be stored [24]. Common energy storage devices are batteries and fuel cells. On the market exist different type of energy storages, e.g. zinc–carbon, alkaline, nickel metal hydride (NiMH), and lithium-ion (Li-ion), capacitors, and supercapacitors

Supercapacitors are a unique promising new technology that feature a combination of relatively high energy density with high power density. As seen in figure 1.3, supercapacitors offers a compromise between the positive characteristics of both batteries and standard capacitors.

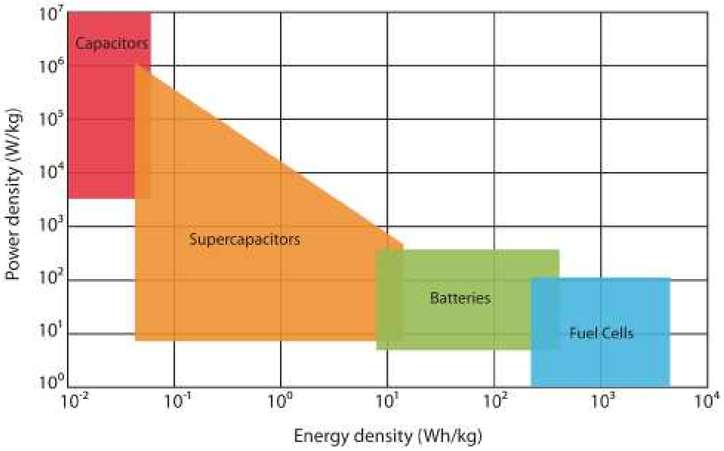

Fig 2.3 Power vs energy for various energy reservoirs redrawn from Cap-XX [25].

2.3.1 Supercapacitors

Supercapacitors, have similar characteristics to normal capacitors. The main difference is that the supercapacitor present higher capacitance values for volume unit while the energy is stored in the same way as in conventional capacitors [26]. Moreover, they store electric charge without involving the chemical reaction of a traditional battery that allows to reduce the environmental pollution due to the chemical waste.

Their energy density is typically hundreds of times greater than conventional electrolytic capacitors. They also have a much higher power density than batteries or fuel cells.

Figure 2.4 shows the comparison between a conventional capacitor (1mF) and supercapacitor (220mF). The physical size advantage is evident.

Fig. 2.4 Physical size advantage of supercapacitors.

Due to porosity characteristic of conductive plates area, the supercapacitor presents high surface area and then high capacitance value.

The stored energy is a function of the capacitance and voltage potential across the conductive plates. The energy stored in a supercapacitor can be calculated using equation (2.1) [27].

$$E = \frac{1}{2} C V^2 \tag{2.1}$$

where:

E = energy available in supercapacitor (joule)

C = capacitance of the supercapacitor (farad)

V = steady-state potential across conductive plates (volt)

Capacitors and supercapacitors have the same characteristics, but they are different from batteries rechargeable in the charged and discharged operation.

Moreover, for the batteries rechargeable, the potential across the plates, a cell voltage of a battery is chemically defined and then the voltage, during charge and discharge cycles, is constant. The voltage across a capacitor increases and decreases linearly with respect to the charge across the conductive plates [26].

Figure 2.5 shows the different charge and discharge characteristics for a capacitor and a rechargeable battery.

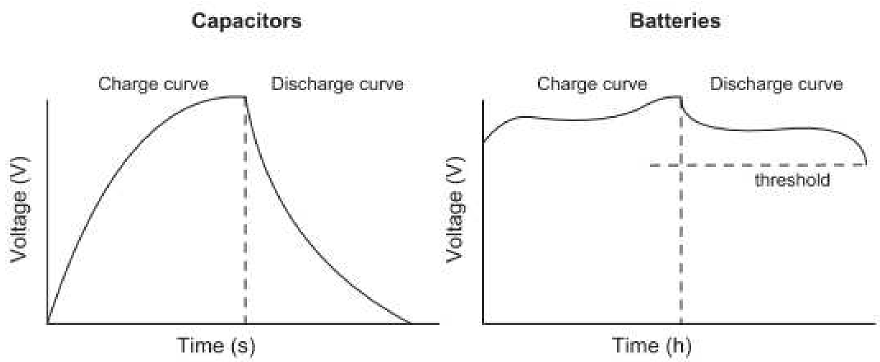

Fig 2.5 Charge and discharge characteristics redrawn from [26].

2.4 Energy harvesting systems

Thanks to the introduction of energy harvesting techniques for WSNs, sensor nodes could become self-sustained thus being only limited by the failure of their own hardware and not by the energy source .

Energy harvesting means that the sensor node converts the energy available in its environment into usable electricity to supply itself [28] More in detail, an energy harvesting system is a system designed to match the variable power output of the energy source to the inconsistent power demand from the load by collecting, converting and storing energy. An energy harvesting system, in fact, has an energy storage reservoir such as a rechargeable battery or supercapacitor to collect the harvested energy.

Typical energy harvesting system architecture is sketched in figure 2.6: the first block is the component responsible of the energy harvesting; then the harvested energy arrives at boost converters that scale up the voltage; finally the battery management systems stores the energy that is in this way converted into a useful and regulated form, thus being suitable for many small electronic and mobile applications [29].

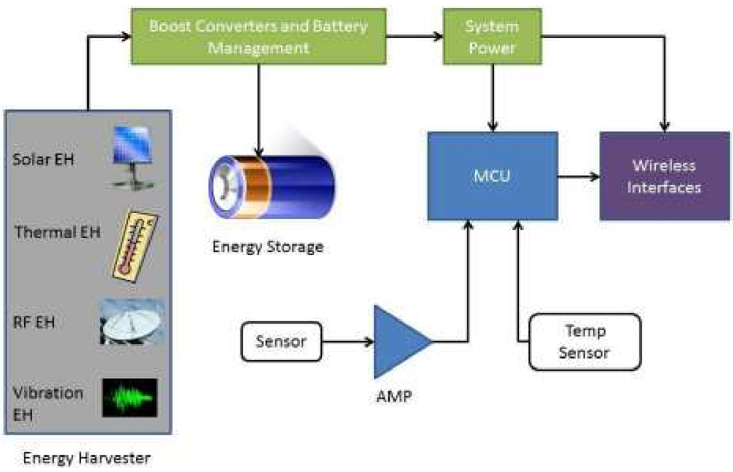

Fig. 2.6 Energy harvesting systems diagram.

Energy harvesting systems can be grouped into three categories according to the type of energy they use, which may be kinetic, thermal or electromagnetic (including both solar and RF radiation).

2.4.1 Kinetic energy

Kinetic energy is transformed to electrical energy by means of electrostatic, piezoelectric or electromagnetic mechanisms that convert the displacement of a moving part or the mechanical deformation of some structures inside the energy harvesting module. In electrostatic transducers, the distance or overlap of two electrodes of a polarized capacitor changes due to the movement or the vibration of a movable electrode. This motion produces a voltage change across the capacitor and results in a current flow in an external circuit.

In piezoelectric transducers, vibrations or movement cause the deformation of a piezoelectric capacitor thereby generating a voltage [30].

In electromagnetic transducers, the relative motion of a magnetic mass with respect to a coil causes a change in the magnetic flow. This generates an AC voltage across the coil [31]. The piezoelectric mechanism allows to obtain the most efficient conversion.

Thanks to recent advances in MEMS technology the piezoelectric-based energy harvesting systems have been miniaturized, this making them usable in the WSNs context [31-32].

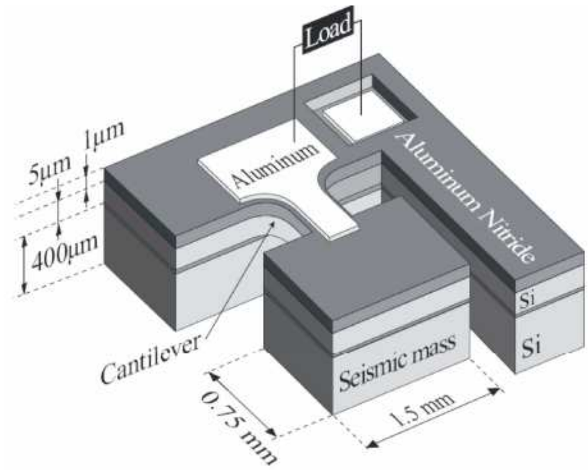

Fig. 2.7 Schematic of a piezoelectric micro-power generator [32].

2.4.2 Thermal energy

A thermoelectric generator basically is formed by a thermocouple, consisting of a p-type and n-type semiconductor connected electrically in series and thermally in parallel. The temperature difference between the cold and hot junctions is proportional to the electrical current produced (by the Seebeck effect). An electrical load is then connected in series with the thermo-generator, thus creating an electric circuit [28]. Bi_2 Te_3 is the most widely used material for the fabrication of thermoelectric generators, at room temperature. Poly-SiGe has also been used, especially for micro-machined thermopiles [33]. Moreover, research on nano-structured materials is ongoing worldwide in order to optimize thermoelectric generator performance.

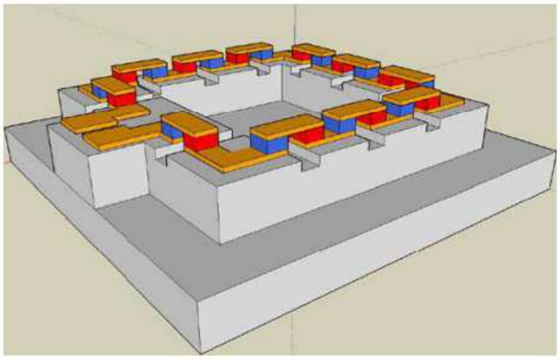

Fig. 2.8 Micro-machined thermopile [33].

2.4.3 Electromagnetic energy

Electromagnetic radiation is an interesting energy source, either in the form of light (known as solar energy), or lower frequency RF radiation. Both methods are extensively used in many present devices. Solar energy is a mature technology. Photovoltaic systems are found from the megawatt to the milliwatt range, being used in a wide range of applications. Outdoor they are a viable energy source for self-powered systems, while indoor the illumination levels are much lower (10-100 $\mu W/cm^2$). In this case, in fact, a higher sensitivity is required, given the lower level of illumination, that means a fine-tuning of the cell design to the different spectral composition of the light. RF energy harvesting systems overcome such limitation [34]. Indeed, RF power can be easily provided when needed, in every location. RF harvesting systems, in fact, rely on a RFID-like approach: the power is delivered to passive tags through the radio waves transmitted by a reader. This solution gives makes the RF-powered devices to be located in inaccessible or hazardous areas, or, more in general, in locations where battery replacement is highly impractical, thus giving great flexibility to these kind of systems.

2.4.3.1 Solar based energy harvesting

Solar cells have been used to power electronic systems, converting solar energy into electricity, for decades.

Even if light intensity varies dramatically due to the 24 hour solar cycle and cloud cover and to the location on the earth’s surface (longitude and latitude), the gap between indoor irradiance and outdoor lighting still remains large, ranging from a few mw/cm^2 for indoor cell to hundreds of mw/cm^2 for outdoor solutions [35].

The most relevant problem to be solved in harvesting efficiency is the Maximum Power Point Tracking (MPPT) that is impedance matching between the supply and the source at runtime [36].

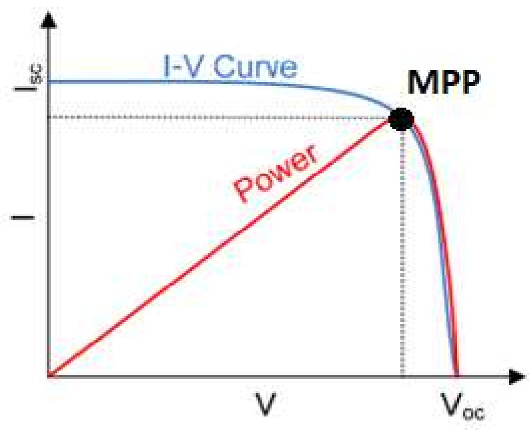

Fig. 2.9 Maximum power point of a photovoltaic module.

The impedance of a solar panel is primarily a function of the sunlight intensity and the current, and to a lesser extent of temperature and other factors. For a given level of light intensity, the maximum power point (MPP) is the point that maximizes the power output on the I-V curve depicted in figure 2.9. There are several academic prototypes that use photovoltaic cells for embedded systems; more recently, some solutions have been found also for wireless sensor nodes [37-43].

2.4.3.2 Radio Frequency based energy harvesting

This technique is based on the recovery of the energy contained in the RF fields generated by sources of opportunity like TV towers, wireless radio networks and cell phone towers [44-49]. Conceptually, this energy is captured and converted into functional DC voltage by using specialized circuits directly connected to the receiving antenna.

Although the energy intensity is lower compared to other energy harvesting systems, RF energy harvesting systems have many attractive features. Such systems can be used in any location where there is a dedicated transmitter, thus not depending anymore on time of the day, geographical aspects of the region, weather conditions etc., which must be considered in other examples of energy harvesting systems above mentioned (including solar, and wind energy). Figures 2.10 demonstrate the principle and architecture of RF energy harvesting systems.

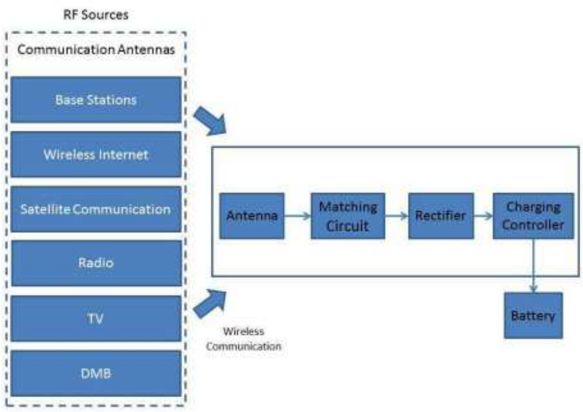

Fig. 2.10 RF energy harvesting system architecture.

Powercast company, uses the energy from a dedicated transmitted RF signal to supply wireless sensor nodes. The transmitter can be placed everywhere, in any device thus sending a low, continuous signal to small gadgets containing an embedded receiver [50].

3

Wideband Radio Frequency Energy Harvesting System

Object of this chapter is the sizing and design of a circuit for the recovery of energy from radio frequency sources present in the environment (GSM1800, UMTS, Wi-Fi or Bluetooth). The advantages of using this type of source are related to the type of wireless sensor (or sensor network) that it possible to supply. In particular, the sources of radio frequency are a source of energy potentially available throughout the day, both outdoor and indoor. Given the low power that can be recovered, these techniques will be developed for WSN-ULP (Wireless Sensor Network - Ultra Low Power) systems that use a RF Energy Harvesting system that converts the radio frequency electromagnetic energy available in the environment into an electrical quantity in order to self-feed the same WSN.

3.1 Introduction

There is an increasing need for highly distributed ambient-embedded systems, integrating wireless communication and sensing functionalities, autonomous from the power supply point of view. For power needs of the order of few μW, this can be accomplished by integrating harvesting systems able to receive available RF power from wireless applications [51-54]. To this aim, the RF receiver should be highly versatile with respect to both the operating frequency and the RF power range.

The Friis equation (3.1) relates the received (P_r) and transmitted (P_t) powers with the distance R as:

$$P_r = P_t G_t G_r \left(\frac{\lambda}{4\pi R}\right)^2 \tag{3.1}$$

where G_t and G_r are antenna gains, and λ is the wavelength of the transmitted signal.

As shown by equation 3.1, the received power is inversely proportional to the square of the distance from the source. More precisely, this is true in "line of sight" and, in realistic scenarios, the distance dependence is even more constraining in terms of received power.

The following tables indicate the main electromagnetic sources and the relative power density available in the input RF energy harvesting architecture (before the conversion to DC) for outdoor-indoor applications [55].

50 kW AM RADIO STATION	
Distance	***Density Power Available***
5 Km	159 μW/m²
10 Km	40 μW/m²

Tab. 3.1 Density power available for the 50 KW AM Radio Station.

100 W GSM BASE STATION	
Distance	***Density Power Available***
100 m	800 μW/m²
500 m	32 μW/m²
1000 m	8 μW/m²

Tab. 3.2 Density power values available for the 100 W GSM Base Station.

0.5 W MOBILE PHONE	
Distance	***Density Power Available***
1 m	40 mW/m²
5 m	1.6 mW/m²
10 m	0.4 mW/m²

Tab. 3.3 Density power available for the 0.5 W Mobile Phone.

1W Wi-Fi ROUTER	
Distance	***Density Power Available***
1 m	80 mW/m²
5 m	3.2 mW/m²
10 m	0.8 mW/m²

Tab. 3.4 Density power available for the 1 W Wi-Fi Router.

The efficiency of an RF energy harvesting system η is defined as the ratio between the harvested power (P_{dc}) and the received power (P_r) as seen in equation 3.2.

$$\eta = \frac{P_{dc}}{P_r} \times 100 \tag{3.2}$$

In order to get high efficiency from the energy harvester, the rectifier circuit needs to be carefully designed by considering all its input parameters. Generally, the power conversion efficiency depends on many design parameters: load condition, input power level, number of stages, etc. [56-57].
The energy recoverable from electromagnetic sources is limited by the existing law that on the one hand protects the health of citizens, on the other hand minimizes the maximum transmitted power of the electromagnetic sources. In particular, the Italian law DPCM of 8 July 2003 fixes the limit values of the EM radiations to 1W/m^2 between 3MHz and 3GHz [58] reducing thus the energy available in the environment.

Of course, the use of wideband architectures can overcome such limitations, thus maximizing the harvested energy.
For these reasons, a wideband system architecture based on radiofrequency energy harvesting, able to recover energy from available RF electromagnetic sources to power wireless sensor nodes is presented.

3.2 Wideband RF Energy Harvester

The RF Energy harvester shown in figure 1.1 is the revision of a previous architecture (see figure 3.1) which has been designed to work at three different frequencies: GSM1800, UMTS and Wi-Fi. In fact, in order to do this it was necessary to design each rectifier circuit at a different frequency and adapt, by means of a matching network, the impedance of the antenna. Finally, the outputs of the individual rectifier circuits, were linked together to be able to sum, with a certain efficiency, the "single" powers harvested from each circuit by means of a DC combining circuit.
Despite this architecture would present a good efficiency of rectification, it had the disadvantage that the individual channels (each consisting of the rectifier circuit and the matching circuit for a single frequency) were not perfectly separated between them. In this way, the matching network of a single channel depended also on the state (active or inactive) of the remaining circuits. This drawback has been overcome by using a single matching network which can, together with three different inductors (the number of

the inductors derives from how many rectifier circuits we want to adapt to the individual frequencies) to match the impedance of the antenna to the single circuit rectifier multi-band impedance. This architecture is shown in Fig. 3.2.

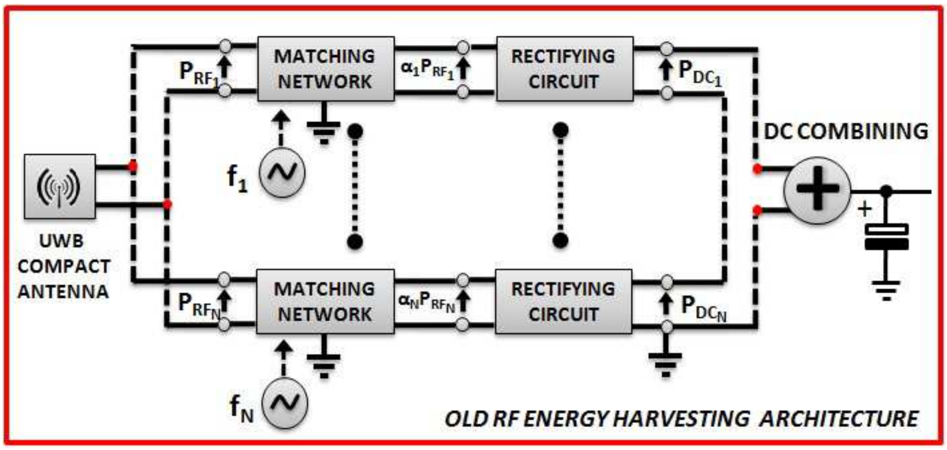

Fig. 3.1 Old wideband RF energy harvesting architecture.

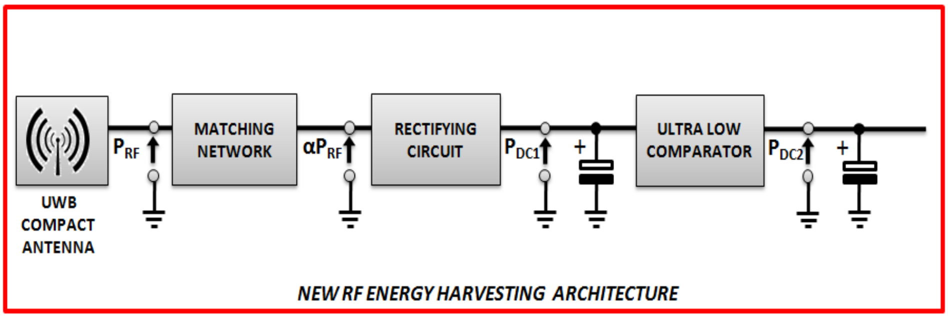

Fig. 3.2 New wideband RF energy harvesting architecture.

Now we analyze in detail the building blocks of the architecture showed in figure 3.2.

3.3 Wideband RF Energy Harvesting Components

The building blocks of the new wideband RF energy harvesting architecture, as showed in figure 3.3, are mainly three: the antenna, the rectifying circuit and finally the power matching network which has the aim to adapt the impedance between the antenna and the rectifying circuit.

As mentioned earlier, the new approach to RF energy harvesting circuit design proposed in this work is based on the voltage rectifier circuit. In this subsection, we explain how to select the components of voltage rectifier and the power matching network according to the constraints posed by the load, and also how the components of circuit influence the efficiency and performance of the circuit.

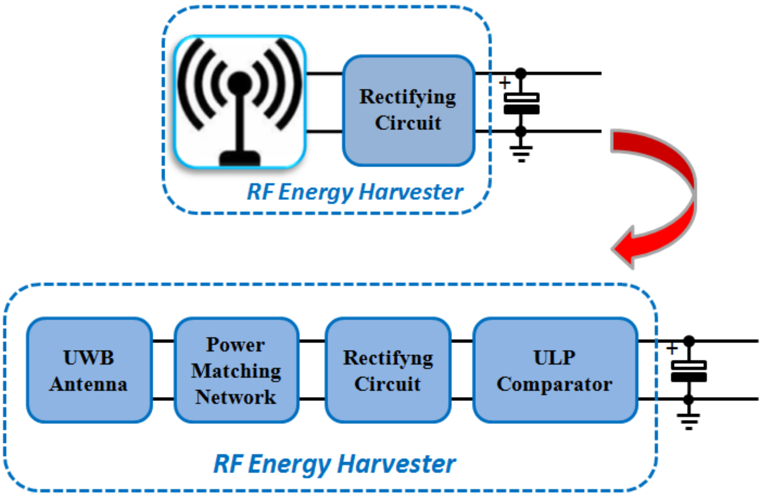

Fig. 3.3 Building blocks of the wideband RF harvester.

The analysis begins with the design of a new type of antenna, based on the concept of metamaterials (MTMs).

3.3.1 Flexible Metamaterial-Based Wideband Antenna

In the RF Energy Harvesting system, in order to minimize the overall dimensions, it is necessary to use an electrically small antenna. In this thesis, the antenna has been designed to fulfil emerging wireless technology requirements related to the working bandwidth (in our case [1700, 2500] MHz, including GMS, UMTS and Wi-Fi), and to the overall antenna dimension (to be reduced as much as possible). To this aim, the small antenna has been designed according to the recent MTM-inspired concepts [59]. As well known, an electrically small antenna is an inefficient radiator, due to its very small radiation resistance and very large capacitance reactance, with a large impedance mismatch to any realistic power source. The main idea, coming from [59] and herein applied, is to achieve resistive and reactive matching without using effective MTM medium, but with an element such as an inclusion that could be used in MTM unit cell to realize an epsilon-negative (ENG), mu-negative (MNG) or double-negative (DNG) medium [59-61].

The result is a very efficient electrically small antenna, easy to realize, easy and inexpensive to build, derived by applying MTM concepts, but that in reality consists of a regular antenna just loaded with the elements mentioned before. Innovative layouts of printed antennas based on transmission-line MTMs have been recently reported [60-61].

3.3.1.1 Metamaterial Inspired Antenna Design and Simulations

The proposed antenna has been designed according to the MTM concept of phase compensation [59], obtained through a series capacitive loading and a shunt inductance. The first one is achieved by using an interdigited capacitance along the body of the monopole, while the shunt inductance is obtained by properly adding a strip totally running around the monopole, connecting the monopole to the ground plane. It has been demonstrated that, for the typology of the MTM called "planar MTMs", the permittivity and the permeability of the material can be represented respectively by a capacitance and an inductance [62]. In this way, a "planar MTM" can be modeled using a loaded transmission-lines in printed technology and the electromagnetic behavior is dominated by a shunt inductance and a series capacitance [63].

A transmission line is considered as an ordered repetition of unit-cells, but it has been demonstrated that a single unit-cell of "planar-MTM" can be sufficient to obtain the phase compensation in printed monopoles [64]. The use of the phase-compensation law allows to reduce the antenna size [59]. The main concept is that the phase of a wave propagating in a DNG material reversed (the Poyinting's vector is anti-parallel to the wave vector) compared to the case of a wave propagating in a conventional material. In this way, it is always possible to combine the two materials so as to apply and satisfy the phase-compensation law. This theoretical result has been successfully applied to design very innovative antennas and microwave components [62, 65-66].

The geometry of the MTM-inspired printed monopole is showed in figure 3.4. It is composed of a central radiating element and two ground planes, which, together with a central RF line, form the supply line coplanar antenna.

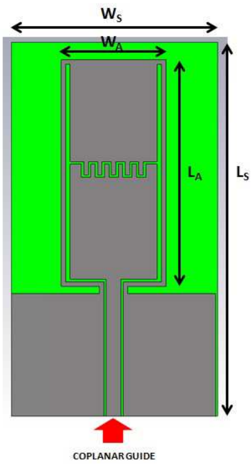

Substate ASTRA	
ε_R	3
tanD	0.003
H [μm]	500
W_S [mm]	30
L_S [mm]	50
Metamaterial Inspired Antenna	
W_A [mm]	15.21 (λ/11.5)
L_A [mm]	34.45 (λ/5.1)
t [μm]	9
B [GHz]	(1.71-2.53)
AREA [mm]	1650

Fig. 3.4 Geometry e dimensions of the printed MTM inspired antenna.

The starting parameters of the central radiating element, having length (L_A) and width (W_A), can be determined from the following expression [ref]

$$W_A = \frac{c}{2f_0}\sqrt{\frac{2}{\varepsilon_r + 1}} \tag{3.3}$$

$$L_A = \frac{c}{2f_0\sqrt{\varepsilon_{r,eff}}} \tag{3.4}$$

The antenna is fed by a 50**Ω** coplanar waveguide (CPW) transmission-line with the slot width of 0.12mm and the center conductor width 2.2 mm, which can be easily integrated with the other CPW-based microwave circuits.

The "planar MTM" is represented by the shunt inductance (obtained through a metallic strip connecting the monopole to the ground plane) and the series capacitance (implemented through an interdigited capacitor placed to the centre of the monopole). The monopole is printed on a flexible 0.5mm Astra Isola dielectric (ε_r=3, tanδ=0.0017).

The geometry of the overall "planar MTM antenna" (printed monopole, shunt inductances and interdigited capacitor) has been numerically optimized with CST full-wave simulator in order to match the monopole with the SMA. The reflection coefficient magnitude at the input port, reported in figure 3.5, shows a frequency band of operation (<-10dB) from 1700 to 2550 MHz, which does not completely fulfil the requirement.

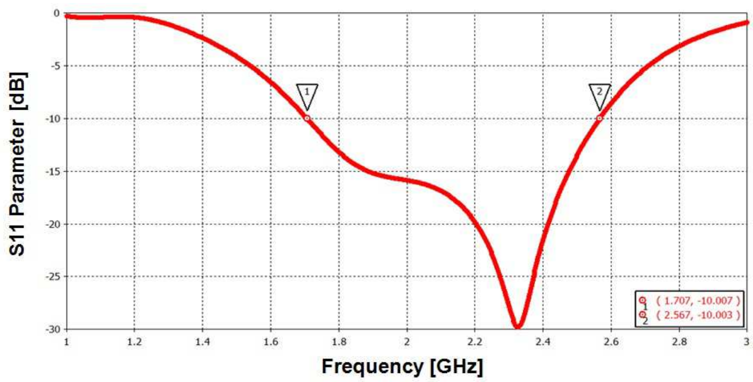

Fig. 3.5 .Magnitude of the reflection coefficient at the SMA port for the MTM inspired monopole antenna.

The gain pattern of the proposed antenna on the (a) horizontal and (b) vertical planes is shown in the figure 3.6. By varying the frequency, the antenna gain remains constant at 2dB. Note that the co-polar (co-) and cross-polar (X-) components are the vertical and the horizontal ones, respectively. These show that the radiation performance of the antenna in terms of polarization purity and pattern shape are rather stable with the frequency.

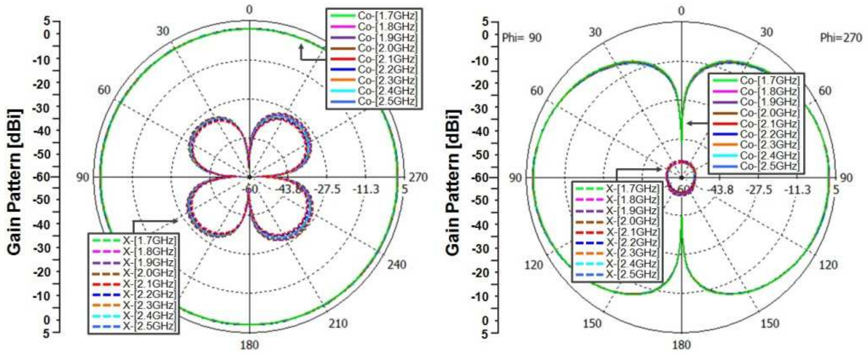

Fig. 3.6: Gain pattern of the printed monopole of figure 3.4 on the (a) horizontal and (b) vertical planes. Co-polar (co-) and cross-polar (X-) components are the vertical and the horizontal ones, respectively.

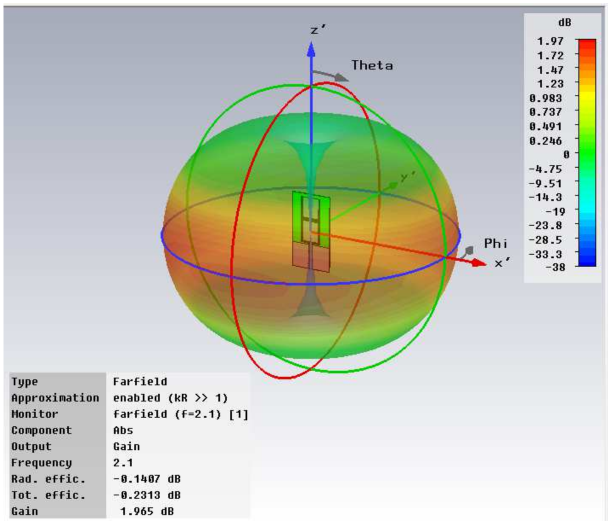

Fig. 3.7 Gain pattern of the printed monopole of figure 3.4 in 3D view @ 2.1GHz.

In order to demonstrate the efficiency of the flexible antenna when it is subjected to a deformation, simulations were carried out for varying parameter K that indicates the vertical deformation of the substrate on which the antenna is printed. Figure 3.8 shows the study cases analyzed.

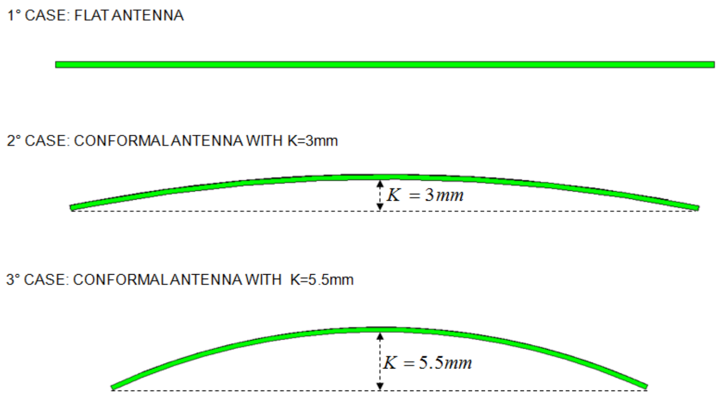

Fig. 3.8: Study cases analyzed for the flexible MTM inspired monopole antenna.

The vertical deformation values considered in the CST simulations were respectively K=0 (flat antenna), K=3mm and K=5.5mm. The reflection coefficient magnitude at the input port, varying the K parameter, is reported in figure 3.9, and it shows that the bandwidth remains almost constant.

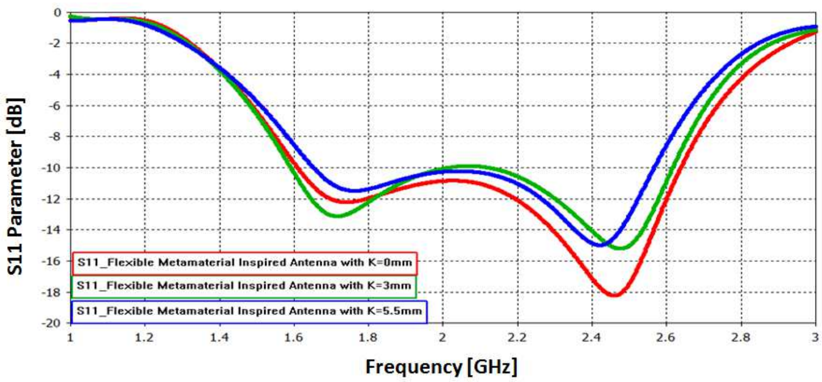

Fig. 3.9 Magnitude of the reflection coefficient S11 to vary the vertical deformation of the substrate.

Furthermore, the simulations confirm that this antenna continues to radiate in the Theta component and, as can be seen in the figure 3.10, it presents a gain which remains constant (for Theta=90 and Phi=90) for varying substrate deformation.

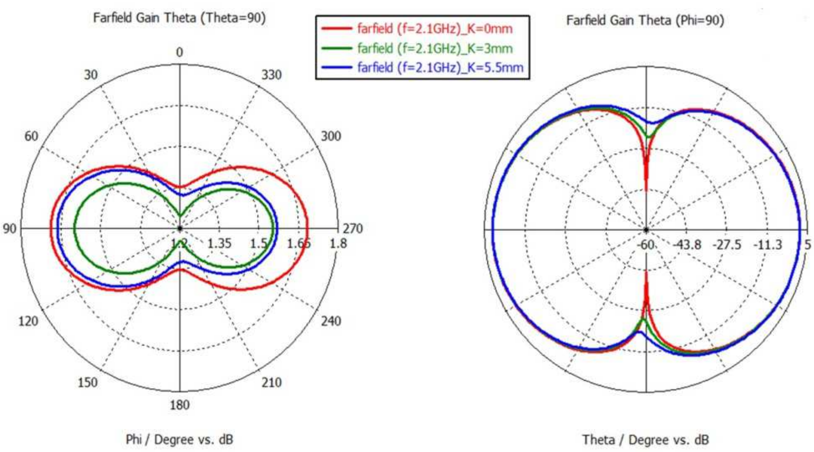

Fig. 3.10 Gain pattern of the flexible MTM inspired antenna on the (a) horizontal and (b) vertical planes to vary the vertical deformation of the substrate at 2.1GHz

This means that, in a range of deformation between 0mm and 5.5mm, the antenna continues to “maintain” the operating band it was designed for.

In order to demonstrate the efficiency of the proposed antenna, in terms of size reduction, it has been compared with two monopole antennas. The antennas are again assumed to be printed on ASTRA Isola substrate and fed by a 50 coaxial cable. In particular:

a) the first antenna, identified as Monopole Antenna 1, is the same antenna as above (with the same dimensions WS, LS) but without MTM components (unload monopole).

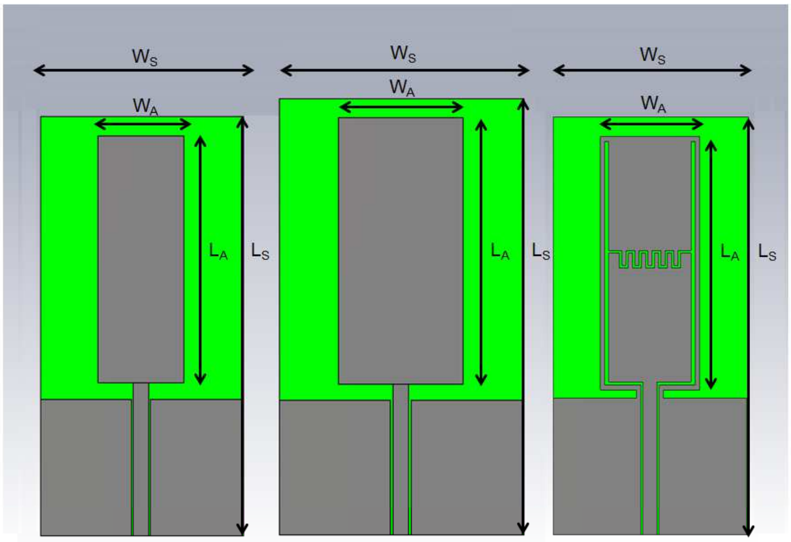

Substate ASTRA	
ε_R	3
tanD	0.003
H [µm]	500
W_S [mm]	30
L_S [mm]	50
Monopole Antenna 1	
W_A [mm]	12.65
L_A [mm]	32.3
t [µm]	9
B [GHz]	(1.818-2.585)
AREA [mm^2]	1500

Substate ASTRA	
ε_R	3
tanD	0.003
H [µm]	500
W_S [mm]	34
L_S [mm]	58.25
Monopole Antenna 2	
W_A [mm]	17.21
L_A [mm]	35.55
t [µm]	9
B [GHz]	(1.71-2.69)
AREA [mm^2]	1980.5

Substate ASTRA	
ε_R	3
tanD	0.003
H [µm]	500
W_S [mm]	30
L_S [mm]	50
MTM Inspired Antenna	
W_A [mm]	15.21
L_A [mm]	34.45
t [µm]	9
B [GHz]	(1.71-2.53)
AREA [mm^2]	1500

Fig. 3.11: Geometry and dimensions of the MTM inspired monopole antenna (green line), Monopole Antenna 1 (red line) and Monopole Antenna 2 (blu line).

The geometry of the Monopole Antenna 1 and its dimensions are shown in figure 3.11. It has been optimized in order to work at the 2.2GHz (center frequency of the MTM inspired antenna work band). The maximum frequency bandwidth of this antenna is comprised between 1.818GHz and 2.585GHz (red line in the figure 3.12). It is possible to note that the bands of the two antennas are not identical, although they have the same dimensions. This is due to the inclusion of the MTM components in the Monopole Antenna 1. The working band is shifted towards lower frequencies by 100MHz. Now, since the two antennas have the same size but the MTM inspired antenna radiates at lower frequencies, this proves that we have compacted the total size of the proposed antenna

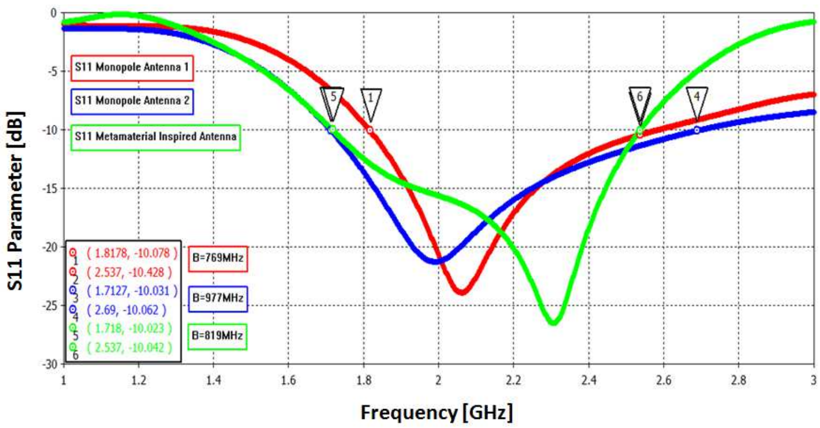

Fig. 3.12 Gain Magnitude of the reflection coefficient at the SMA port for the MTM inspired monopole antenna (green line), Monopole Antenna 1 (red line) and Monopole Antenna 2 (blu line).

b) the second antenna, identified as, Monopole Antenna 2, is an antenna similar to the Monopole Antenna 1, but it has been optimized in order to obtain an ultra wide-band, starting from 1.7GHz (blue line in the figure 3.12). The aim is to compare the area of two antennas having the same working band. The optimization process has led to a variation in the size of the antenna compared to the case of Monopole Antenna 1. The geometry of the Monopole Antenna 2 and its dimensions are shown in figure 3.11.

Comparing the working bandwidth and the total area of the two types of antennas, it can be affirmed that, in these conditions, the inclusion of MTM components on the same dipole, leads to a decrease of 17% of the total antenna size. Before concluding, we remark that other monopoles have been designed with the aim to check the effect of reducing the supporting board dimensions.

3.3.1.2 Metamaterial Inspired Antenna Prototype and Measurements

In this sub-section, the prototype of the proposed antenna and relative measurements are reported. In particular, in figure 3. 13, the designed, fabricated, and tested antenna is showed. The whole antenna dimensions are 30 mm x 55 mm x 0.5 mm and the design is based on the MTM concept of phase compensation, obtained in this case through a series capacitive loading (i.e. the interdigited capacitance along the body of the monopole) and a shunt inductance (i.e. the strips running around the monopole connecting the monopole to the ground plane).

Fig. 3.13 MTM inspired monopole antenna prototype manufactured on flexible substrate.

In this sub-section are reported the measured results obtained from the fabricated antenna prototype. The measurement was performed using Agilent E8362B PNA series network analyzer.

The CST-simulated and measured magnitudes of S11 are shown in figure 3.14 The antenna exhibits the characteristics of the ultra-wide band operation, i.e., a measured -10 dB bandwidth of 900MHz from 1.6GHz to 2.5GHz.

The antenna therefore covers all the required services: GSM1800, UMTS, and Wi-Fi. The measurements have been carried out in an anechoic chamber.

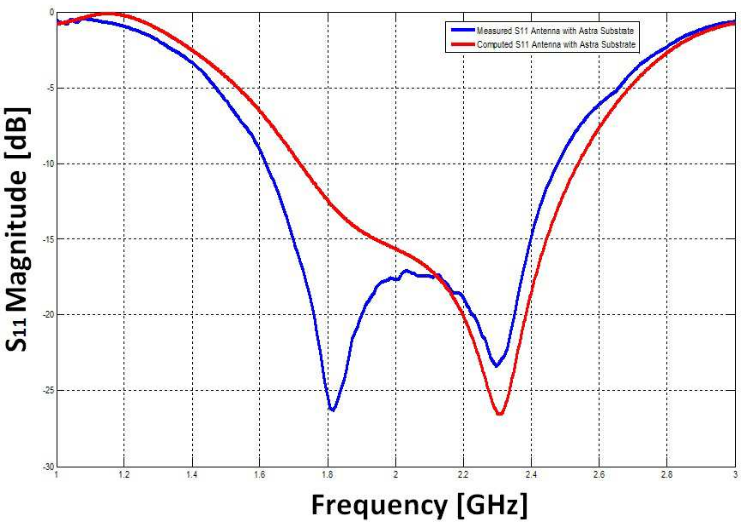

Fig. 3.14 Computed and measured S11 of a MTM inspired printed.

A small discrepancy in terms of frequency shift is observed between the simulated and measured return loss of the proposed antenna. These frequency shifts are attributed to the manufacturing tolerance errors, the surface roughness, soldering, and also to the connector's effect. This association of the antenna on the PCB resulted in small shifts of resonances without any noticeable degradation of their bandwidths.

After all, the measurements made show a good matching with the simulations in terms of both bandwidth and gain.

3.3.1.3 Flexible Wideband Metamaterial-Based Antenna Array

The designed antenna possesses all the necessary requirements to be used in the RF energy harvesting architecture. The only drawback regards the feeding of the antenna: it is not in microstrip technology but in coplanar technology. This could cause problems in the layout design of the rectifier circuit (which is connected after the antenna). The production of a layout in coplanar technology requires the occupation of a larger area since on the metal layer placed on the substrate, in addition to the RF signal, also the two ground planes that serve as reference to the RF signal must be present. In this way it is necessary to adapt the parameters again bringing the antenna ground plane under the substrate by means of two vias which connect the two metallization separated by the substrate. At the end of an optimization process, the new parameters of the antenna are shown in figure 3.15.

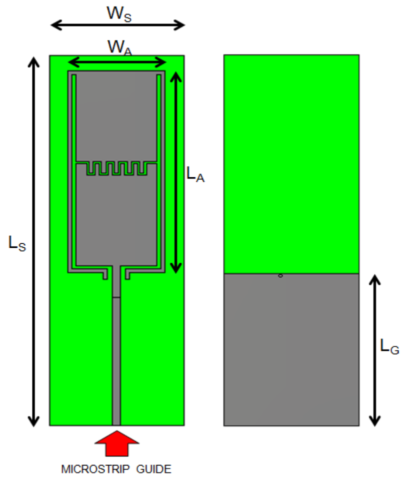

Substate ASTRA	
ε_R	3
tanD	0.003
H [µm]	500
W_S [mm]	21
L_S [mm]	61.25
L_G [mm]	25.05
Metamaterial Inspired Antenna in MT	
W_A [mm]	15.21
L_A [mm]	34.45
t [µm]	9
B [GHz]	(1.818-2.585)
AREA [mm2]	1286

Fig. 3.15 Geometry and dimensions of antenna in microstrip technology.

The performance of the S11 parameter that defines the working band is shown in figure 3.16. The antenna has a working band (1.7GHz-2.5GHz) perfectly in line with the demands of the project specifications.

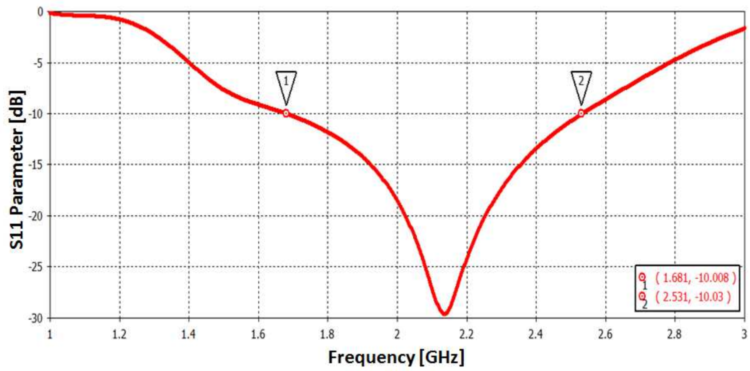

Fig.3.16 Performance of the S11 parameter antenna adapted in microstrip technology in CST.

Below is shown the trend of the radiation pattern of the monopole (in the two components of theta and phi) at the center frequency (@2.1GHz). As can be seen in figure 3.17, the antenna maintains a vertical polarization and a gain of 2 dB.

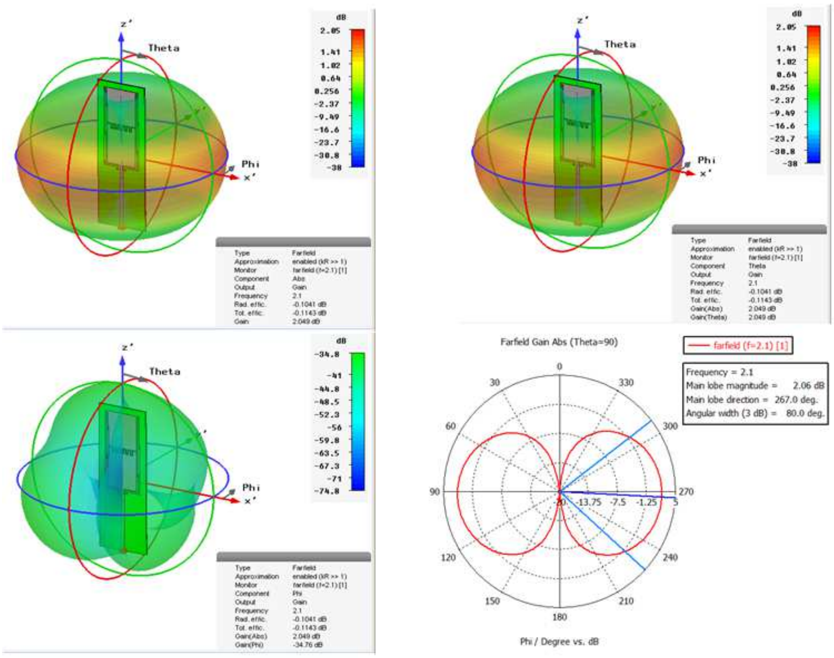

Fig.3.17 Gain and electromagnetic field performance (in the components theta and phi) of antenna in technology microstrip calculated at frequency of 2.1GHz.

Once adapted the geometric parameters of the antenna and checked the performances by a full-wave 3D simulator like CST, the next step has been to simulate the same antenna using another simulator like ADS which is not 3D but 2.5D. In fact, ADS is a simulator that allows the planar electromagnetic analysis of planar structures such as an antenna. The antenna in ADS is shown in figure 3.18. The upper metal layer that constitutes the antenna is brown in color, while the lower one, which represents the ground plane is of a yellow color. As can be seen, the two layers are connected through two via holes (blue color) which drill the substrate (the Z axis in the figure is not to scale).

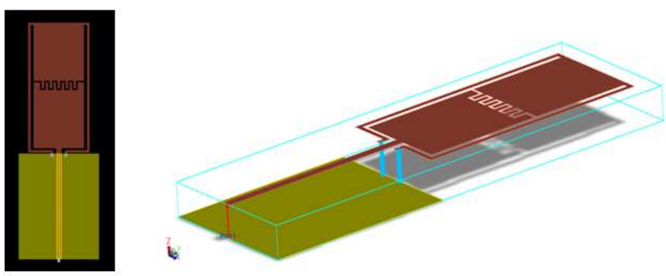

Fig.3.18 3D view of antenna in microstrip technology in ADS software.

The working band is determined by the S11 parameter performance which is showed in figure 3.19. In figure 3.20 it is possible to note two main lobes due to the absence of the ground plane below the antenna.

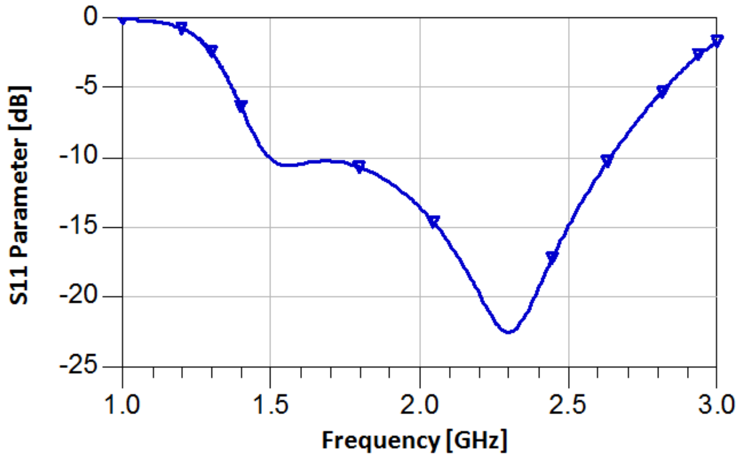

Fig.3.19: S11 parameter performance antenna adapted in microstrip technology simulated in ADS software.

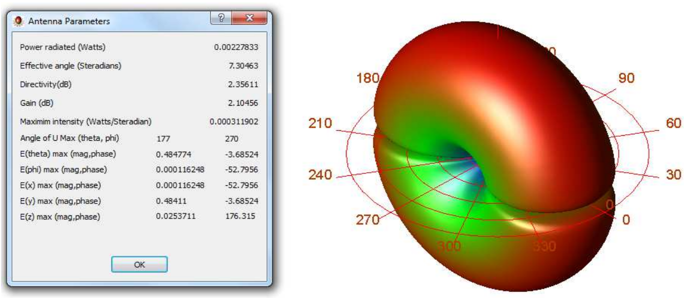

Fig.3.20 Parameters and radiation pattern of the antenna adapted in microstrip technology simulated in ADS software.

Once designed and sized the radiating element, the next step was to design an antenna array in such a way of increasing the gain and the reception of the electromagnetic power. The antenna array consisting of four antennas equally spaced among them to λ / 2 (with λ corresponding to the minimum operating frequency, @1.7GHz) is shown in figure 3.21.

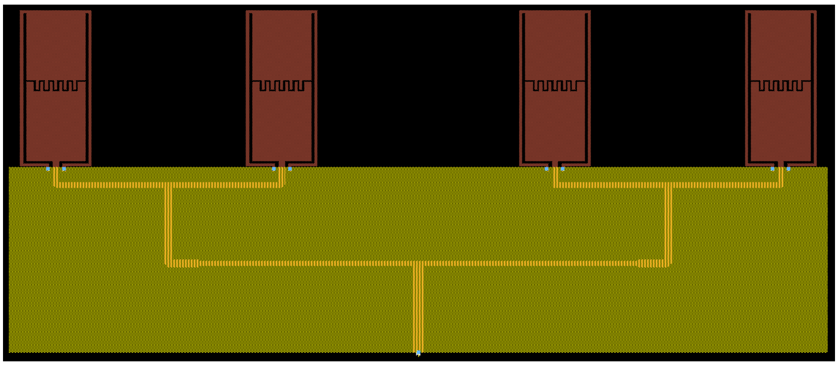

Fig.3.21 Antenna array 1x4 in microstrip technology (2D view).

The design of the antenna array provided the sizing (in terms of width and length) of the feed line. In fact, in order to obtain 50Ω in input of array antenna, a beam-forming network has been designed. As shown in Fig.3.21, the width of the microstrip feed lines are not constant but was determined after an optimization process. At the end of this process, the S11 parameter which determines the working band of the array, respects the design specifications.

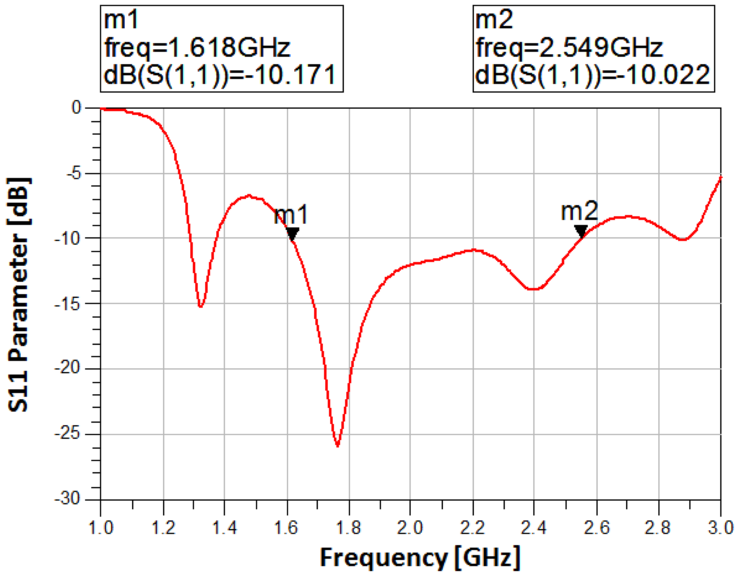

Fig.3.22 S11 parameter performance of the antenna array in microstrip technology.

Also in this case the radiation pattern of the antenna array presents two main lobes (see Figure 3.23) while the gain is increased from 1.9dB to 7.8dB

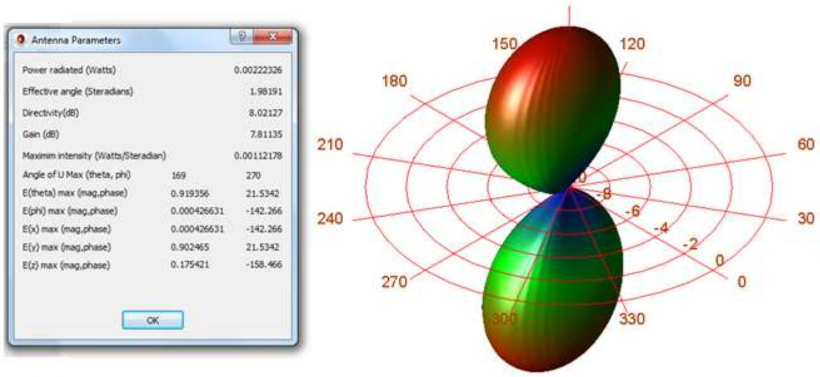

Fig.3.23 Parameters and pattern radiation of antenna array.

3.3.2 Rectifier Circuit

The approach to the RF energy harvesting circuit design proposed here is based on a voltage rectifier circuit. In this subsection we explain how the components were selected. In particular the dependence of the rectification efficiency on these components was evaluated.

3.3.2.1 Voltage Multiplier Rectifier

The Voltage Multiplier Rectifier, as shown in Fig.3.23., has been widely used in micro-power harvesting circuit [67-71]. The basic structure of the conventionally used charge-pump rectifier is similar to Dickson's DC-DC charge pump architecture [72], which was proposed in 1976 and originally used as DC-DC up-converter.

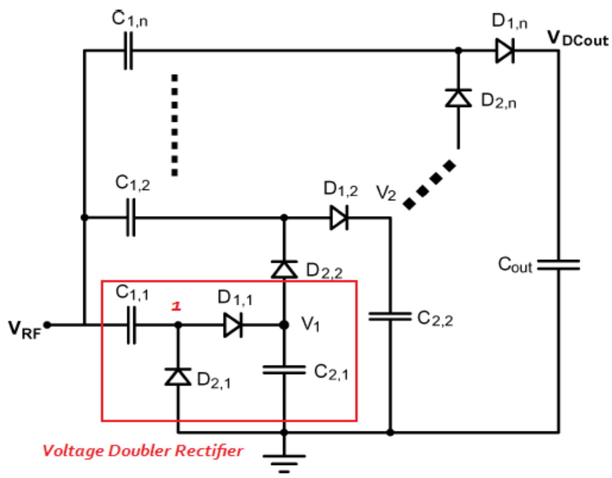

Fig. 3.24 N-stage voltage multiplier as a cascade of n - voltage doubler rectifiers.

The voltage doubler rectifier structure is considered for the design of the RF-Energy Harvesting system because it rectifies the RF signal input. The voltage doubler rectifier in figure 3.24 consists of a peak rectifier formed by C2 and D1 and a voltage clamp formed by C1 and D2.

The voltage doubler rectifier output is:

$$V_{OUT=}\left(2V_{RFamp} - V_{th1} - V_{th2}\right) \tag{3.5}$$

where Vth is the threshold voltage of the diode and V_{RFamp} is the RF input voltage. The individual stages of voltage doubler rectifier circuit can be arranged in cascade as in figure 2 (N-stage voltage multiplier) to increase the output voltage of the rectifier [73].

$$V_{OUT=}\left(2NV_{RFamp} - 2NV_{th} - \frac{(N-1)I_{LOAD}}{f_0 * C}\right) \tag{3.6}$$

where I_{LOAD} is the load current, *C* are the blocking capacitor and f_0 is the working frequency.

When the rectifier stages are cascaded, each rectifier stage acts as a passive voltage level shifter in addition to the voltage shift in voltage clamp and peak rectification. The number of rectifier stages used in the design is an important parameter. Indeed, choosing too few rectifier stages means to have insufficient output voltage and, on the other side, choosing too many rectifier stages damps out the effect of the high- resonator.

In particular, let us suppose that a sinusoidal voltage, V_{RF}, with a frequency f_0 and amplitude V_{RFamp}, is applied at the input of the voltage multiplier. In order to have a small ripple in the output voltage, capacitances have to be dimensioned so that the time constant is much smaller than the period of the input signal, that is, $1/(2\pi CRL) << f_0$, where *C* are the blocking capacitors and R_L is the equivalent load resistance. In this way, the voltage applied to all *C* capacitors and the output voltage can be considered a DC voltage. In such condition the input-output characteristic is implicitly given by,

$$\left(1+\frac{V_{OUT}}{R_L I_{D,SAT}}\right) exp\left(\frac{V_{OUT}}{2NV_T}\right) = B_0\left(\frac{V_{\mathrm{RFamp}}}{V_T}\right) \tag{3.7}$$

where V_T, is the thermal voltage and B_0 is the modified Bessel function of zero order. Solving (3.7) by numerical iteration, for a fixed output voltage and power consumption, it is possible to note that the higher is the number of stages, the smaller is the amplitude of the input voltage required to obtain a given DC output voltage and power consumption. This is true as far as the number of stages N becomes too large.

3.3.2.2 Choice of Diodes

One of the crucial requirements for the energy harvesting circuit is to be able to operate with weak input RF power. For a typical 50 Ω antenna, the −20 dBm received RF power signal means an amplitude of 32 mV. As the peak voltage of the AC signal obtained at the antenna is generally much smaller than the diode threshold [74], diodes with the lowest possible turn on voltage are preferable. In these applications, the Schottky diode is the best. It uses a metal-semiconductor junction instead of a semiconductor-semiconductor junction. This allows the junction to operate much faster, and gives a forward voltage drop of as low as 0.15V.

In order to achieve a good performance, suitable Schottky diodes should be chosen from those available on the market. The AVAGO HSMS family diodes are ideal for these applications. In particular,in this work, the HSMS2852 [75] diode has been selected.

The equivalent circuit of a Schottky diode is shown in figure 3.25. [76], along with its package parasitic element.

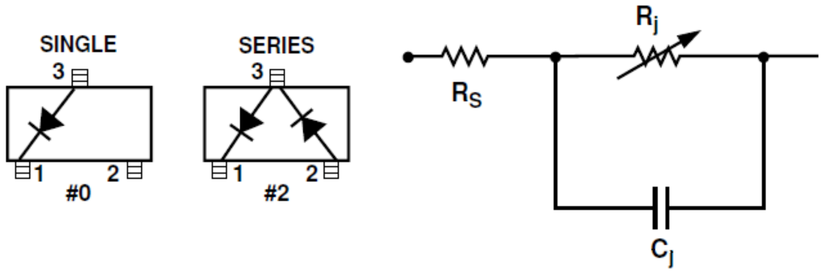

Fig. 3.25 Agilent HSMS2850 equivalent circuit of a diode Schottky.

In order to reduce the loss in the diode, it should have large saturation current I_S, low junction capacitance C_J which result in low forward voltage V_d; small series resistance R_S, small junction resistance R_V and also finally smaller parasitic effects to the substrate.

Parameter	***Units***	***HSMS-285x***
B_V	V	3.8
C_{IO}	pF	0.18
E_G	eV	0.69
I_{BV}	A	3E-4
I_S	A	3E-6
N		1.06
R_S	Ω	25
$P_B(V_J)$	V	0.35
$P_T(XTI)$		2
M		0.5

Tab. 3.5 Spice parameters of a HSMS2852 diode Schottky.

3.3.2.3 Number of Stages

The number of rectifier stages N has a major influence on the output voltage of the energy harvesting circuit. In N-stage voltage multiplier circuit, each stage is a modified voltage multiplier, arranged in series. The output voltage is directly proportional to the number of stages used and then N has a major influence on the output voltage of the circuit. Moreover, the constraints force a limit on the number of permissible stages. In fact, the voltage gain decreases as the number of stages increases due to parasitic effect of the capacitors, and finally it becomes negligible.

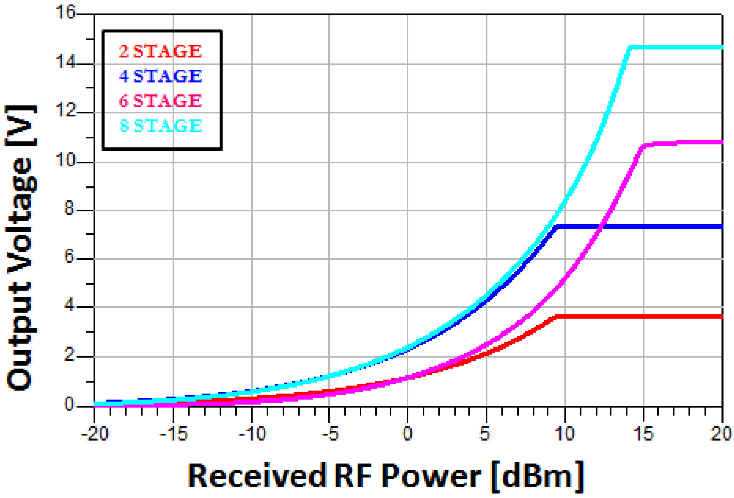

Fig. 3.26 Effect of number of stages on the output voltage of energy harvesting circuit.

Figure 3.26-show the impact of number of stages on output voltage of an energy harvesting circuit.

We have used Agilent ADS with parameters sweep of −20dBm to 20dBm for the input RF power and circuits with various numbers of stages, from 2 to 8 stages. The simulated circuit stage is a modified voltage multiplier made of HSMS-2852, arranged in series and a 10nF capacitors. The voltage plot shows that the highest voltage can be achieved by increasing the number of circuit stages, but a corresponding increase in power loss is also introduced into the low power region.

3.3.2.4 Effect of the Load Impedance

In the RF energy harvesting applications, the effect of the load impedance is very important because it impacts on the circuit performance (figure 3.27). We simulate the effect of load impedance on the efficiency of the energy harvesting circuit using Agilent ADS with parameters sweeped from −30dBm to 30dBm and 500Ω to 1MΩ for input RF power and load value, respectively.

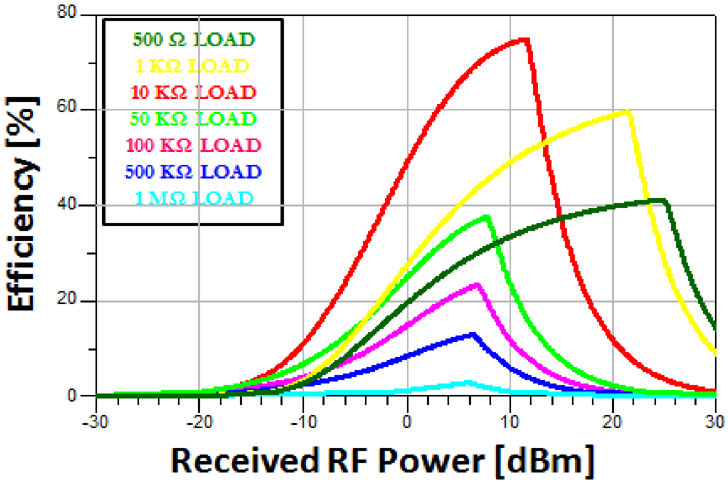

Fig. 3.27 Effect of load impedance on the rectification efficiency of energy harvesting circuit.

We observe that the circuit yields the optimal efficiency at a particular load value, that is, the circuit's efficiency decreases dramatically if the load value is too low or too high. The energy harvesting in simulation is a 6-stage circuit, each stage is a modified voltage multiplier of HSMS-2852, arranged in series. This behavior is caused by the non linear characteristics of the diode, and, specifically, by his resistance, depending from the bias current. In fact, with a given a received RF power, there is only an optimal load that maximizes the power transfer.

3.3.2.5 Effect of the RF Input Power

Due to the presence of the diodes, the RF energy harvesting exhibits non-linearity characteristics. This implies that the impedance of the energy harvesting circuit varies with the power received from the antenna. In this way, for the particular input power, the maximum power transfer to load can be obtained when the circuit is matched with the antenna by means of a impedance matching circuit.

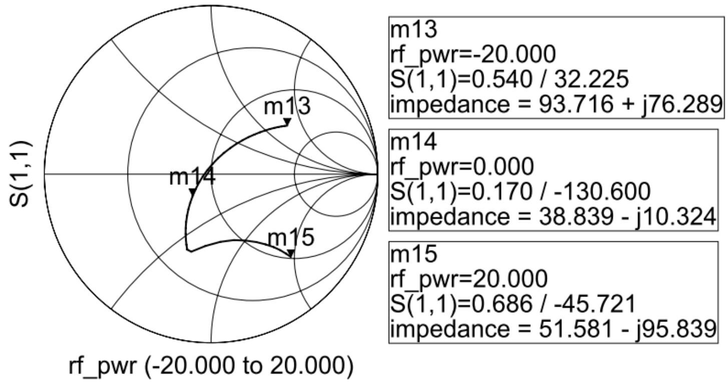

Fig. 3.28 Effect of RF input power on the impedance of the energy harvesting circuit.

Figure 3.28 depicts the effect of RF input power, ranging from −20dBm to 20dBm, on the impedance of the energy harvesting circuit.

3.3.3 Power Matching Circuit

A matching impedance circuit between the antenna and the rectifier circuit is necessary to increase the input voltage of the rectifier circuit.

The equivalent input impedance of the voltage multiplier might be represented, as a zero-order approximation, by the parallel of a resistance and a capacitance. In the high frequency analysis of the voltage multiplier, all the capacitances of the voltage multiplier can be considered as short-circuited and so all diodes can be considered in parallel or anti-parallel with the input. As a consequence, at the input of the voltage multiplier, the capacitances of all diodes are in parallel [73]. The equivalent input resistance, Rin_eq of the voltage multiplier is the resistance calculated from power consumption as:

$$R_{in\_eq} = \frac{V_{RFamp}}{2P_{IN}} \tag{3.8}$$

In order to compensate the equivalent input capacitance of the voltage multiplier a proper inductance L', in parallel with the input of the voltage multiplier can be used. So, the input impedance of the voltage multiplier can be modeled as a resistive load that allows to use a simple "impedance transformer" (classic $\lambda/4$ transformer) able to increase the voltage value at the rectifier circuit input.

Since the input capacitance due to the diodes is variable with the voltage across diodes, the inductance L' is dimensioned in order to resonate with its average value at the operating frequency f_0. Of course, this is reasonable when the variations of the input impedance around the mean value are small with respect to the equivalent input resistance [73]. This leads to the condition,

$$\Delta C \ll \frac{Q}{2\pi f_0 R_{in\_eq}} \tag{3.9}$$

where ΔC is the maximum variation of the input capacitance of the voltage multiplier with respect to its mean value.

In order to realize the $\lambda/4$ transformer we use an LC matching network circuit (L series and C shunt).

The Q-factor of the LC matching network is limited by the resistance transformation ratio [77] and its expression is given by

$$Q = \sqrt{\left(\frac{R_{in\_eq}}{R_{ANT}}\right) - 1} \tag{3.10}$$

where R_{ANT} is the antenna resistance.

Using an LC power matching network, the values of L and C are chosen as [77]:

$$L = \frac{QR_{ANT}}{\omega_0} \quad \text{and} \quad C = \frac{Q}{R_{in\_eq}\omega_0} \tag{3.11}$$

and the voltage value at the rectifier circuit input is $V_{RFamp} = QV_{RFsource}$.

Note that the matching circuit is a crucial device for an harvesting system. Indeed, the conversion efficiency of the system η defined as

$$\eta[P_{RF}(f_i, t), \rho, Z_{DC}] = \frac{P_{DC}(f_i)}{P_{RF}(f_i, t)} \tag{3.12}$$

where P_{RF} $(f_i;t)$ is the statistically varying incident RF power and $P_{DC}(f_i)$ is the output load power, is closely related to the impedance matching $\varrho(P_{RF}; f_i)$ between the antenna and the rectifier circuit that is a nonlinear function of both power and frequency.

3.4 Ultra Low Power Comparator

The last component to be examined in the architecture in figure 3.3, is the comparator. We chose an integrated circuit provided by Linear Technologies, LTC1540 [78].

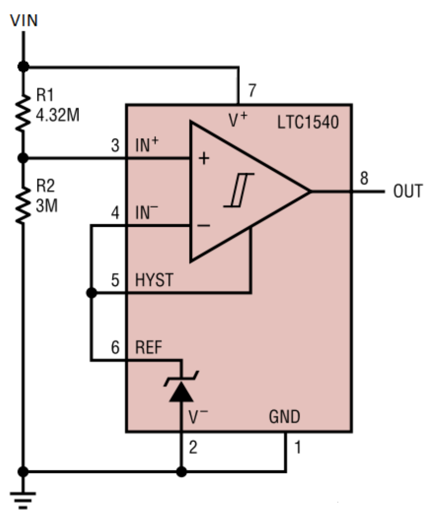

Fig. 3.29 Nanopower threshold detector.

The LTC1540 is an ultralow power, single comparator with built-in reference. The comparator operates from a single 2V to 11V supply and 2V represent a good power supply for the energy harvesting applications. The comparator hysteresis is easily programmed by two resistors and the HYST pin. The LTC1540 is ideal for use as a nanopower level detector as shown in figure 29. R1 and R2 form a voltage divider from V_{IN} to the non-inverting comparator input. R3 and R4 set the hysteresis voltage, and R5 and C1 bypass the reference output. The following design procedure can be used to select the component values:

1. Choose the V_{IN} voltage trip level, in this example 2.1V.
2. Calculate the required resistive divider ratio.

$$Ratio = \frac{V_{REF}}{V_{IN}} = \frac{1.182V}{2.1V} = 0.56 \qquad (3.13)$$

3. Choose the required hysteresis voltage band at the input V_{HBIN}, in this example 60mV. Calculate the hysteresis voltage band referred to the comparator input V_{HB}.

$$V_{HB} = (V_{HBIN}) \cdot (Ratio) = (60mV) \cdot (0.56) = 33.6m \qquad (3.14)$$

4. Choose the values for R3 and R4 to set the hysteresis.

$$\text{R4} = 2.4\text{M}\Omega \qquad (3.15)$$

$$V_{HB} = 33mV \ \Rightarrow R3 = 33k\Omega \qquad (3.16)$$

5. Choose the values for R1 and R2 to set the trip point.

$$1 = \frac{V_{REF}}{I_{BIAS}} = \frac{1.182V}{1\mu A} = 1.182M\Omega \qquad (3.17)$$

$$R2 = R1 \cdot \left[\frac{V_{IN}}{V_{REF} + \frac{V_{HB}}{2}} - 1 \right]$$

$$= 1.18M\Omega \cdot \left[\frac{2.1V}{1.182V + \frac{33mV}{2}} - 1 \right] = 887\text{K}\Omega \qquad (3.18)$$

As can be seen from figure 3.4, this component is connected to the rectenna circuit. This means that the load seen by the rectenna is the input impedance of comparator. In order to optimize the rectenna circuit (in particular the power matching circuit), it is necessary to calculate the comparator input impedance. The procedure by which it was possible to calculate is shown in the next chapter (Chapter 5, par. 5.3.2) because the comparator must be connected to the input power management circuit which, in fact, will be examined later. The results show that the input impedance mean value is 24kΩ. Comparing with figure 3.27, it is possible to note that this value is a very good load in order to obtain high rectification efficiency of energy harvesting circuit. For this region, the 24 kΩ value will be used as resistive load for the rectenna optimization.

3.5 Improvement of the Widedand RR Energy Harvesting Architecture

In the preceding paragraphs, the components of the wideband RF energy harvesting architecture were analyzed. In fact, the guidelines regarding the sizing of the impedance matching network and the rectifier circuit were defined. In particular, for the latter, it was obtained the rectification efficiency at different number of stages, loads, RF input powers and also for different diodes. Having this information available and considering that the system will be working at the frequencies of the GSM1800, UMTS and Wi-Fi, it was initially thought to use three double-stage rectifier circuits (each operating at a different frequency). For low power system, the Schottky diode HSMS 2852 from Avago technologies is chosen for its low voltage threshold. In this case, the equivalent load considered is the input impedance of the following stage (ultra low power comparator).

The connection of the three rectifier circuits is shown in Figure 3.30

In order to achieve high efficiency rectification, the rectifiers need to be matched to the antenna at all three frequency bands. In fact, the three matching networks with poor bandwidth characteristics, have been designed (following the lineguide paragraph 3.3.3.) to perform an impedance matching between the antenna and the rectification circuit operating at different frequencies.

The RF energy harvesting circuit is simulated using Agilent Advanced Design System (ADS) software. In this work we use the harmonic balanced analysis (a frequency domain method) since our objective is to compute the steady state solution of a non-linear circuit. The alternate method, the so called transient analysis that is undertaken in the time domain, is not used due to the reason that it must collect sufficient samples for the highest frequency component. This involves significant memory and processing requirements. The circuit has an RF power generator multi-tone which represents the three RF sources with real impedance of 50 Ω.

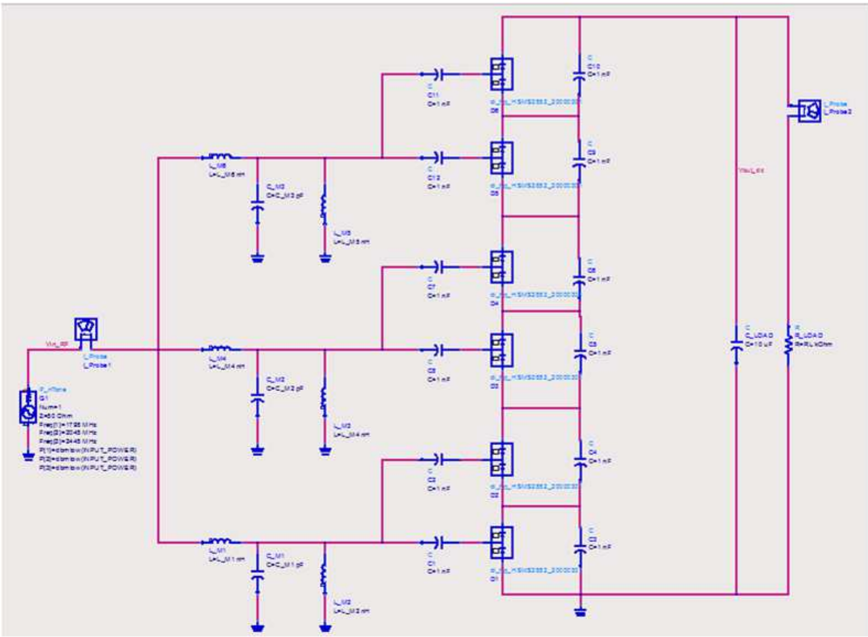

Fig.3.30 Old RF energy harvesting architecture implemented in ADS software.

The rectification efficiency of this architecture, varying the RF power input and working frequency, is shown in figure 3.33 (green line). As can be seen, in all three cases, considering an RF input power of 0dBm, the rectification efficiency is always higher than 40%. Furthermore, in figure 3.34 were also considered the cases where there are also other RF signals in input to the circuit. In particular, considering an equivalent input power equal to 0dBm, the rectification efficiency values are higher than 50%.

The main disadvantage of this architecture is the matching network. In fact, it is difficult to achieve a good matching because the input impedance of a rectifier circuit is dependent on the other two circuits. Moreover, if we consider that the latter also depends on the RF input power and the load, it is evident that the matching networks are not "robust" to the variations of the working conditions of the entire architecture.

To solve this problem, it was decided to use only one matching network and only one rectification circuit in three stages. The electrical circuit of the new architecture is shown in figure 3.31.

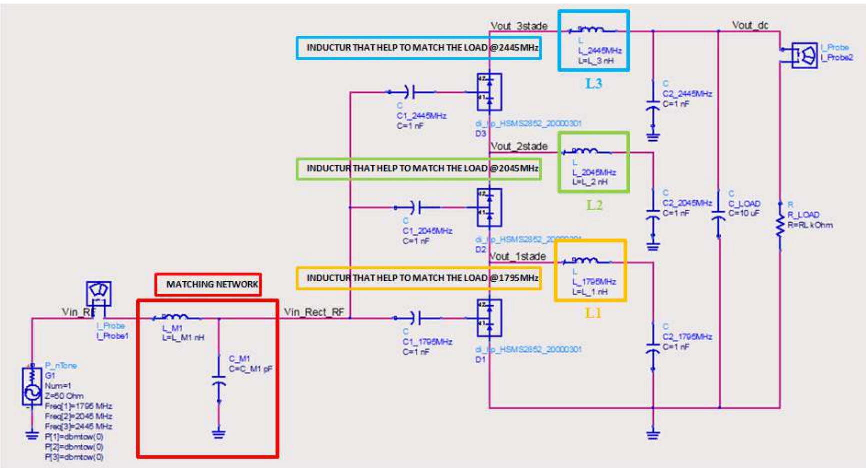

Fig.3.31 New RF energy harvesting architecture implemented in ADS software.

Designing a triple-band matching network is not trivial. A technique of designing a multiple band matching network for the rectifier is presented [79]. It simplifies the circuit and allows for tuning each matching frequency independently. Figure 3.31 shows the schematic diagram of the rectifier. A three-stage rectifier is chosen to have not only high sensitivity but also ease of the triple band matching. A LC voltage boosting network is used to match the antenna impedance with that the rectifier circuit. Moreover, the three lumped inductors L1, L2, and L3 improve the matching to 50 Ohm at our three desired frequency bands. L1 is added to stage 1 in series with the load capacitor as well as L2 and Le respectively to 2 and 3 stage.

When L3 is shorted, the rectifier has only 2 matching frequencies at 1800MHz and 2100MHz bands. When L2 is shorted, the matching at 2100 MHz is off and matching only occurs at 1800MHz and 2.4GHz. Similarly, the matching at 1800MHz is off if L2 is shorted. Therefore, we can say that L1 provides the matching for 1800MHz, L2 controls the matching for 2100MHz and L3 helps to match at 2.4GHz.

The choice of the values of L1, L2 and L3 is also a function of the load used. At this point it is necessary to highlight two aspects:

- The circuit of figure 3.31 should be connected to a power management circuit which supplies the WSN node;

- Considering the little power recoverable, it is indispensable that it is transferred to the power management circuit only when the output of the circuit of figure 3.31 reaches a steady value sufficient to supply that circuit. For this reason, it is necessary to include an ultra low comparator which has the task to activate the power management circuit only when the output of the RF Energy harvester reaches a minimum voltage of 2.1V.

This architecture, compared to the previous one, is more robust in terms of impedance matching and is composed of fewer components. This means to have available a stroger control of the parameters of the project and a lower cost of the prototype.

3.6 Simulation Results

The values of L and C components used in the matching network, together with inductors L1, L2 and L3, were produced by an optimization process in which were defined six targets (GOALS) to satisfy (see figure 3.32). In particular, these components optimize the maximum power transfer between antenna and load at three different working frequencies.

Fig.3.32 Optimization process in ADS through which was carried out the impedance matching between the rectifying circuit and the antenna.

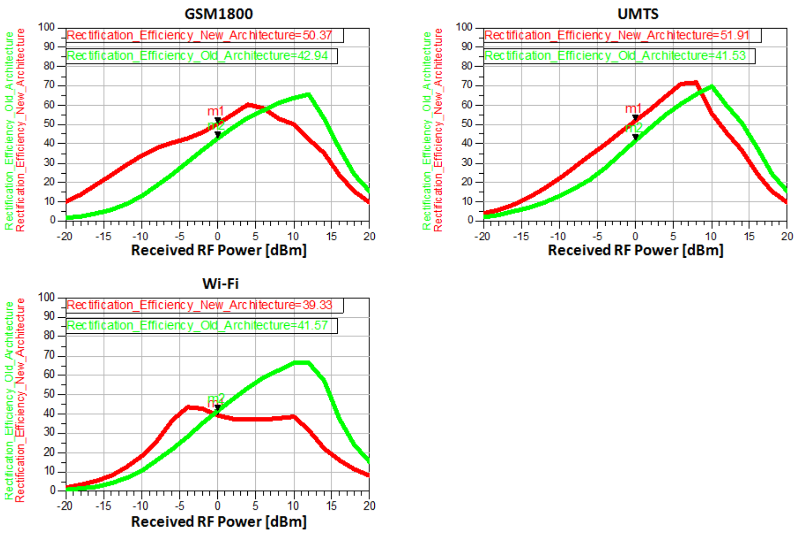

Fig.3.33 Comparison in terms of rectification efficiency of the two architectures to three different working frequencies.

After the optimization is achieved for both architectures, it was possible to compare them in terms of efficiency of rectification for different input RF signals. This comparison is shown in figure 3.33 and 3.33.

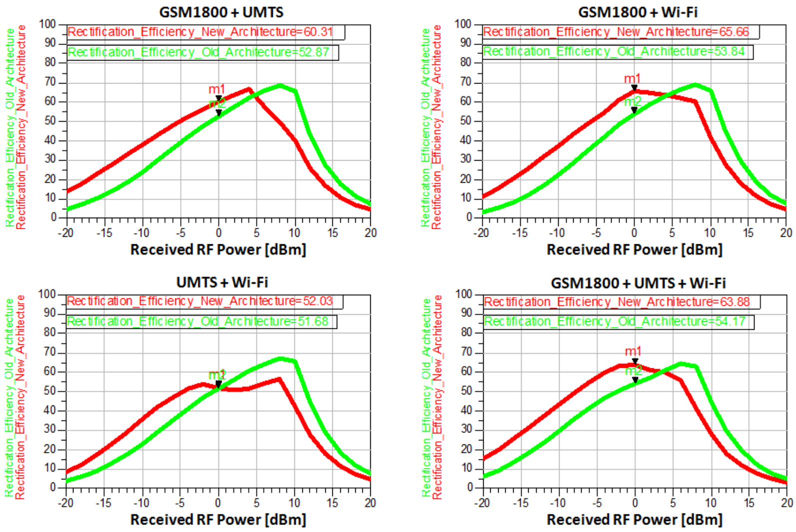

Fig.3.34 Comparison in terms of "rectification-sum" efficiency of the two architectures as a function of the sum of three different RF signals.

As can be seen, the efficiency values of the new architecture (red line), for a power range from -20dBm to 0 dBm, are always higher than those of the old architecture (green line). For input powers higher than 0dBm, the situation is the opposite.

Defined all circuit components values, it was decided to test the robustness of the circuit through a Monte Carlo simulation.

In particular, it was assumed a Gaussian distribution with a variance of 5% for all values of the L-C components.

In figure 3.35 are shown the trends of the rectification efficiency (red points) and the output voltage (blue points) to different values of the matching network (Lm and Cm) and the inductance L useful to further improve the adaptation of impedance fixed frequency and input power.

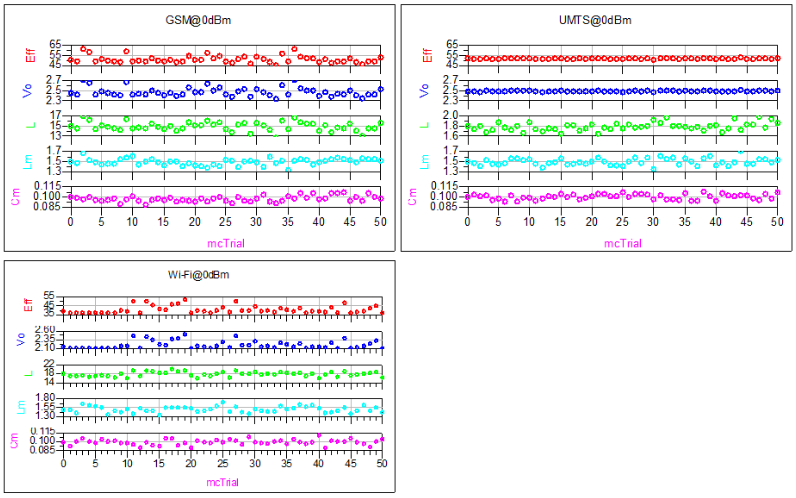

Fig.3.35 Performance of the rectification efficiency and the output voltage for varying matching network values at the three different working frequencies with 0dBm input power.

Using Monte Carlo simulations, it was analyzed the performance of the circuit when the RF sources are considered. In particular, the output voltage and rectification efficiency, varying the matching network component values and working frequency, are shown in the figure 3.36

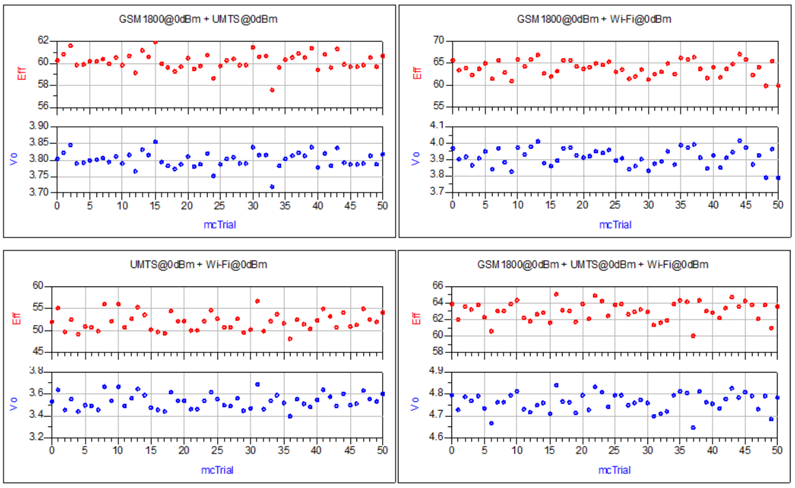

Fig.3.36 Performance of the rectification efficiency and the output voltage varying the matching network component values with multiple RF sources, assuming a 0dBm total input power.

The next step was to design the rectifier circuit layout in microstrip technology and to verify the performance considering the non-ideal characteristics of the substrate (Astra h = 500um, eps = 3, TnD = 0.0017).
For this reason, it was necessary to perform a Co-Simulation analysis using a planar simulator like ADS, which takes into account the circuital aspects and the mutual coupling phenomena.
In the figure 3.37, the final layout of the circuit of figure 3.31 is shown. The stack-up circuit is composed of an upper metal layer (brown layer), a substrate, a second metal layer placed under the substrate (yellow layer) that represents the ground plane and via holes that connect the two metal layers.

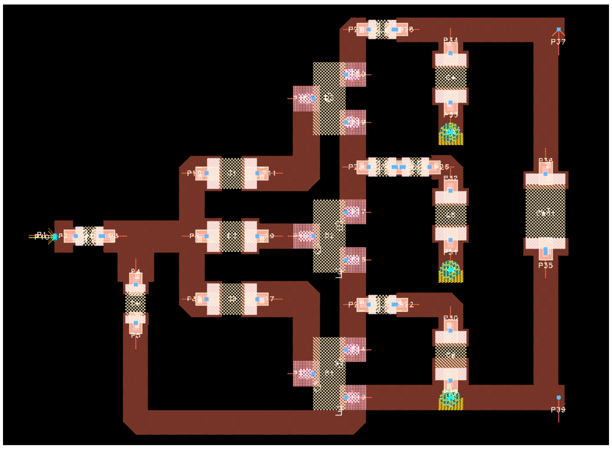

Fig.3.37 Rectifier circuit layout in microstrip technology.

As can be seen, there are all the components that constitute the rectifier circuit (diodes, capacitors, and inductors). These components are connected to the various metal layers through the port circuit.
In this way it is possible to simulate, using a co-simulation, the behavior of the circuit, considering every mutual couplings phenomena between the various metal tracks.

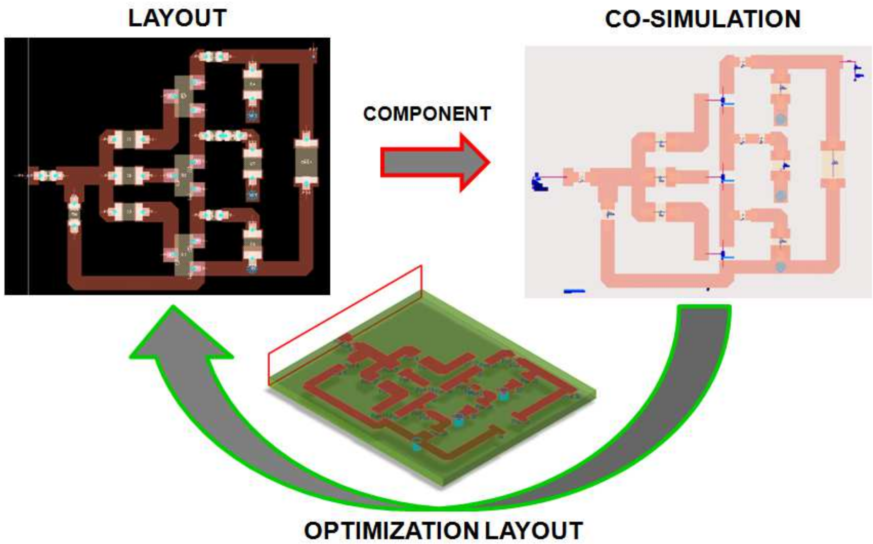

Fig.3.38 Co-Simulation process in ADS.

As expected, the introduction of the substrate into the design caused a worsening of the rectification efficiencies at different working frequencies.

To solve this problem, it was necessary to perform a new optimization process only for the components value and not on the layout geometry. Following this procedure, the various efficiencies of rectification and the relative output voltages (considering 24 kΩ for the load) at the three different working frequencies, are shown in figures 3.39 and 3.40.

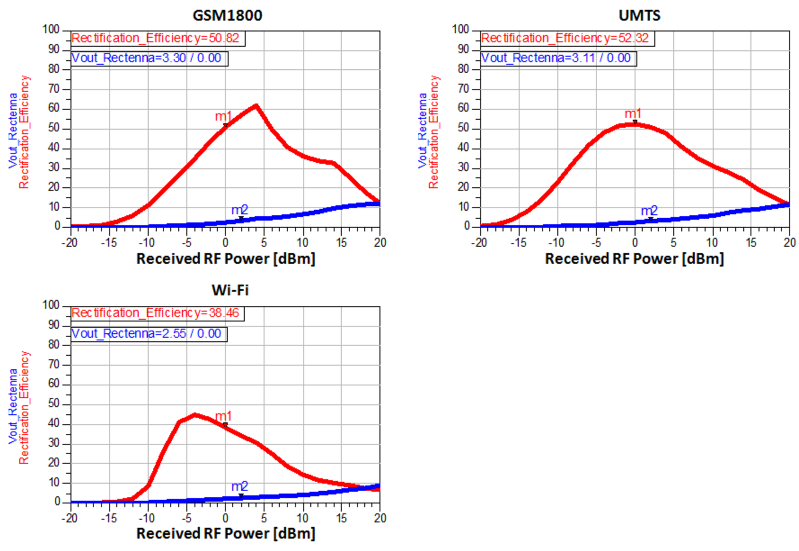

Fig.3.39 Rectification efficiency at three different frequencies derived from the co-simulation-optimization process.

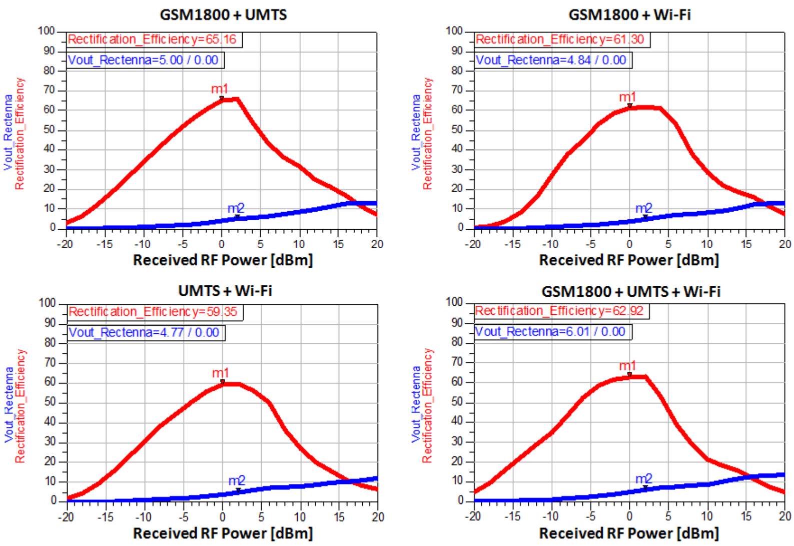

Fig.3.40 "Rectification-sum" efficiency according to the sum of three different RF signals derived from the co-simulation-optimization process.

Once fixed the values of the circuit components, it was decided to test again the robustness of the circuit by changing the component tolerances through a Monte Carlo simulation.

In figure 3.40 are shown the trend of the rectification efficiency (red points) and the output voltage (blue points) to different values of the matching network (Lm and Cm) and the inductance L which is useful to improve the adaptation impedance fixed the frequency and the input power. For example, in figure 3.41a is shown the trend of these parameters in case of a GSM signal with a power of 0dBm.

It can be noted, changing the parameters of the matching network and the L1 inductor (see figure 3.30), the rectification efficiency of the circuit, changes between 35% and 65%.

Afterwards, using a Monte Carlo simulation, it was possible to analyze the performance of the circuit when multiple RF sources are considered.

In particular figure 3.42 shows this trend considering the variation of the matching network components and the L inductor considering three different working frequencies and assuming a total input power equal to 0dBm.

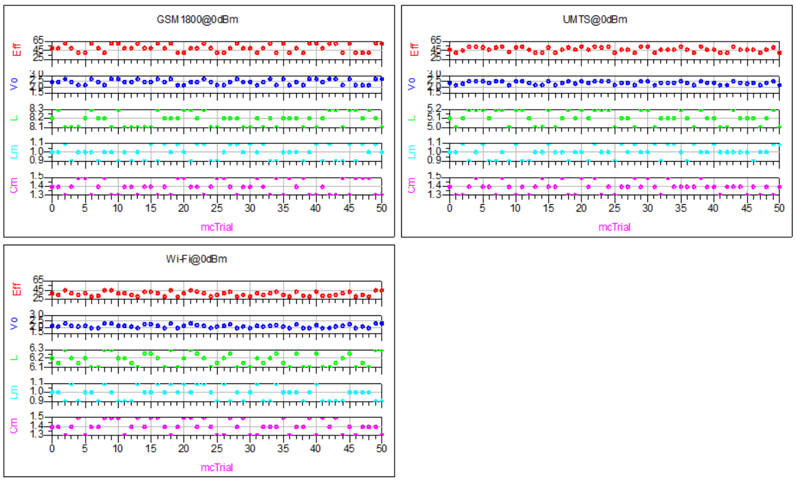

Fig.3.41 Performance of the rectification efficiency and the output voltage varying the matching network component values in the three different working frequencies assuming a total input power equal to 0dBm derived from the co-simulation-optimization process.

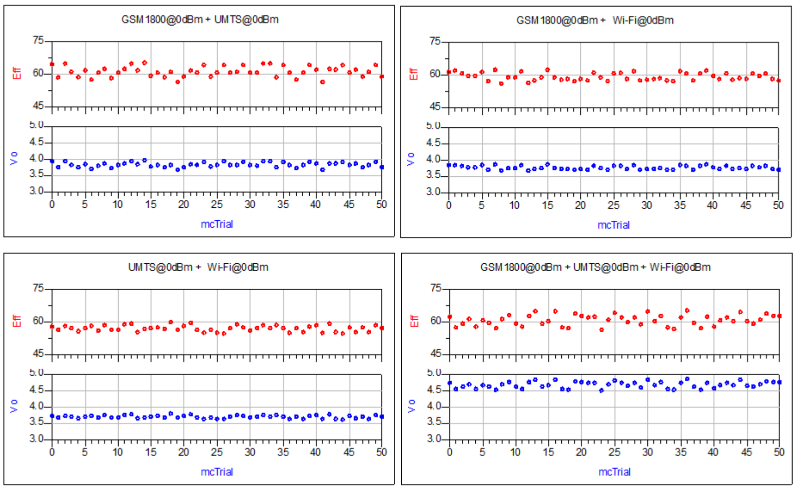

Fig.3.42 Performance of the rectification efficiency and the output voltage varying the matching network component values for multiple RF sources, assuming a total input power equal to 0dBm derived from the co-simulation-optimization process.

4
Solar Energy Harvesting System

The limited battery lifetime of wireless sensor network, necessitates frequent battery recharging or replacement. Solar energy harvesting is an attractive solutions to increase the autonomy of these systems.

In this chapter, we present a battery-less solar-harvesting circuit able to supply a sensors for low-power applications. The harvester, composed of small size KXOB22-12X1 cells and a DC-DC regulator, performs maximum-power-point control of solar energy with high efficiency.

4.1 Principle of power generation

The principle of power generation consists of the utilization of the photovoltaic effect in semiconductors.

When the sunlight or any other light of proper wavelength is incident upon a semiconductor surface, the electrons present in the valence band absorb energy and, being excited, jump to the conduction band and become free. These highly excited, non-thermal, electrons diffuse and some reach a junction where they are accelerated into a different material by a built-in potential. This generates an electromotive force, and thus some of the light energy is converted into electric energy [80].

In most photovoltaic applications the radiation is sunlight, and the devices are called solar cells.

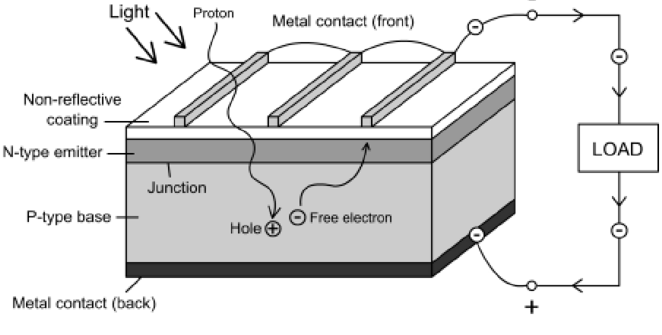

Fig. 4.1 Basic operation of photovoltaic cell.

Table 4.1 (that shows the energy in the light) together with the table 4.2 (that shows the common efficiencies for solar cells) give an idea of energy availability.

Condition	Power [mW/cm^2]
Mid-day, no clouds	100
Outdoors, overcast	5
Incandescent bulb 3m away	10
Compact Fluorescent Lamp 3m away	1

Tab. 4.1 Power available in different types of light [81].

Solar Panel	Efficiency [%]
Silicon	25
GaAs	26.4
Amorphous Si	10.1
Organic	15.15
Multi-junction	32

Tab. 4.2 Photovoltaic technologies and their reported maximum efficiencies [82].

4.2 Architecture for the Solar Energy Harvesting

4.2.1 Solar Cells

The solar cell is a p-n junction semiconductor as shown in figure 4.2. According to [83], the output voltage and current or V-I characteristics are given by (4.1):

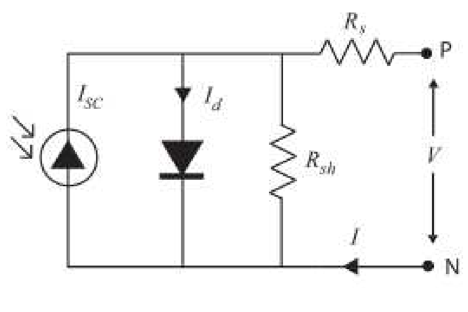

Fig. 4.2 Equivalent electrical circuit of a solar cell.

$$I = I_{SC} - I_d \cdot \left(e^{\left(\frac{q(V+R_S I)}{nkT}\right)} - 1\right) - \left(\frac{V + R_S I}{R_{sh}}\right) \tag{4.1}$$

where

- V is the output voltage;
- I is current respectively;
- R_S is a series resistance of the cell;
- R_{SH} is a shunt resistance of the cell;
- q is the electron charge;
- I_{SC} is the photon-generated current;
- Id is the reverse saturation current;
- n is a dimensionless factor;
- k is Boltzman's constant;
- T is the temperature in Kelvin (K).

The output characteristics of solar cells are expressed through voltage-current (V-I) or voltage-power (V-P) curves (figure 4.3). Varying a load resistance from zero to a high impedance and measuring the relative current and voltage, the V-I and V-P curves are achieved.

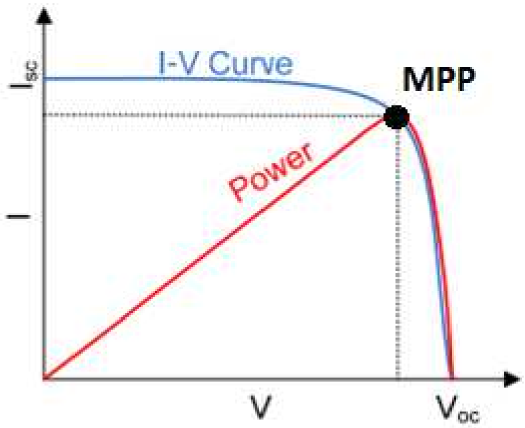

Fig. 4.3 V-I and V-P characteristics for solar cells.

Solar cells are characterized by two parameters, the open-circuit voltage (V_{OC}) and short-circuit current (I_{SC}). The point at which the V-I curve and resistance

(R_L) intersects is the operating point of the solar cell and the relative voltage and current are V_{MPP} and I_{MPP}. The product of V_{MPP} and I_{MPP} produce a maximum power point (MPP) for the solar cell.

In the present work, three solar cells KXOB22-12X1 of IXYS [84] have been used. The exposure area of each cell is very small (120μm^2) as shown in figure 4.4 and in table 4.3.

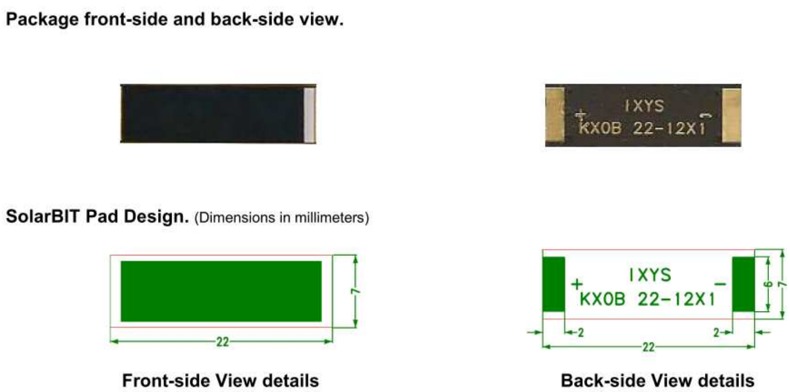

Fig.4.4 KXOB22-12X1 solar cell dimensions.

Parameter	KXOB22-12X1 SOLAR CELL
V_{OC} [V]	0.63
I_{SC} [mA]	50
P_{MAX} [mW]	22.3
V_{MAX} [V]	0.5
I_{MAX} [mA]	44.6
Current Density	42.4
Fill Factor [%]	>70
Efficiency [%]	22
Dimension [mm]	20 x 7 x 1.8
Unit Cell Size [mm]	20 x 6
Cell in series	1
Weight [g]	0.5

Tab.4.3 KXOB22-12X1 solar cell parameters.

As reported in the datasheet [84], the solar cell has the following characteristic **J** (current density) / **V** (voltage) and **V** (voltage) / **P** (power density)

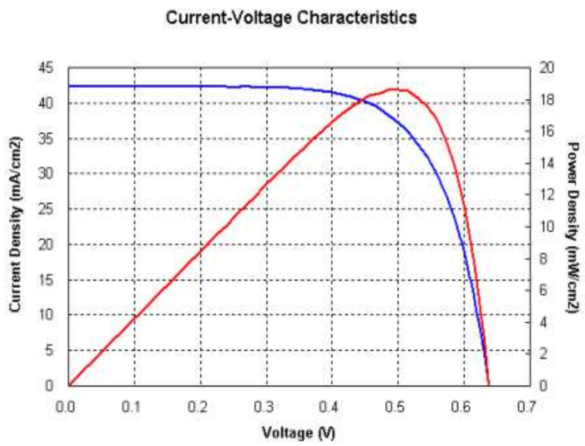

Fig.4.5 V-I and V-P curves for KXOB22-12X1solar cell.

With the solar cell size of 0.00012m^2 (20mm x 6mm), the total maximum power that can be harvested is 22.3mW. Furthermore, the variation of the open circuit voltage for varying solar radiation (expressed in W/m^2) is shown in figure 4.6.

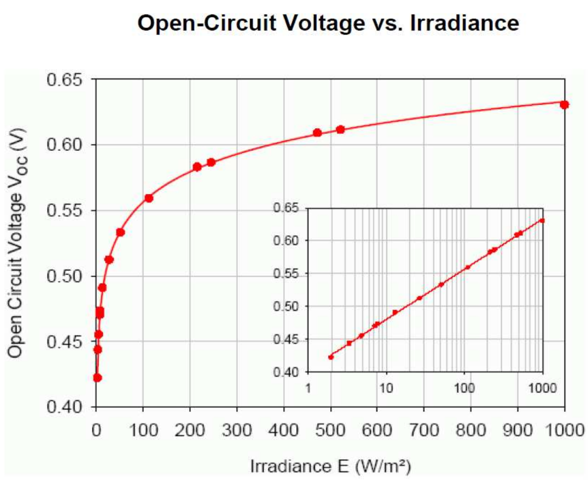

Fig.4.6 Open circuit voltage varying the irradiance solar for KXOB22-12X1 solar cell.

The figure 4.5 shows the solar cell I-V characteristic and as it is seen the solar cell has a maximum power point. This point can be tracked by several MPPT techniques. In fact, the maximum power, in optimal conditions of light (clear sky), is 22.3mW obtained with an J_{MAX} = 44.6 mA/cm^2 and V_{MAX} = 0.5V.

4.2.1.1 Solar Cell Characterization

In order to verify the solar cell characteristics, it has been characterized in indoor and outdoor environment. The light intensity was carefully measured by Luxometer. Exposing the cell to different lighting conditions, was measured the open circuit voltage V_{OC} across the terminals.

The energy in the light at the test site is defined as 683 lux corresponds to $1 W/m^2$. In these conditions, were found four special cases:

- 1.475 W/m^2 that corresponds to outdoor light with clear sky.
- 500 W/m^2 that corresponds to outdoor light with overcast sky.
- 95 W/m^2 that corresponds to inside light by a window.
- 4 W/m^2 that corresponds to low artificial light inside an office.

The results show in figure 4.7, are comparable with those reported in figure 4.6.

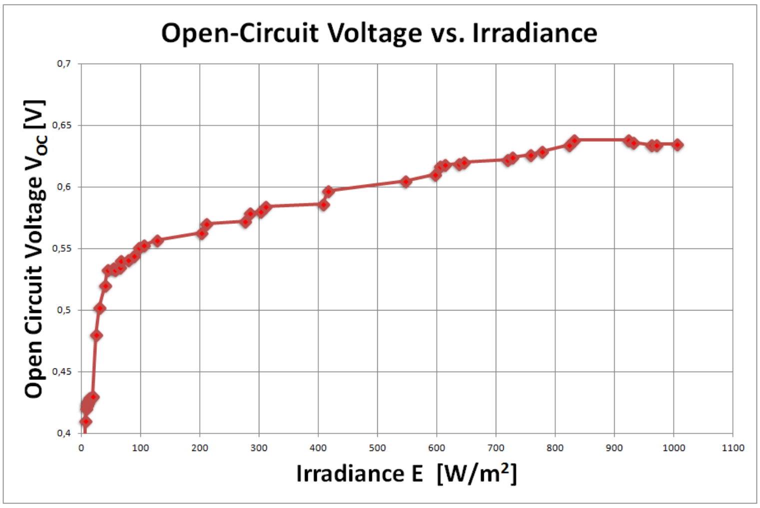

Fig.4.7 Sperimential characterization of KXOB22-12X1 Solar Cell.

The minimum irradiance E_{MIN} in order to obtain the maximum output power cell is:

$$E_{MIN}\left[\frac{W}{m^2}\right] = \frac{P_{MAX}[W]}{\eta \cdot A_{EFF}[m^2]} = \frac{22.3 \cdot 10^{-3} W}{0.22 \cdot (1.2 \cdot 10^{-4} m^2)} = 844{,}69\left[\frac{W}{m^2}\right] \quad (4.2)$$

Considering that

$$1lux = \frac{1lumen}{m^2} = \frac{1}{683}\left[\frac{W}{m^2}\right] \quad (4.3)$$

$$1W = 683lumen \quad (4.4)$$

the minimum irradiance expressed in lux is:

$$E_{MIN}\,[lux] = 844{,}69 \cdot 683\left[\frac{W}{m^2}\right] = 576.928\,[lux] \quad (4.5)$$

For an irradiance value higher than E_{MIN}, the output power cell will stay at a constant value of 22.3mW.

In these conditions, assuming an average illumination, for example 10 hours, the total power harvested would be

$$E_{Solar\_Cell} = P_{out\_Solar\_Cell} * 10hours[mW] = 22.3[mW] * 36000[s] = 803[J] \quad (4.6)$$

which is enough for our ULP sensors load.

Identified the solar cell, the next step was to identify the spice model to be used for the architecture of the Solar Energy harvesting circuit. The equivalent spice model of the solar cell is shown in figure 4.8.

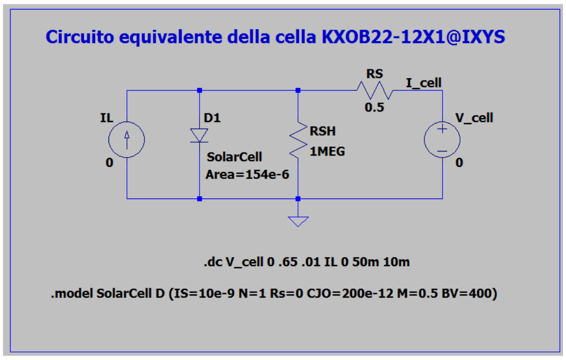

Fig.4.8 Spice model for KXOB22-12X1 solar cell.

It consists of a current generator IL (which depends on the irradiation conditions), a real diode and two resistances (series and shunt resistance of the cell). Using the LTSpice (Linear Technology) circuit simulation software and performing a DC sweep simulation, it was obtained the following I-V characteristic:

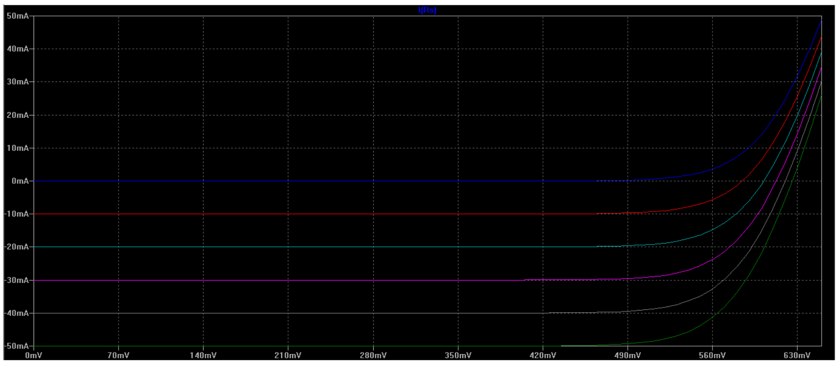

Fig.4.9 I-V characteristic for the KXOB22-12X1 solar cell.

A single cell produces only 0.5V and thus needs a low voltage boost converter to operate.

4.2.2 Step-Up DC/DC Converter

In the market, there are many DC-DC converters can be used for solar cells, but not all offer a high output power and a low VMPPC voltage maximum power point control. The LTC3105 [85] integrated step-up circuit from Linear Technology has been designed in order to meet these characteristics.

This converter was chosen to be implemented as the power converter for the KXOB22-12X1-solar cell.

The LTC3105 is synchronous boost converter that incorporates Maximum Power Point Control (using a programmable MPPC threshold), and an integrated LDO regulator. This converter is able to operate on a wide range of input voltages from 225mV to 5V.

The LTC3105 starts by charging the CAUX pin until this reaches 1.4V . In this phase the MPPC is not yet enabled. When VAUX voltage is equal to 1.4V the converter starts to regulate the LDO output. When this is done, the COUT capacitor is charged. (see figure 4.11 for the waveforms).

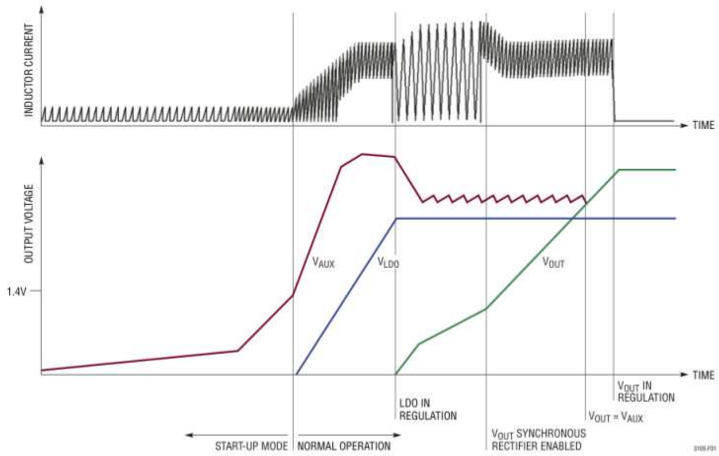

Fig. 4.10 Waveforms in the LTC3105 from datasheet.

The MPPC circuit allows the user to set the optimal input voltage operating point for a given power source. The MPPC circuit dynamically regulates the average inductor current to prevent the input voltage from dropping below the MPPC threshold. In fact, this circuit is able to controls the inductor current in order to maintain V_{IN} at the voltage on the MPPC pin.

In figure 4.11 is showed the overall solar energy harvesting architecture implemented in the Linear Technologies simulator.

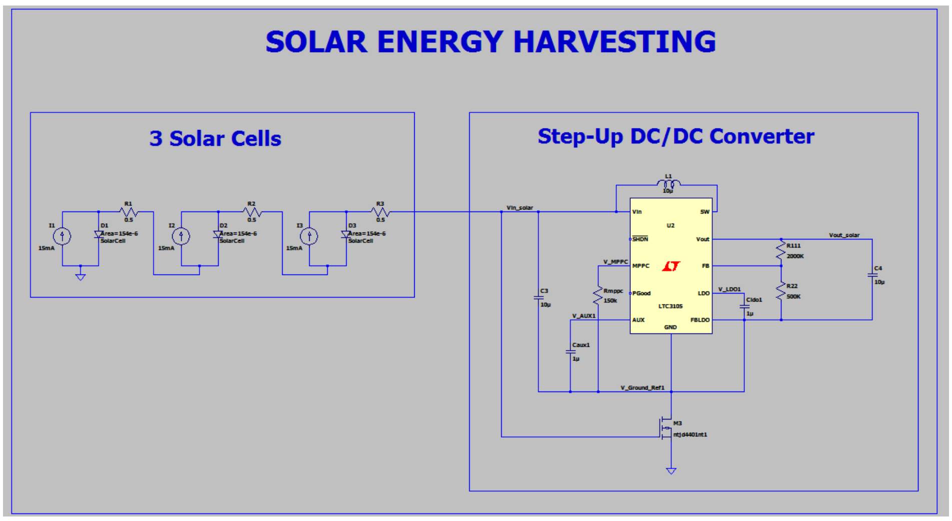

Fig. 4.11 Solar energy harvesting architecture.

4.2.2.1 Component Selection

In this section, the components shown in figure 4.11 are chosen. For the feedback inductor, low series resistance power inductors with values

between 4.7μH and 30μH are recommended. If the series resistance is too high, efficiency will be reduced and the V_{MPPC} voltage will increase.
In many applications, a 10μH inductor is chosen. Moreover, this one must have a high saturation current.
The MPPC voltage pin is set by connecting a resistor between the MPPC pin and GND, as shown in figure 4.12.

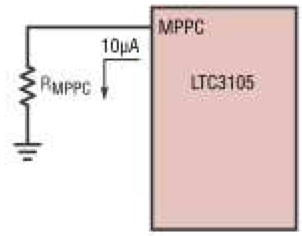

Fig. 4.12 MPPC Configuration.

The MPPC voltage is determined by the equation:

$$V_{MPPC} = 10\mu A \cdot R_{MPPC} \tag{4.3}$$

Setting the desired operating voltage of the solar cell at 0.5V, the MPPC voltage V_{MMPC} is 1.5V (because in input to LTC3105 there is three solar cell connected in series). In this way, the R_{MPPC} resistor was fixed to 150kΩ.

Input capacitor selection is highly important in low voltage. In many applications, a 10μF ceramic capacitor is recommended between V_{IN} and GND. A 1μF C_{AUX} ceramic capacitor is recommended between AUX pin and GND, while a minimum 10 μF C_{OUT} ceramic capacitor is recommended between V_{OUT} and GND with low ESR.

A resistor divider connected between the V_{OUT} and FB pins determines the step-up converter output voltage, as shown in figure 4.11. The equation for V_{OUT} is:

$$V_{OUT} = 1.004V \cdot \left(\frac{R_1}{R_2} + 1\right) \tag{4.4}$$

The open circuit voltage is fixed to 5V setting R1=2MΩ e R2=500kΩ. Finally, between LTC3105 and GND, a N-Mosfet was inserted in order to maximize the power consumption as long as the input voltage does not exceed the threshold voltage of the N-Mosfet, the LTC3105 regulator will not turn on. In figure 4.17, it is possible to show the Mosfet.

4.3 Simulations

Selected and sized all the components that constitute the system architecture (figure 4.13), we passed to the simulation step. Several simulations were performed as a function of photo-generated current of each solar cell. In particular, the current generators that represent the three solar cells have been set to a value of 15mA, intermediate compared to what they can actually deliver. This value corresponds to the value of the photo generated current by the solar cell in conditions of outdoor light overcast.

In fact, in ideal conditions of irradiation, each cell can deliver more than 44.6mA while in the case where the radiation conditions are hostile (obviously excluding the evening hours) can deliver up 1-2mA.

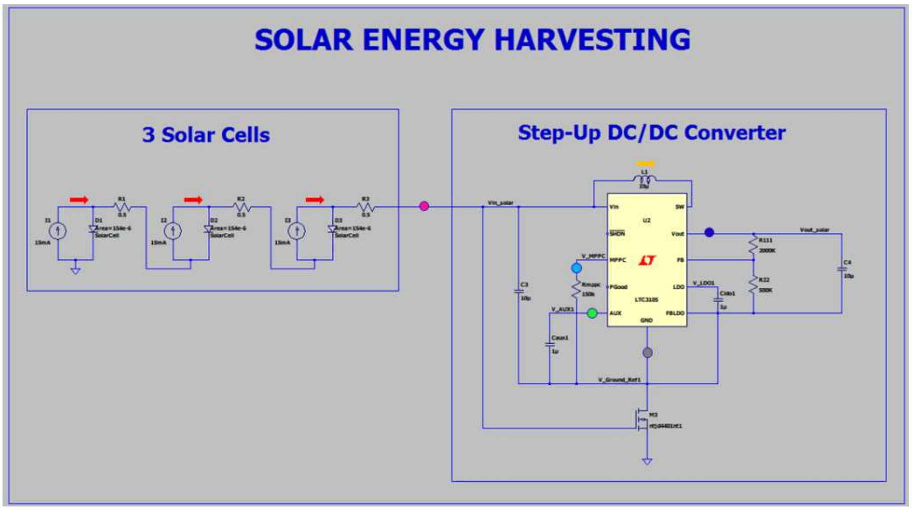

Fig. 4.13 Solar energy harvesting architecture.

The performance of the input/output voltages of the DC-DC regulator and V_{MMPC} voltage are shown in figure 4.14.

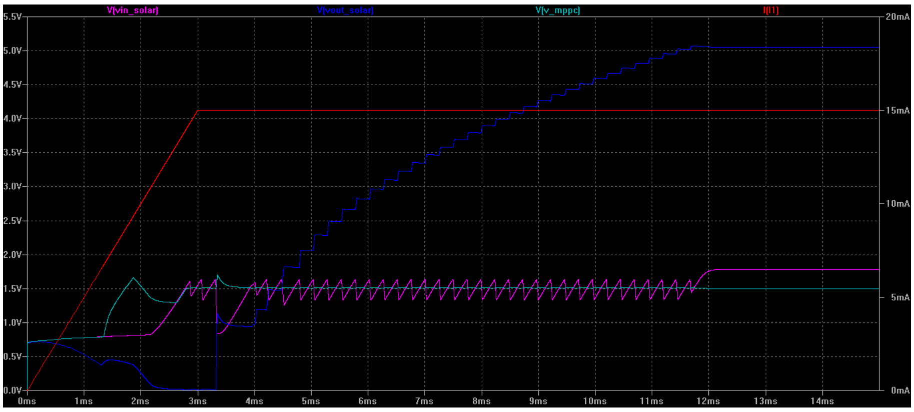

Fig. 4.14 Input/output voltage for the IC LTC3105.

As can be seen in figure 4.15, in regime condition, the V_{OUT_SOLAR} output voltage is 4.1V while, the V_{IN_SOLAR} input voltage is comparable with that of V_{MMPC} in such a way that the integrated circuit LTC3105 regulate the feedback current (IL1) required to increase the output voltage. This detail is evident in figure 4.15.

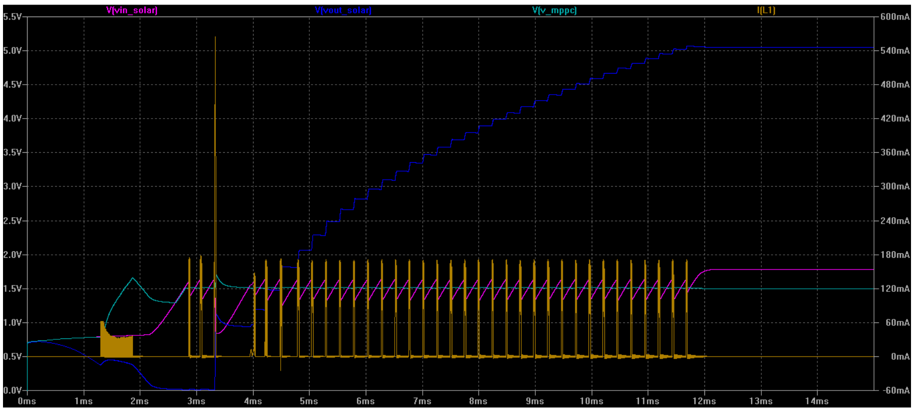

Fig. 4.15 Inductor current IL1 during the output voltage regulation phase.

In figure 4.16 is possible to note the operation of the ntjd4401 mosfet during start-up. In fact, in this phase, the mosfet disconnects the LTC3105 integrated circuit from the GND. When the input voltage of the system (V_{IN_SOLAR}) is greater than the threshold voltage of the mosfet (0.9V), it connects the integrated circuit to GND. In this way, it is possible to optimize the regulation phase of the output voltage. It is also possible to note how, in line with what is reported in the datasheet, the output voltage begins to increase when the voltage on the capacitor C_{AUX} reaches 2.6V.

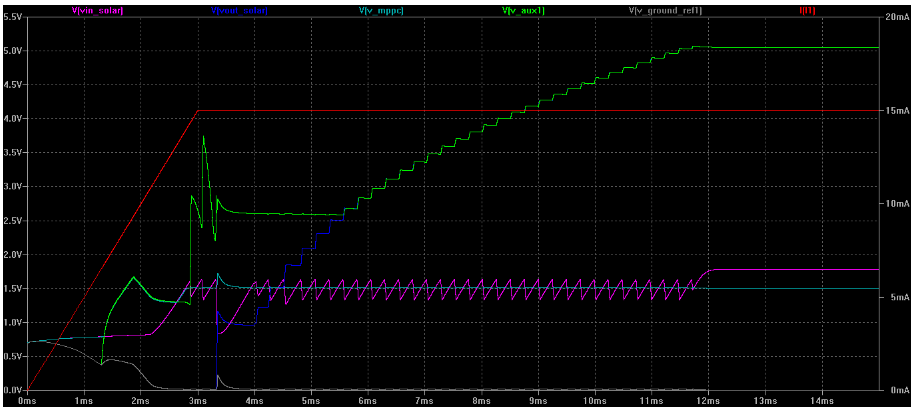

Fig. 4.16 LTC3105 waveforms.

Finally, the whole architecture was simulated in different conditions of irradiation: maximum light intensity which corresponds to a value of photo-generated current of 44.5mA for solar cell and a minimum luminous intensity (ensuring an output voltage of 5.1V) which corresponds to a value of photo-generated current of 1mA. In these two extreme conditions, the output voltage reaches the regime voltage after 4ms and 90ms respectively.

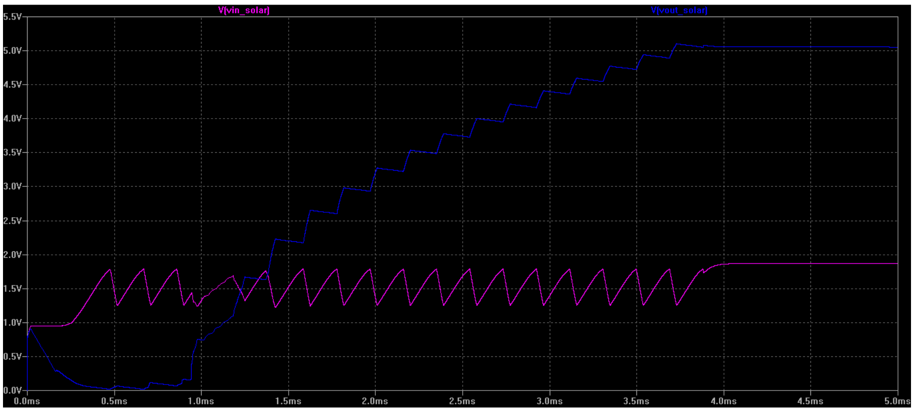

Fig. 4.17 Input-Output LTC3105 waveforms @44.5mA solar cell current.

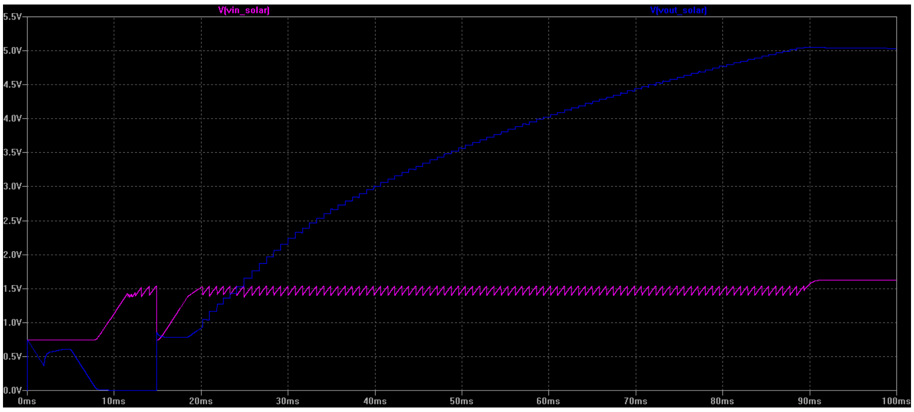

Fig. 4.18 Input-Output LTC3105 waveforms @2mA solar cell current.

4.4 Scavenging efficiency

LTC3105 performs a so called Maximum Power Point Control, which is a quite limited method of making sure to keep the solar cell at its maximum power output. The method is to set the desired operating voltage via a resistor R_{MMPC} on the MPPC pin, where there is a reference current of 10µA, and then the IC will make sure to operate the input at this fixed voltage level. This solution cannot track the MPP when the light intensity changes and this is very important for outdoors harvesting, as the light intensity is very fluctuating. As the MPPC outputs just a reference voltage, one could connect another circuit for tracking it (remembering to take the 10µA into account). In order to evaluate the LTC3105 efficiency, the input power to the system (by varying the current of each solar cell from 2mA to 45mA) and the output power transferred to a capacitor of 10uF, has been calculated as follows:

$$P_{out\_avg} = \frac{E}{\Delta t} = \frac{1}{\Delta t} \cdot \left(\frac{1}{2} C[(V_{MAX})^2 - (V_{MIN})^2]\right) \qquad (4.4)$$

where C is a 10uF output capacitor, V_{MAX} and V_{MIN} are respectively the 90% and 10% of the value of the output voltage. In this case, since V_{OUT} is set to 5V, the values V_{MAX} and V_{MIN} correspond to 4.5V and 0.5V. Δt is, instead, the time required by the output voltage to go from 10% to 90% of its steady state value.

The system input power was calculated as the sum of the output power of each solar cell (for different values of the current photo-generated). All the details are shown in table 4.4.

Iout_cell [mA]	Pout_cell [mW]	Pout LTC3105 [mW]	η LTC3105 [%]
2	0,8	1,7	70,3
5	2,2	4,9	71,8
10	4,6	10,0	72,7
15	7,0	15,6	74,7
20	9,3	20,7	74,4
25	11,6	26,9	77,5
30	13,8	31,6	76,4
35	16,0	36,9	77,0
40	18,0	41,7	77,2
45	20,0	46,5	77,5

Tab. 4.4 LTC3105 efficiency calculated varying the solar cell output current.

In this way, the LTC3105 regulator efficiency is defined as follows:

$$\eta_{LTC3105} = \frac{P_{out\_LTC3105}}{3 * P_{out\_cell}} \tag{4.5}$$

The figure 4.19 shows the trend of the LTC3105 regulator efficiency varying the current photo-generated by each solar cell (from 2mA to 60mA). As can be seen, the efficiency is always higher than 70% in agreement with what declared in datasheet [84].

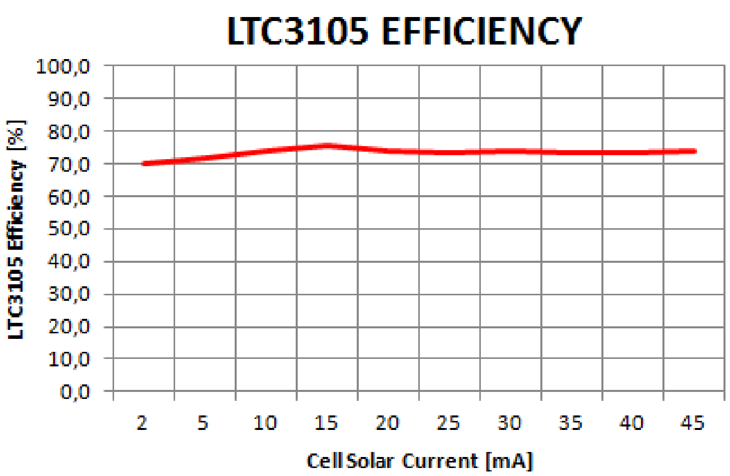

Fig. 4.19 LTC3105 efficiency calculated through (4.5).

After the design of the RF and Solar Energy Harvesting circuits, the next step was to connect both the circuits in input to the LTC3108 power manager which has the task of manage the input power recovered and to supply, directly or using a supercapacitor (previously loaded), the WSN node.

5

RF-Solar Energy Harvesting Architecture with Power Management

The characteristics and power output capabilities of both the rectenna and the solar cells were determined and discussed in chapters 3 and 4 respectively. With the knowledge of experimental data gathered from these two energy sources, the prototype of a power management system can now be designed. This chapter details the development of such a system.

5.1 Overview

Figure 5.1 shows a block representation of the proposed power management system. The system is capable of harvesting energy from solar radiation (E_S) and Radio Frequency electromagnetic waves (E_{RF}). These circuits were designed separately in the previous sections.

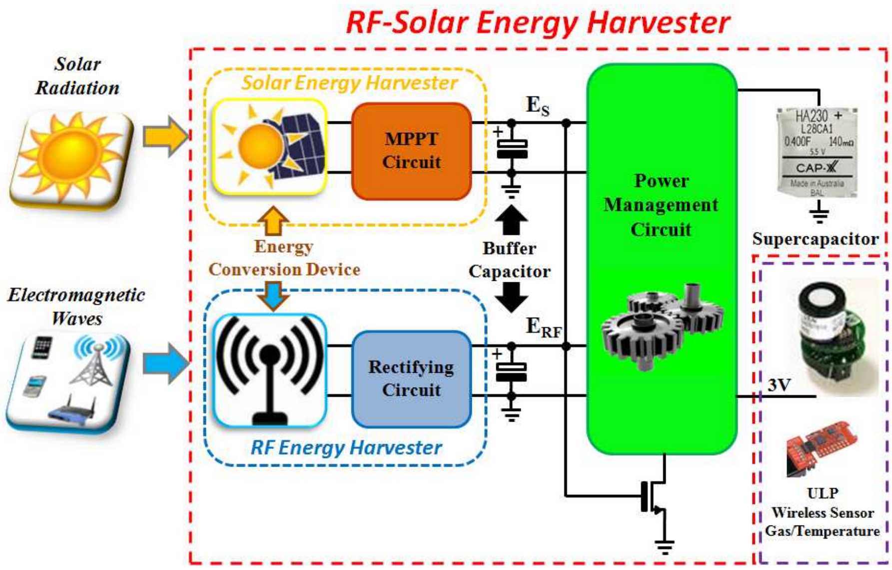

Fig. 5.1 RF- Solar energy harvester with power management circuit.

Both E_S and E_{RF} are harvested through their respective converters and stored separately. The system is capable of efficiently harvesting energy as well as producing a regulated output suitable for the load, in this case the wireless sensor node.

The LTC3108 integrated circuit by Linear Technologies is used as the power management circuit. It is designed to accumulate and manage energy over a long period of time to enable short power bursts for acquiring and transmitting data. The bursts must occur at a low enough duty cycle such that the total output energy during the burst does not exceed the average source power integrated over the accumulation time between bursts.

Finally, the load is powered by the output capacitor and supercapacitor connected to the system.

5.2 Ultra Low Power Sensor Load assessment

The proposed energy harvesting system was designed to supply, without the use of battery, two WSN nodes:

- eZ430-RF2500 wireless sensors temperature (WST) of TI [1];
- Gas (CO) Sensor Platform with Bluetooth low-energy [2];

For both WSN nodes, the energy characteristics and the current absorption trend are respectively listed and show in tables 5.1-5.2.

Wireless Sensor Temperature	
Parameters	**Value**
Supply voltage	3.3 [V]
Sleep mode current	1.3[μA]
Average active mode current	10.51 [mA]
Average current consumption	36.80 [μA]
Duration in active mode	2.838 [ms]
Frequency	1 [Hz]
Total power consumption	121.44 [μW]

Tab. 5.1 Energy characteristics of the wireless sensor temperature.

Wireless Sensor Gas	
Parameters	**Value**
Supply voltage	3.3 [V]
Sleep mode current	1.1[μA]
Average active mode current	8.531 [mA]
Average current consumption	23 [μA]
Duration in active mode	2.675 [ms]
Frequency	1 [Hz]
Total power consumption	75.9 [μW]

Tab. 5.2 Energy characteristics of the wireless sensor gas.

Because it is not possible to simulate directly these sensors (Spice model is not available), the load utilized as sensor is a resistive one with an absorption current shown in [1-2]. For this reason, the current absorption profiles were represented through a PWL curves as show in figure 5.2 and 5.3.

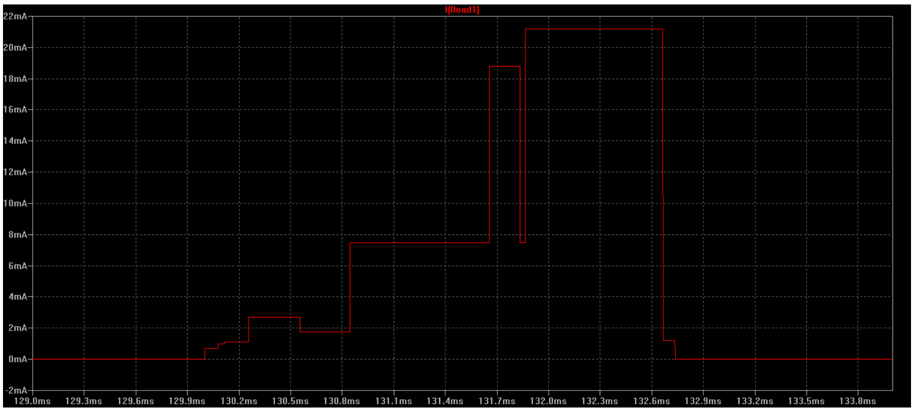

Fig. 5.2 Spice model for the temperature sensor transmission current profile.

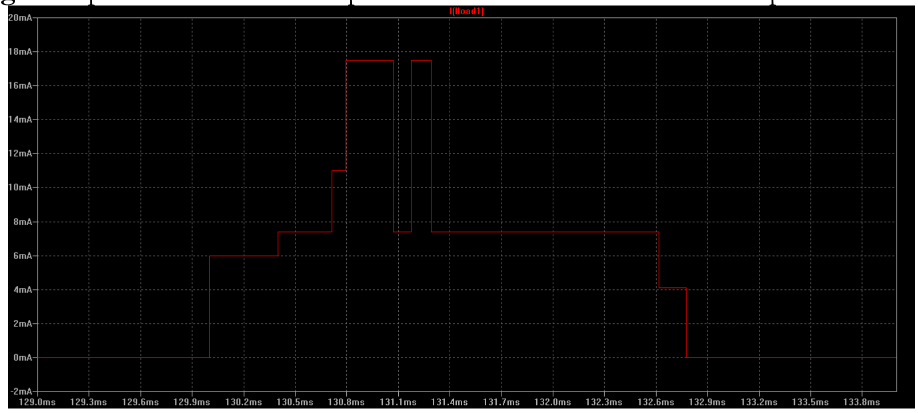

Fig. 5.3 Spice model for the gas sensor transmission current profile.

To ensure sustained operation, the following condition needs to be true:

$$P_G \geq P_C \tag{5.1}$$

where P_G and P_C are the generated and consumed mean power respectively. Considering D a duty-cycle of the WSN node, the required generated mean power is given as:

$$P_G \geq (1 - D)P_{sleep} + DP_{active} \tag{5.2}$$

For example, for the WST the generated mean power would have to be equal or more than 121.44µW for sustained operation.

$$E_C = P_C * T_{STORE} = 121.44\ \mu W * 86400\ s = 10.5\ J \tag{5.3}$$

Considering a supercapacitor with operating voltage of 5.25V with the minimum operating voltage 3.3V (supply voltage of WSN nodes), the capacitance value required to supply the sensor for one day is given by

$$C_{STORE} = \frac{2 * E_C}{V_{MAX}^2 - V_{MIN}^2} = \frac{2 * 10.5\ J}{16.67\ V^2} = 1.26\ F \tag{5.4}$$

Instead, considering the Wireless Sensor Gas (WSG) load and T_{STORE} = 1 day, the C_{STORE} capacitance storage value is

$$C_{STORE} = \frac{2 * E_C}{V_{MAX}^2 - V_{MIN}^2} = \frac{2 * 10.5\ J}{16.67\ V^2} = 787\ mF \tag{5.5}$$

This value is lower than previous ones because the total power consumption value is smaller than that of wireless sensor temperature.

5.3 Power Management

In energy harvesting applications, in order to efficiently manage the energy harvested is necessary to utilize an IC power manager. As a power management component was chosen, an integrated circuit was provided by Linear Technologies, LTC3108 [85]. It is designed to accumulate and manage energy over a long period of time to enable short power bursts in order to supply lo load. The PGD signal can be used to enable other circuitry when V_{OUT} reaches regulation, indicating that enough energy to hold up the power bursts.

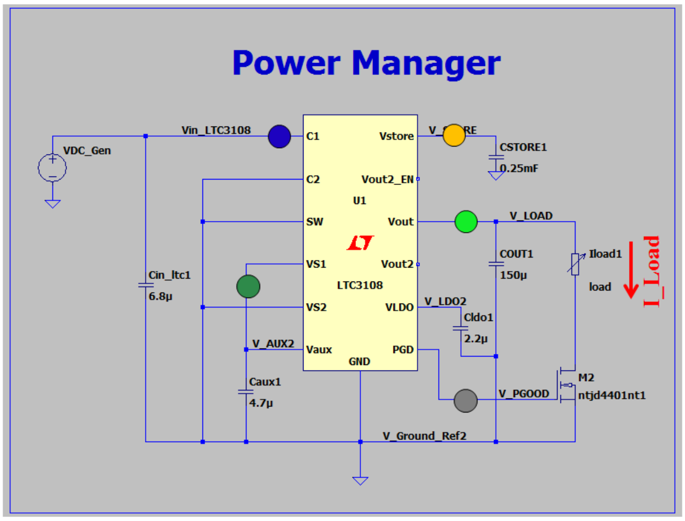

Fig.5.4 LTC3108 power management.

The output voltage value can be programmed setting the voltages on pins VS1 and VS2 [85].

In order to demonstrate the efficiency and the benefits of the LTC3108 circuit, an ad-hoc example has been reported in figure 5.4. Considering a sensor gas load power by means ideal voltage generator. This is connected in input to LTC3108 circuit and it is turned-on for a short time interval (blue waveform in figure 5.5).

In particular, the generator is turned-on for 15s. In this period, the voltage V_{LOAD} (waveform light green in figure 5.5) reaches the 3.3V after 6.5 s. In this moment, the C_{STORE} capacitor (0.2mF) begins to charge and at same time, the PGD voltage goes from low logical value to high one. Just in this case, through a switch (M2 in figure 5.4) driven by V_{PGOOD} voltage, the sensor is active for 26s that is, up to 33s.

Between 15s and 33s, the load is powered by C_{STORE} capacitor previously charged. When the V_{STORE} voltage begins lower the V_{LAOD} voltage, the C_{STORE} ends to supply the load. For C_{STORE} values larger, the standby time of the sensor is extended. This example shows how the TLC3108 regulator manages efficiently the harvested power.

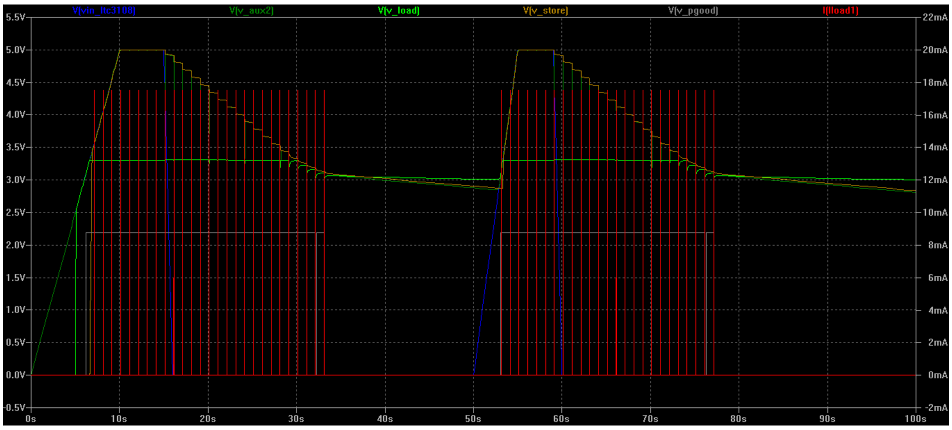

Fig.5.5 Waveform LTC3108 with V_{OUT} programmed for 3.3V.

In the WSN with very low duty-cycle, the V_{OUT} capacitor should be sized to provide the necessary current when the load is pulsed on. The capacitor value required is a function of the load current, duty-cycle and the voltage drop the circuit can tolerate.

$$C_{OUT}(mF) \geq \frac{I_{LOAD}(mA) \cdot t_{PULSE}(sec)}{\Delta V_{OUT}} \tag{5.6}$$

Obviously, during the interval between bursts, this capacitor must be charged by an input voltage source.

The C_{STORE} capacitor may be of very large value to provide energy to load when the input power is lost. Regardless of the settings for V_{OUT}, the maximum voltage for the VS_{TORE} pin is 5.25V. The C_{STORE} capacitor can be sized using the following:

$$C_{STORE} \geq \frac{[6\mu A + I_Q + I_{LDO} + (I_{BURST} \cdot t \cdot f)] \cdot T_{STORE}}{5.25 - V_{OUT}} \tag{5.7}$$

where 6µA is the quiescent current of the LTC3108, I_Q is the load on V_{OUT} in between bursts, I_{LDO} is the load on the LDO between bursts, I_{BURST} is the total load during the burst, t is the duration of the burst, f is the frequency of the bursts, T_{STORE} is the storage time required and V_{OUT} is the output voltage required.

The C_{STORE} capacitor value, for both sensors considered, were calculated in (5.4) and (5.5) for T_{STORE}=1 day

For both WSN nodes, the supply voltage is 3.3V and for this reason, the V_{OUT} voltage is set to 3.3V. The maximum allowed voltage droop during a transmit burst is 10% or 0.33V.

Considering the values in the table 5.1, the minimum required capacitance on V_{OUT} is:

$$C_{OUT}(\mu F) \geq \frac{10.51mA \cdot 2.838ms}{0.33V} = 90\mu F \tag{5.8}$$

While, considering the WSG, the minimum required capacitance on V_{OUT} is:

$$C_{OUT}(\mu F) \geq \frac{8.531mA \cdot 2.675ms}{0.33V} = 70\mu F \tag{5.9}$$

Considering both cases, a standard value of 100µF or larger could be used for C_{OUT} in this case.

The average charge current I_{CHQ} required from the LTC3108 to support the average load is

$$I_{CHQ} = I_Q + \frac{I_{BURST} \cdot t}{T} \tag{5.10}$$

where I_Q is the sleep current between bursts, I_{BURST} is the total load current during the burst, t is the duration of the burst and T is the period of the transmit burst rate.
Considering respectively the WST and WSG, the average charge current required from the LTC3108 would be:

$$I_{CHG} \geq 5\mu A + \frac{10.51mA \cdot 2.838ms}{1s} = 35\mu A \tag{5.11}$$

$$I_{CHG} \geq 5\mu A + \frac{8.531mA \cdot 2.675ms}{1s} = 22.8\mu A \tag{5.12}$$

Therefore, if the LTC3108 has an input voltage that allows it to supply a charge current respectively greater than 35µA and 22.8µA, it can support their bursts every second.

5.4 RF- Solar Energy Harvester Architecture

In this work, one of the functions of power management is to combine the harvesting circuits designed previously. In fact, the power management has two input pins: VIN and VAUX pin. This double input allows the two circuits to be independent In figure 5.6, there is shown the final architecture of the RF-Solar Energy Harvester circuit implemented in the LT simulator. It is divided in four main parts:

- Solar Energy Harvesting circuit composed of three solar cells connected to step-up DC/DC converter (LTC3105);
- RF Energy Harvesting circuit composed of rectenna connected to ultra low power comparator;
- Power management circuit;
- WSN node

All these components were analyzed, designed and dimensioned in the previous sections. Let us define the Solar Energy Harvesting Subsystem (SEHS) the combination of Solar Energy Harvesting circuit and power management while RF-Energy Harvesting Subsystem (RFEHS) is the combination of RF Energy Harvesting circuit and power management.

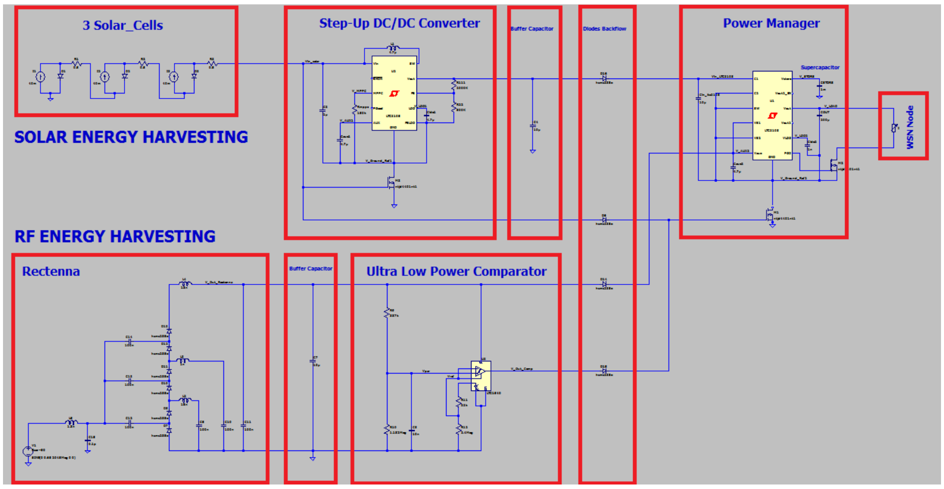

Fig.5.6 Final RF-Solar energy harvester architecture.

We now analyze separately the performance of the two individual harvesters in the presence of the power management circuit with WST and WSG loads.

5.4.1 RF Energy Harvesting subsystem performance

The RF Energy Harvesting subsystem is able to harvest energy from the following radio frequency signals:

- GSM1800@1795MHz;
- UMTS@2045MHz
- Wi-Fi@2445MHz

These signals, in the LT simulator, are represented by sinusoidal voltage generators having an internal resistance of 50Ω. Since this simulator, unlike ADS, works only in the domain of time, it must collect sufficient samples for the highest frequency component. This involves significant memory and processing requirements.

Before evaluating the performance of the RF energy harvesting with power management, it is necessity to examine the comparator waveforms (designed in the Chapter 3, par. 3.4) because it is connected with the rectenna and power management. In particular, fixed the load, the power management has been designed and the regime input resistance to the section shown in figure 5.7, must be evaluated.

In [54], have been defined the design guideline of a rectenna and in particular has been defined the rectification efficiency for varying input power. Assuming to work in optimal load condition. Fixed the RF input power (1mW) and the number of stages, the rectenna output voltage is equal to 2.8V and the rectification efficiency is around 50%. The rectenna can be considered as a voltage generator (with 5.6 V open circuit voltage and 14kΩ internal resistance) able to deliver up to 500μW when the optimal load is connected. This generator was added to the input of the comparator and power management (see fig. 5.7).

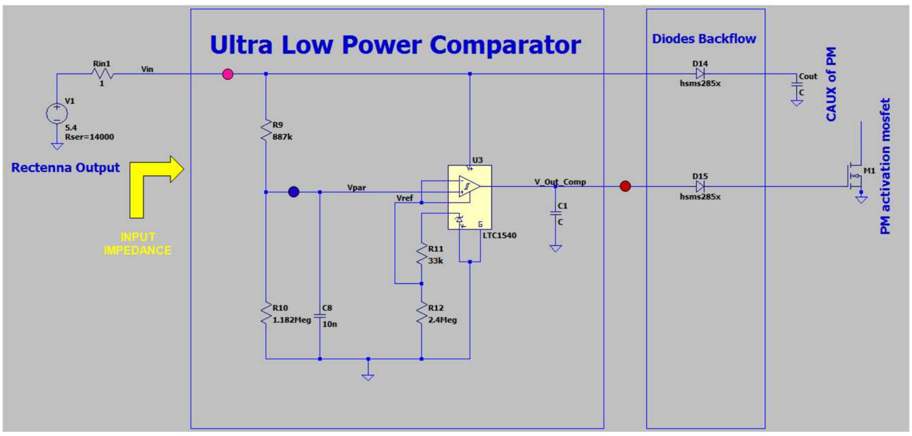

Fig.5.7 Input resistance calculation procedure for the comparator-power management circuits.

It is possible to note in the figure 5.8, that the sensor WSG (represented by the red bursts current) turns-on after 9s. The comparator goes from the high to the low logic state when the voltage of V_{PAR} exceeds the comparator reference voltage (1.18V). Moreover, as can be seen, the comparator power consumption is less than 2.2 μW. This value is in agreement with datasheet value [78]. Figure 5.9 shows a zoom of the previous simulation where the waveforms comparator are indicated.

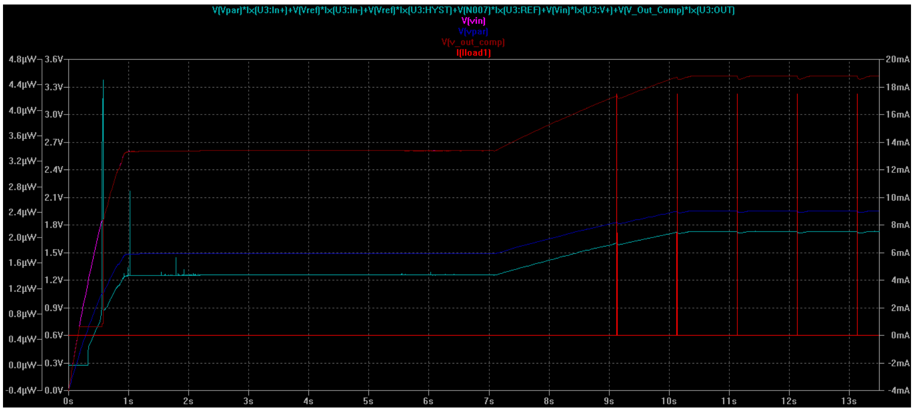

Fig.5.8 Waveforms and power consumption of the comparator (light blue waveform).

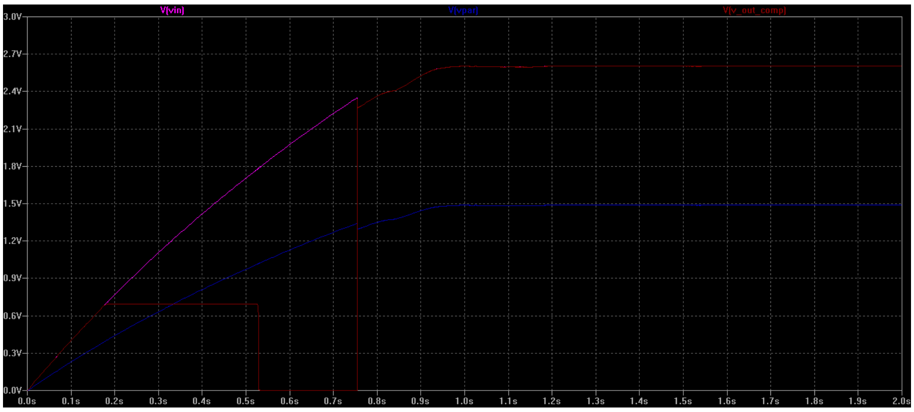

Fig.5.9 Comparator waveforms (zoom of fig-5.8).

Once verified the operation of the comparator, the input impedance of the comparator-power management is shown in figure 5.10. When V_{OUT} voltage (green waveform) increases, the input impedance average value (yellow waveform) is about 13.5kΩ. In fact, the power delivered by the input generator (520μW) is higher than 500μW (light blue in figures 5.10). Once the voltage V_{OUT} has reached 3.3V steady state value, the sensor turns-on and the average value of the input impedance is about 24kΩ. This value lowers the input generator power to 480μW. In fact, considering a mismatching between the generator internal resistance and the input impedance calculated, the comparator output voltage in steady state condition is 3.3V.

The input resistance value calculated was used as load resistive value in order to design the network matching (Cap 3, par 3.4).

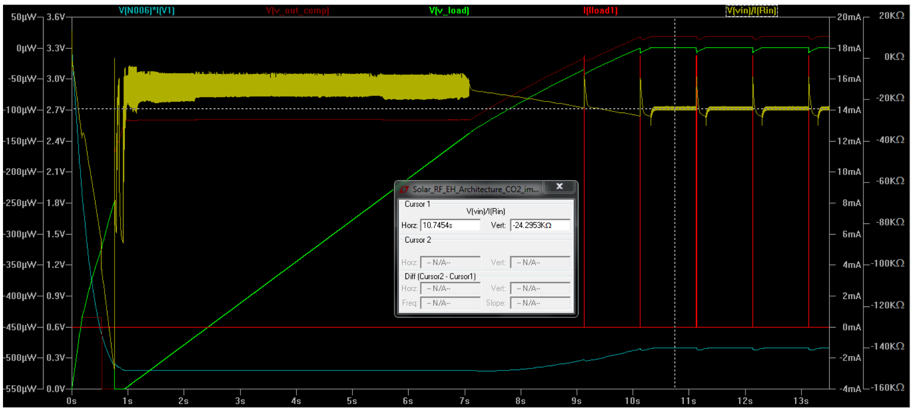

Fig.5.10 Comparator-power management input resistance (yellow waveform).

Setting the input power and the matching network of the rectifier circuit, the performance of the RF Energy Harvesting subsystem can be calculated.

To evaluate the performance, independently of the working frequency, we consider that the power generator is able to deliver up to 1mW (0dBm). Consequently, fixed the internal resistance, the maximum sinusoidal voltage is 0.65V. Furthermore, suppose that the output power from the solar cells is zero. Figure 5:11 shows the RF energy harvesting subsystem with the power management circuit.

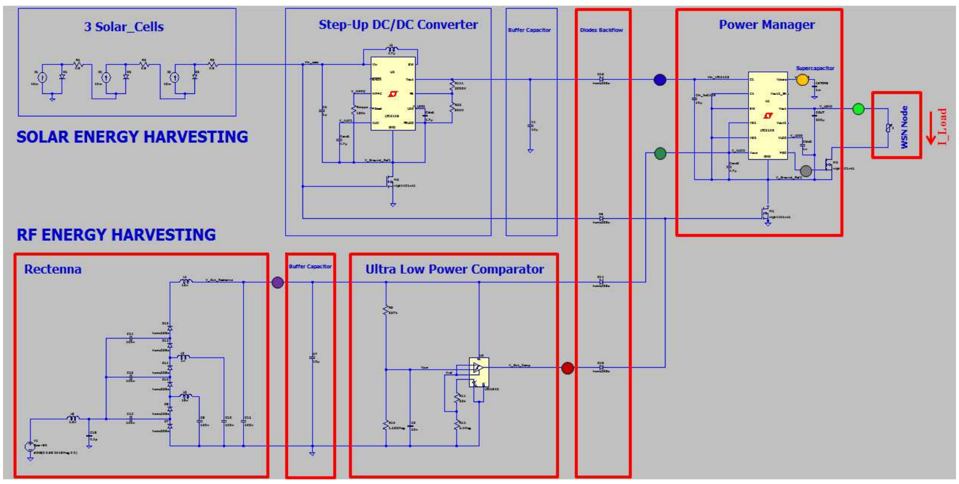

Fig.5.11 RF Energy Harvesting Sub-System.

At this point, suppose we want to supply before the WST and after the WSG: we analyze the following cases:

1. **GSM1800 Energy Harvesting with WST load**

Considering an input average power of 1mW at a frequency of 1800MHz and set the power management output voltage in order to supply the WST node to the voltage of 3.3V, the waveforms relating to the circuit of figure 5.11 are shown in Figure 5.12.

After 500ms, the rectenna output voltage is such that the comparator is turn on. This one activates the MOSFET that connects the power management to GND. The V_{OUT} voltage is brought to the voltage of 3.3V after 12 s. When V_{OUT} voltage exceeds 90% of its steady state value, the voltage V_{PDG} shifts from the low logic state to high activating the MOSFET connected in series to the WST. In this way, at 11s the WST is switched on with a periodicity of one second. Figure 5:13 shows a current burst of the sensor

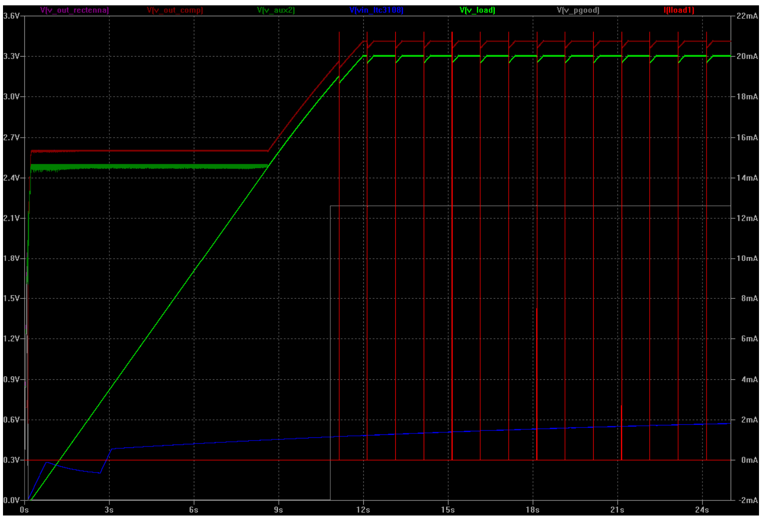

Fig.5.12 RFEHS waveforms@1800MHz-1mW input power-WST node.

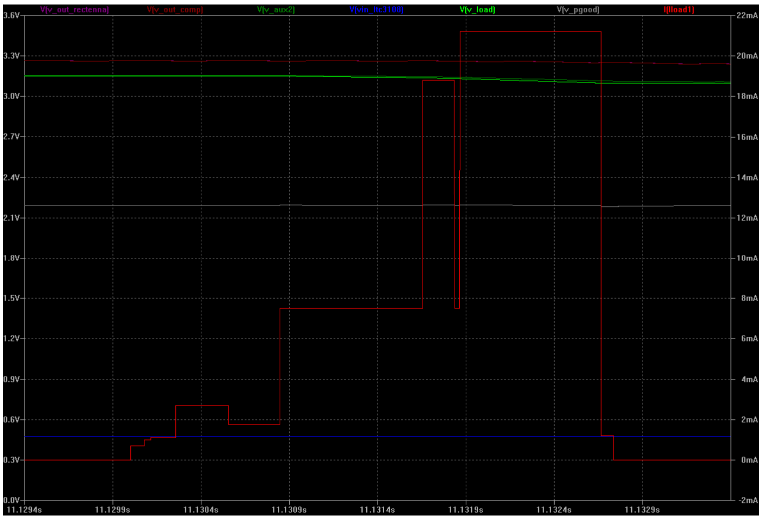

Fig.5.13 Zoom of WST current.

In these conditions, considering an output average power of the rectenna equal to 432μW (figures 5.13), the rectification efficiency is 43.2% . This value is about 7% less than that obtained with the ADS (Ch. 3, par3.6) .

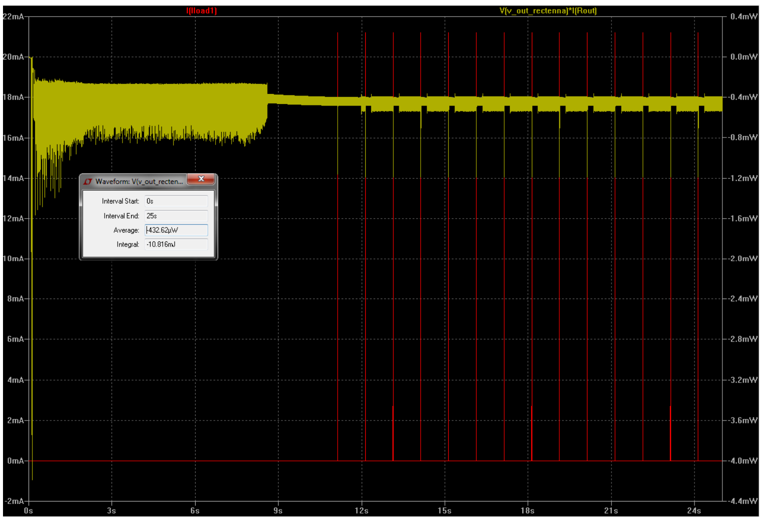

Fig.5.14 Output power of the rectifier circuit @1800MHz-1mW input power-WST node.

2. UMTS Energy Harvesting with WST load

As before, in the UMTS case, the WST node is turned-on after 10 s and the rectification efficiency of rectenna is 49%. This value is about 3% less than that obtained with ADS (Ch. 3, par3.6) .

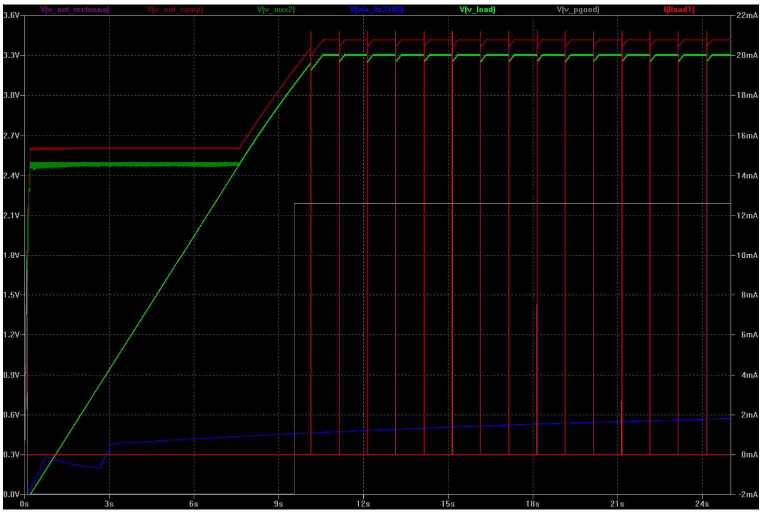

Fig.5.15 RFEHS waveforms@2045GHz-1mW input power-WST node.

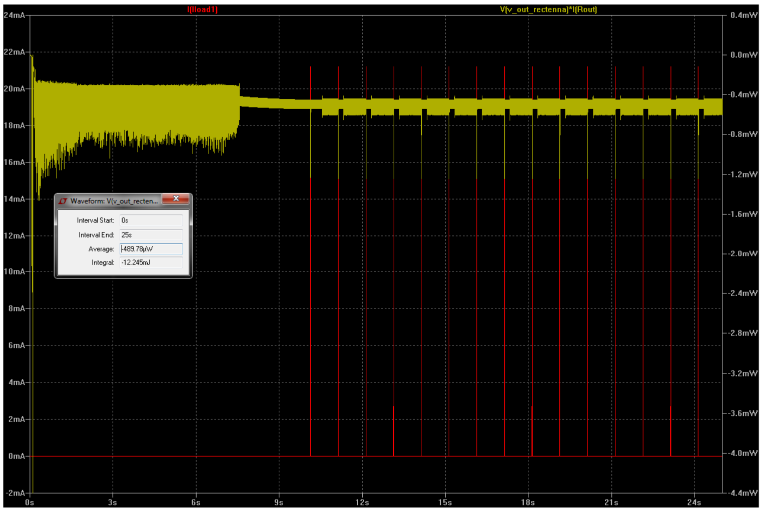

Fig.5.16 Output power of the rectifier circuit @2045MHz-1mW input power-WST node.

3. Wi-Fi Energy Harvesting with WST load

Finally, in Wi-Fi case, the WST node is turned-in after 14 s and the rectification efficiency of the rectenna is 32% This one is about 8% less than that obtained with the ADS (Ch. 3, par3.6) .

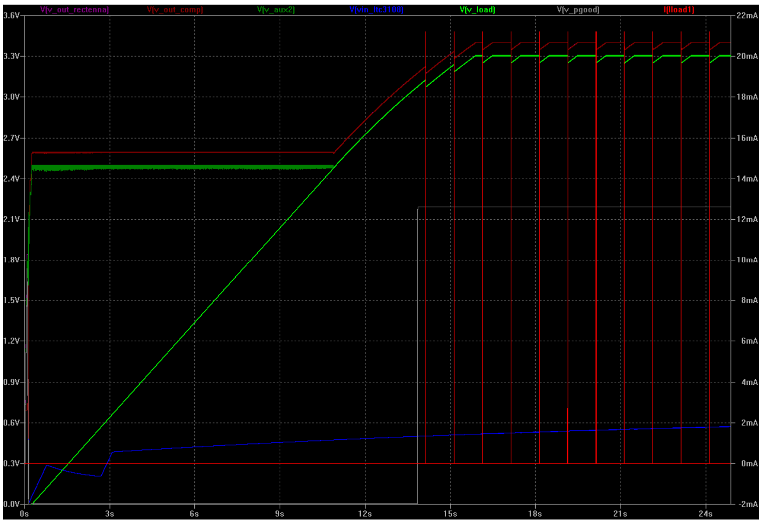

Fig.5.17 RFEHS waveforms@2445GHz-1mW input power-WST node.

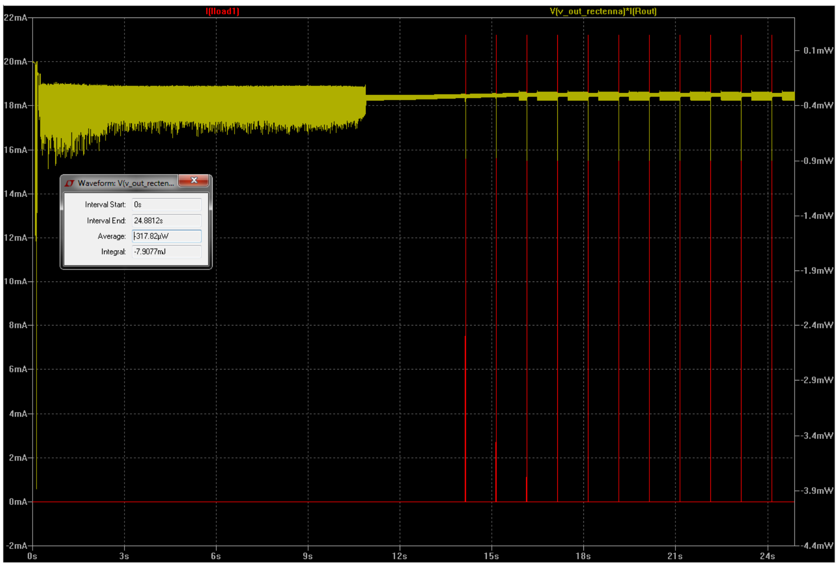

Fig.5.18 Output power of the rectifier circuit @2445MHz-1mW input power-WST node.

As the two nodes have a very similar power consumption, we have not found huge differences in the rectification efficiency and trend waveforms. For this reason, in GSM1800, UMTE and Wi-Fi cases with WSG load, only the rectification efficiencies are shown respectively in figures 5.18, 5.16 and 5.20. Finally, a comparison table is reported for all case examined.

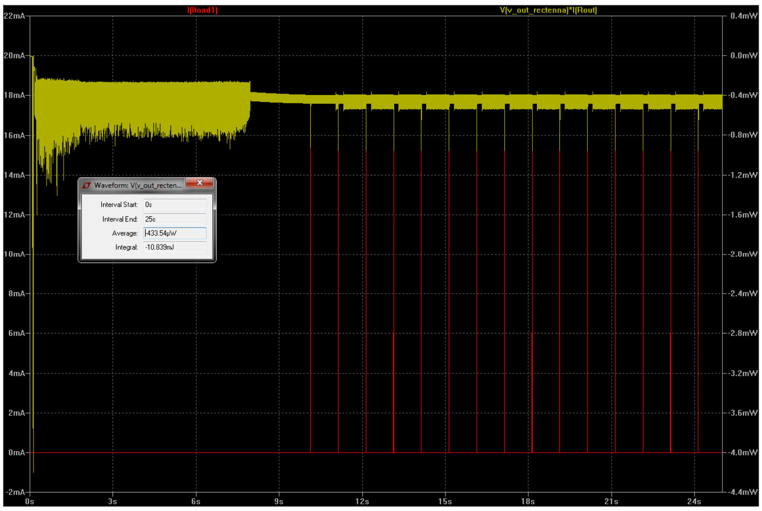

Fig.5.19 Output power of the rectifier circuit @1800MHz-1mW input power-WSG node.

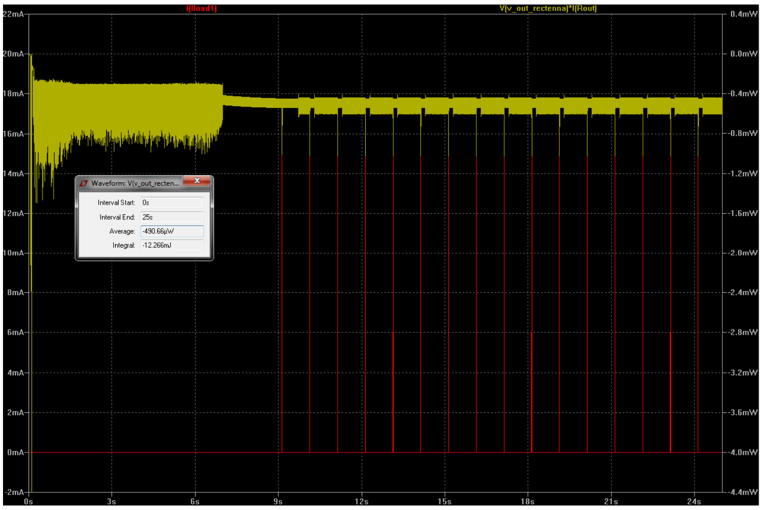

Fig.5.20 Output power of the rectifier circuit @2045MHz-1mW input power-WSG node.

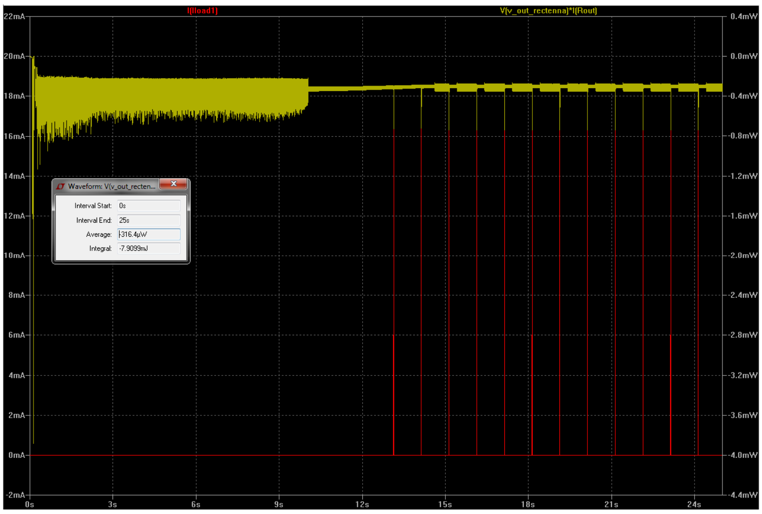

Fig.5.21 Output power of the rectifier circuit @2445MHz-1mW input power-WSG node.

	Frequency	η [%] ADS	η [%] LT	Start Turn-On [s]
WST node	GSM1800	50,37	43,36	11
	UMTS	51,91	48,98	10
	Wi-Fi	39,33	31,78	14
WSG node	GSM1800	50,37	43,35	10
	UMTS	51,91	49	9
	Wi-Fi	39,33	31.64	13

Tab. 5.3 Rectification efficiency comparison for wireless nodes between ADS an LT simulators.

5.4.2 Solar Energy Harvesting subsystem performance

In this section, a solar energy harvesting subsystem performance varying the wireless node was calculated. This time we consider that all RF voltage generators are turned-off and the current generators, that represent the solar cell, are turn on. In particular, two cases for the current of the current generator were examined.

- I=15mA (current for the outdoor light overcast)
- I=45mA (maximum current cell obtain for optimal outdoor environment condition)

According to the design developed in chapter 4, the SEHS circuit is shown in figure 5.21. Because of the enormous memory required by the LT simulator, the simulations were truncated to 150ms. In order to demonstrate the charge of the C_{STORE} capacitor, the value proceeds in (5.4) or (5.5) since they are too high, after 150ms the voltage across it is still ZERO. For this reason, for both wireless nodes, the CSTORE capacitor value has been fixed to 1mF.

Let us analyze now separately the two cases cited, varying the wireless nodes.

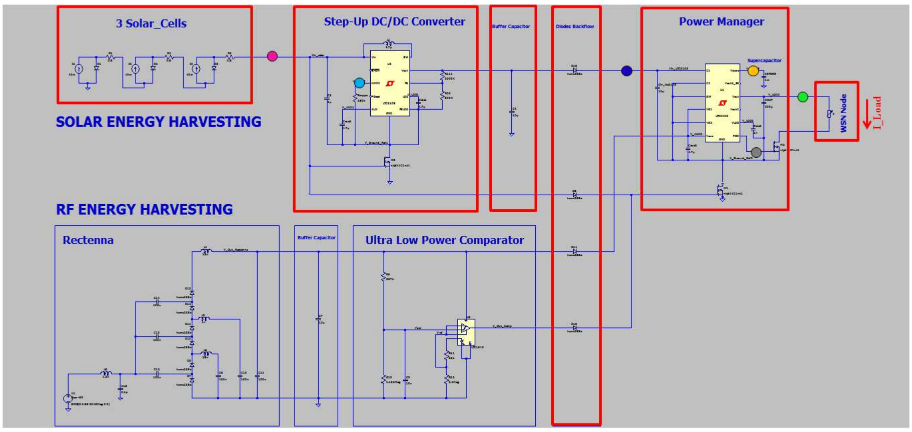

Fig.5.22 Solar Energy Harvesting Sub-System.

1. **15mA current solar cell with WST load**

Considering a 15mA output current for each solar cell and set the power management output voltage in order to supply the WST node to the voltage of 3.3V, the waveforms relating to the circuit of figure 5.10 are shown in Figure 5.21.

After 3ms, the V_{IN_SOLAR} solar cells output voltage is such that to activate the MOSFET M1 and M2 which connect respectively the LTC1305 Step-Up DC-DC converter and LTC3108 power management to GND. As designed, the V_{MPPT} voltage is brought to 1.5V thereby setting the cells working point (0.5V foe each cell).

After 3ms, the LTC3105 output voltage and LTC3108 input voltage begin to rise. In this way, also LTC3108 output voltage (V_{OUT}) increases up to 80ms where it reaches the steady state value (3.3V). When V_{OUT} voltage exceeds 90% of its steady state value, the voltage V_{PDG} shifts from the low logic state to high activating the MOSFET connected in series to the WST. In this instant, however, the WST is not switched on because it will turn on at 130ms with a periodicity of one second. In fact, at 130ms, the sensor burst current is visible in figure 5.5 Between 80ms and 130ms, because the V_{OUT} voltage has reached 3.3V, the CSTORE capacitor is charged. After the duration in active mode of the sensor, is reloaded again.

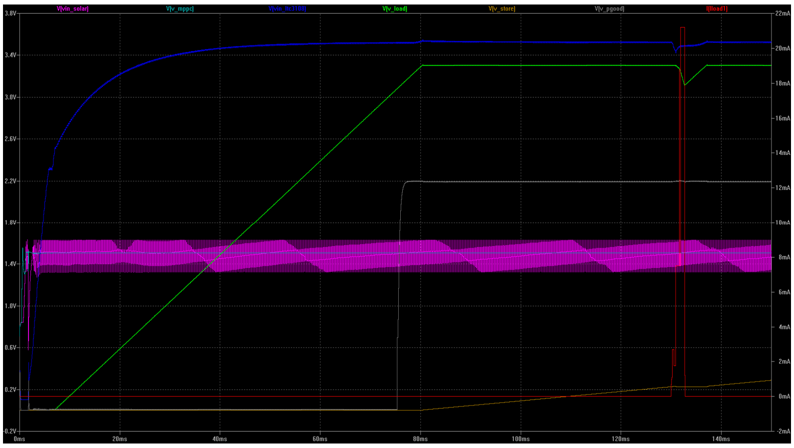

Fig.5.23 SEHS waveforms@15mA solar cell current-WST node.

Moreover, the output average powers of the solar cells and LTC3105 regulator are respectively 21.37mW and 16.74mW. Then, in this case, the efficiency of the LTC3105 regulator is 78.33%. This value is in agreements with fig 4.19.

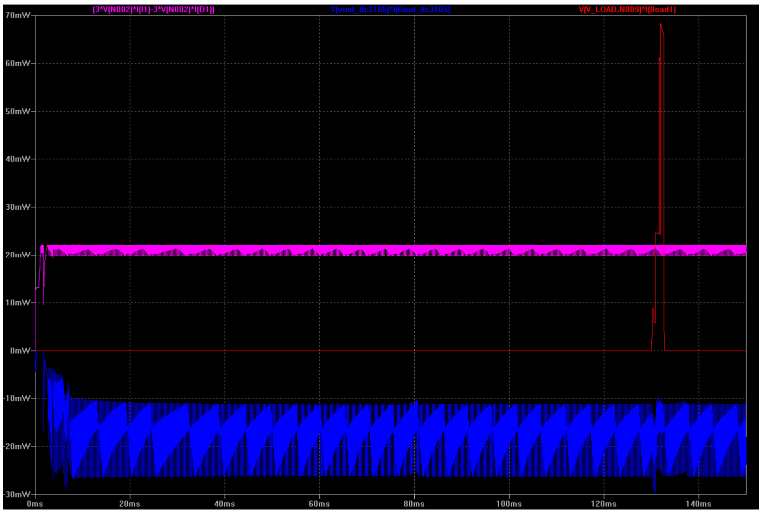

Fig.5.24 SEHS: solar cells output power (fuchsia waveform), LTC3105 output power (blue waveform) and load power consumption (red waveform) @15mA solar cell current-WST node.

2. 45mA current solar cell with WST load

As before, considering a 45mA current for each solar cell, the WST node is turn-in at 130ms (as the last case) but the V_{OUT} output voltage reaches 3.3V after 75ms. The efficiency of the LTC3105 regulator is 69.76% because, the output average powers of cells solar and LTC3105 regulator are respectively 35.36mW and 24.67mW. This value is in agreements with fig 4.19.

Fig.5.25 SEHS waveforms@45mA solar cell current-WST node.

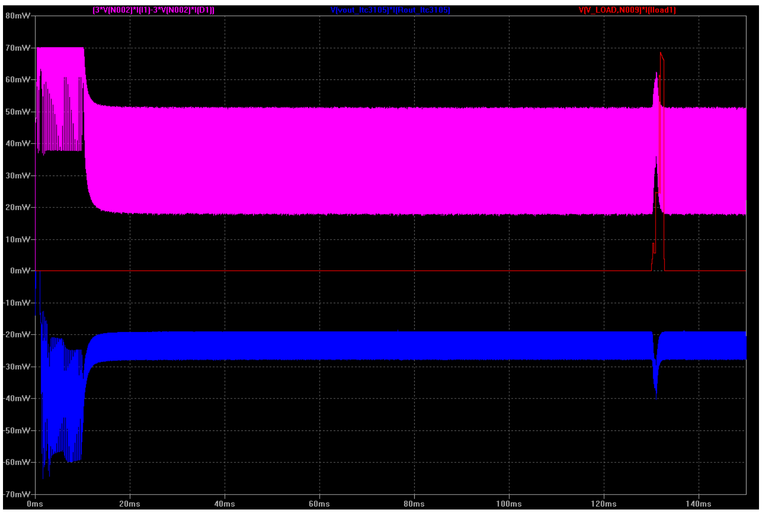

Fig.5.26 SEHS: solar cells output power (fuchsia waveform), LTC3105 output power (blue waveform) and load power consumption (red waveform) @45mA solar cell current-WST node.

Changing the wireless node, for the same reasons previously discussed, a comparison table is reported for all case examined.

	Sky Condition	Current Solar Cell [mA]	η [%] LTC3105	Start Turn-On [ms]
WST node	light overcast	15	78,33	130
	Clear	45	69,76	130
WSG node	light overcast	15	79	130
	Clear	45	70,05	130

Tab. 5.4 LTC3105 efficiency varying the wireless nodes and sky condition.

Comparing tables 5.3 and 5.4, in these conditions, the contribution from the RFEHS than SEHS, in term of "turn-on sensor" is lower. The situation could be reversed in the evening hours.

5.5 Prototype Implementation

In order to verify the performances of RF-Solar Energy Harvesting architecture, a PCB with dimensions 95mm x 60mm was created. In particular, in figure 5.27 it is possible to see the layout with all the components previously designed. This PCB layout has two metallization layers on both sides of substrate (ASTRA, eps=2.9, h=0.5 mm). The brown one is relative to top side, while the yellow one is the bottom side. The two sides are electrically linked through vias holes .

The proposed RF-Solar energy harvesting system was evaluated initially as individual subsystems and then as an hybrid energy harvesting system. In fact, through pins, it is possible to enable or disable manually the rectenna or the solar cells. The physical implementation of the hybrid energy harvesting circuit is shown in figure 5.28.

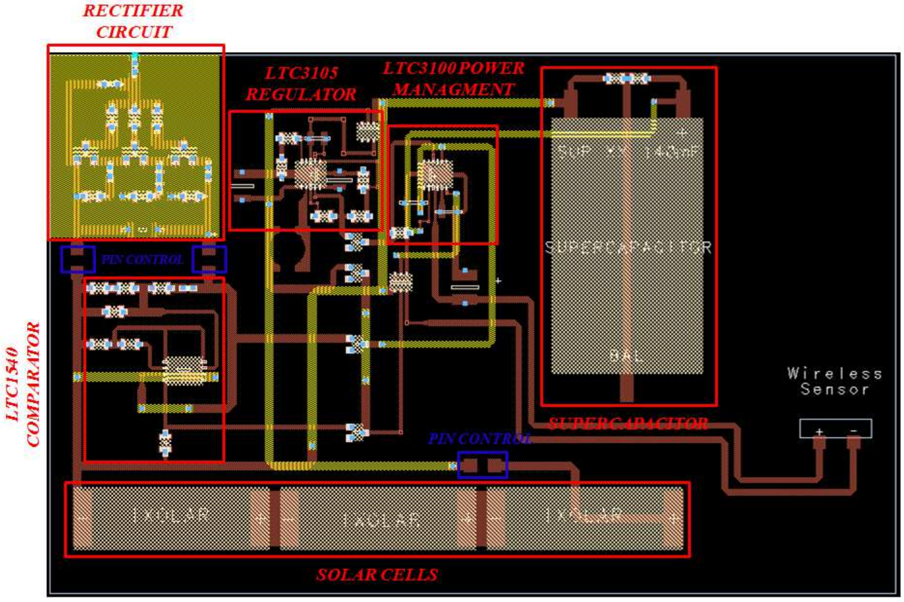

Fig.5.27 RF-Solar energy harvester layout.

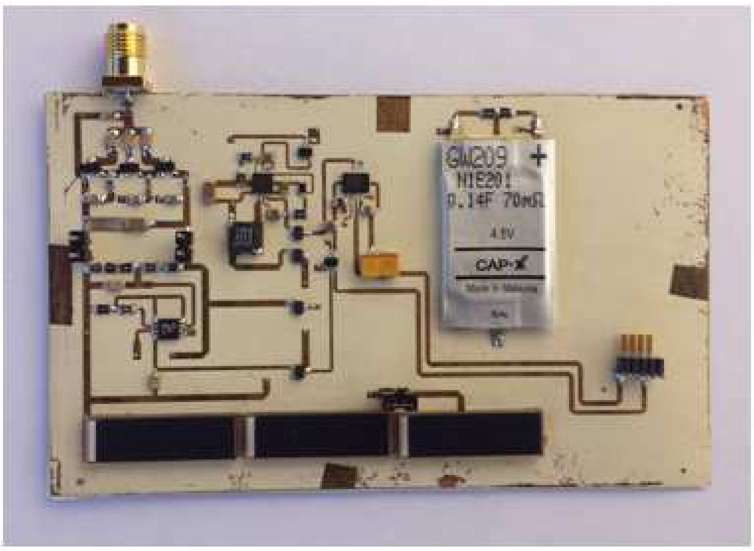

Fig.5.28a RF-Solar energy harvester prototype.

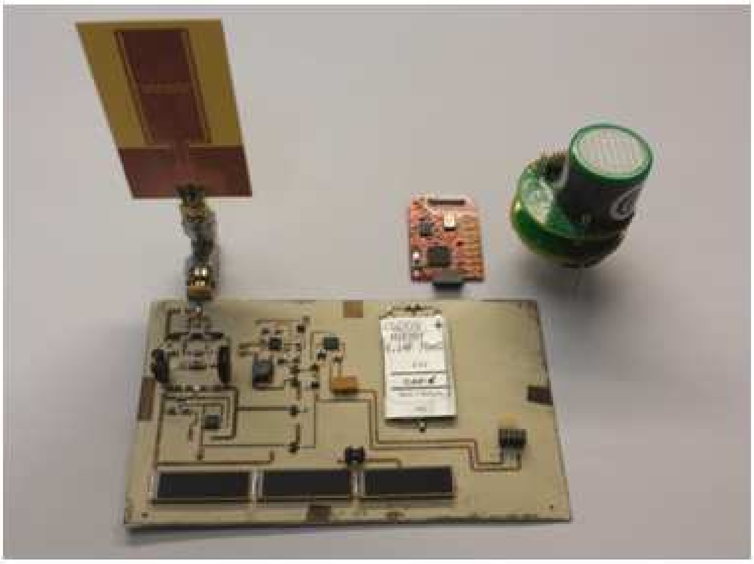

Fig.5.28b RF-Solar energy harvester prototype with MTM antenna and ULP sensors.

5.5.1 RFEHS subsystem performance

In order to verify the theoretical prediction and test the RF /DC rectification efficiency of the RFEHS, the measurement instrumentation for experimentation is set up as shown in figure 5.29.

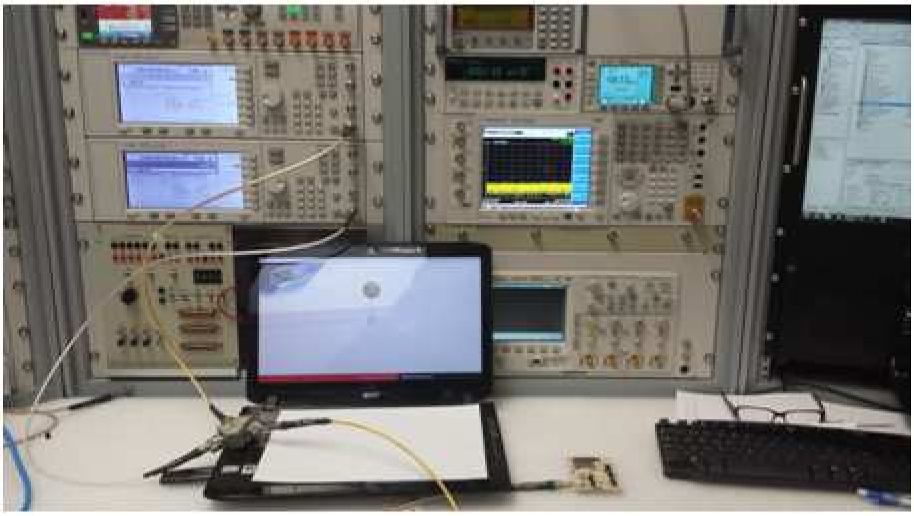

Fig.5.29 Set-up instrument for the RFEHS.

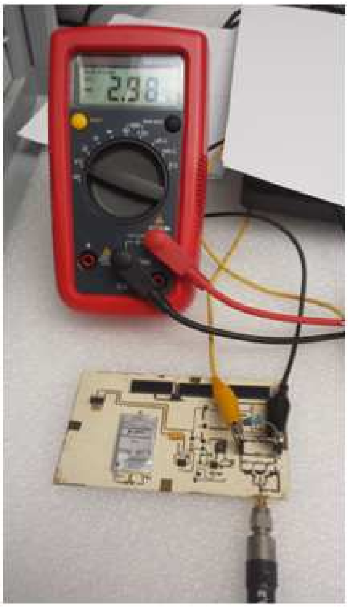

Fig.5.30 Output voltage measured of the rectifier circuit.

As it is possible to note in figure 5.30, in order to obtain the performances of the rectification circuit, it was necessary:

- to disconnect the antenna from the prototype and to connect directly to the input a cable for RF signal;

- to disable the control pin of the solar cells;

- to disable the control pin between rectenna and comparator

- to insert, as load for the rectification circuit, a 24KΩ resistance (load value considered in the rectifier circuit design).

To generate the sinusoid with a given power, a Waveform Generator (E442PC) 250kHz-64GHz of Agilent Technologies was used. Considering cable losses, the cable was linked to the circuit and a power sweep from -20dBm to 20 dBm was done. The utilized sensor node was initially a WST and then a WSG. In figure 5.30 it is possible to observe the rectification efficiency of wide band rectifier circuit in the three cases examined in the simulations.

The efficiency curve shows a steep increase at the beginnig, then a leveling and finally a slight decrease. The increase is a result of the exponential V-I-curve of the diodes, whereas the decrease for high power levels is caused by two factors: the first is the RF voltage approach to the reverse breakdown voltage during the high impedance state of the diode. The second factor is the diode current as it approaches the saturation current of the diode during the low impedance state.

In the three examined cases, maximum rectification efficiencies obtained were:

- GSM1800: η=60%@P_{RF_IN}=3dBm
- UMTS: η=50%@P_{RF_IN}=0dBm
- Wi-Fi: η=40%@ P_{RF_IN}=-4dBm

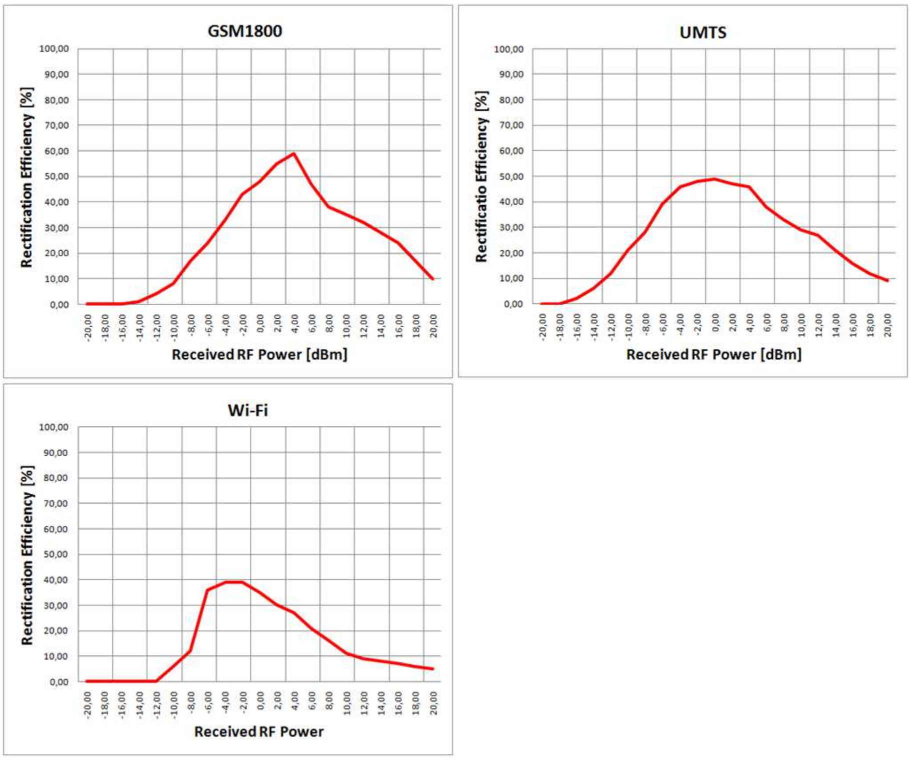

Fig.5.31 Rectification efficiencies measured for the GSM1800, UMTS and Wi-Fi cases.

Comparing figure 5.31 and 3.39, it is possible to note that the trend is identical, but with the same input RF power, the measurements diverge from the simulations of 5%. Anyway, considering that a matching network was designed with SMT component, the results obtained are quite acceptable.

Now we consider cases where the input signal is the sum of the input signals previously analyzed. For this reason, it was necessary to utilize a microwave coupler which is composed by two RF input ports and one RF output port (figure 5.29).

In order to compensate the RF cables and microwave coupler losses, the output of the microwave coupler was connected to the signal analyzer while the two input were connected to waveform generator (E442PC). In this way, it was possible to know exactly the total output power of the microwave coupler.

In figure 5.32 it is possible to note the coupler total output power is composed of two RF signals at 1800MHz and 2045MHz. The input RF power was equally divided for both signals.

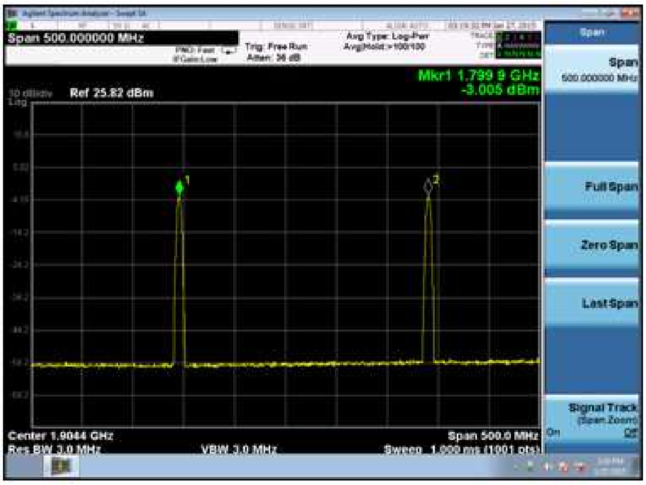

Fig.5.32 Sum of GSM1800 and UMTS signals in the Signal Analyzer.

In figure 5.33 it is possible to examine the rectification efficiency trends in the different cases.

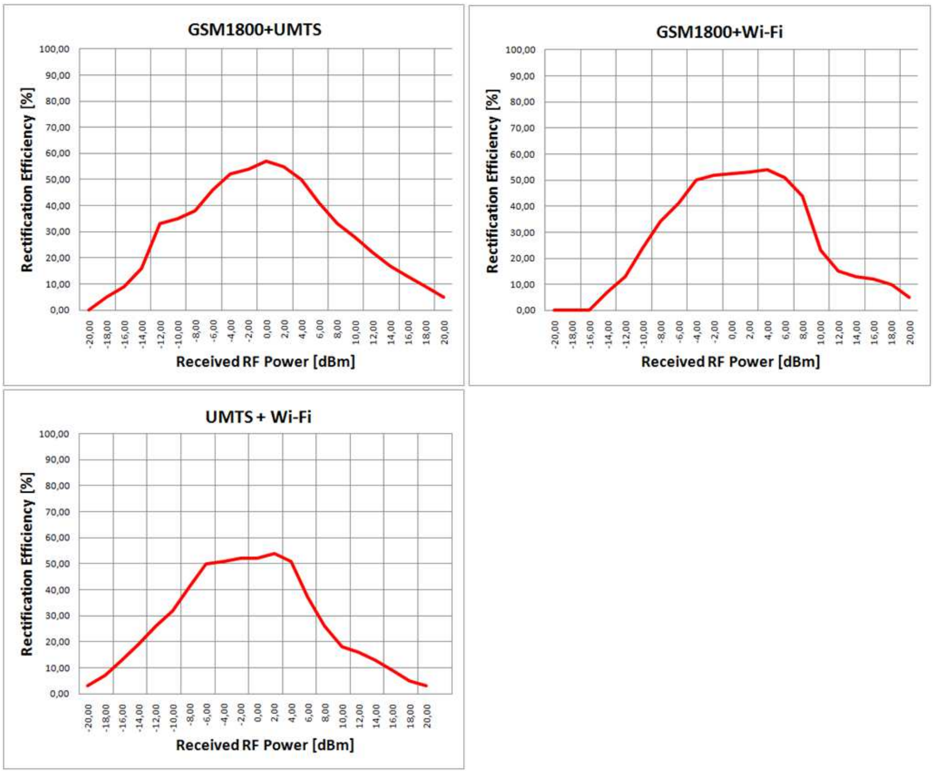

Fig.5.33 Rectification efficiencies measured for the GSM1800+UMTS, GSM1800 + Wi-Fi e UMTS + Wi-Fi cases.

Also in this case, comparing figure 5.33 with figure 3.4, we note that maximum rectification efficiency is worse of 8%.

After the calculation of the rectifier circuit performances, the control pins between comparator and rectifier circuit have been enabled and the 24kΩ resistance has been removed. In figure 5.34 and 5.35 the cases where RFEHS supply WST and WSG are shown.

Considering the temperature sensor, it turns on after 13 seconds measuring a room temperature of 25.1 °C, while in the same condition, the gas (CO) detector turns on after 12 seconds measuring a CO concentration of 13.5ppm (typical value in the air). The measure, sent via Bluetooth communication, is displayed through an app installed on a smartphone.

The activation times of the two sensors, compared with the ones obtained in simulations, are slightly superior because of the worse efficiency in the rectifier circuit.

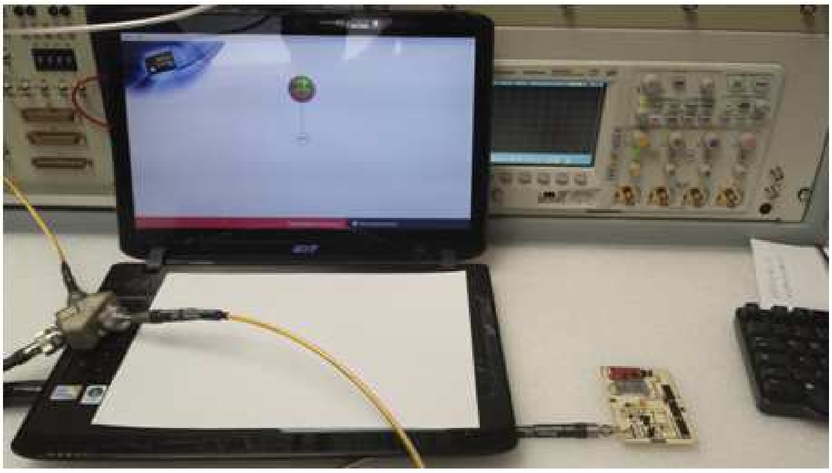

Fig.5.34 RF-Solar energy harvester prototype with WST load.

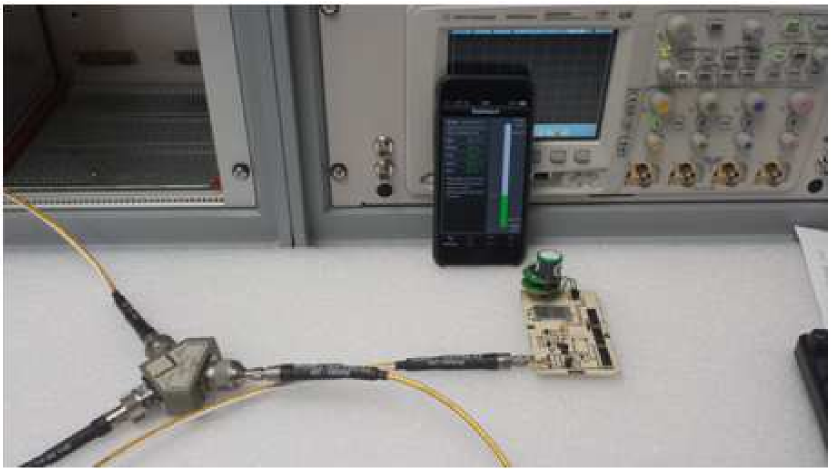

Fig.5.35 RF-Solar energy harvester prototype with WSG load.

Now we link the antenna to the RFEHS prototype and place it close to a Wi-Fi router, where radiating power is 1W and antenna gain is 3dBi (figure 5.32). Considering the “MTM-inspired” antenna with 2.3 dBi gain, the maximum distance in order to turn on the WST or WSG, is 80cm. At this distance, sensor turns on after 15 seconds. Also in this case, the activation time is superior to the one obtained in simulation (13 seconds) for the worse efficiency in the rectifier circuit at 2.45 GHz.

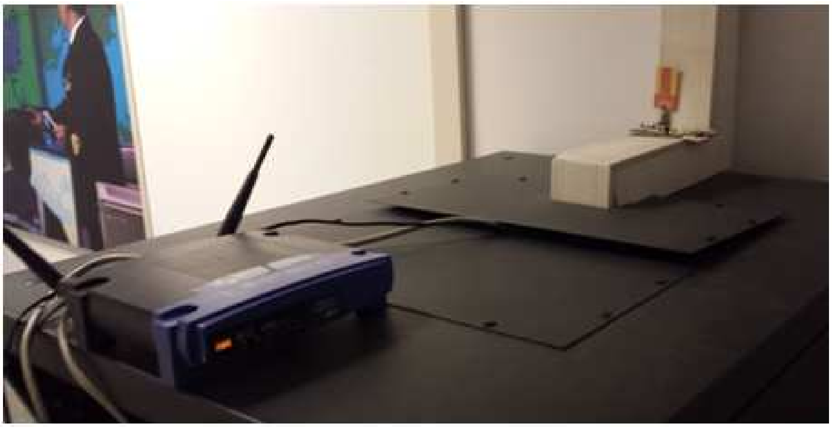

Fig.5.36 Wi-Fi energy harvester prototype with WST load.

5.5.2 SEHS subsystem performance

The SEHS characterization was obtained in outdoor environment, with clear sky (no clouds). Also in this case, WST and WSG were employed as a load for the SEHS prototype. In particular, in figure 5.37 we can see the SEHS prototype feeding the WST with a illuminance of 230.000 lux.

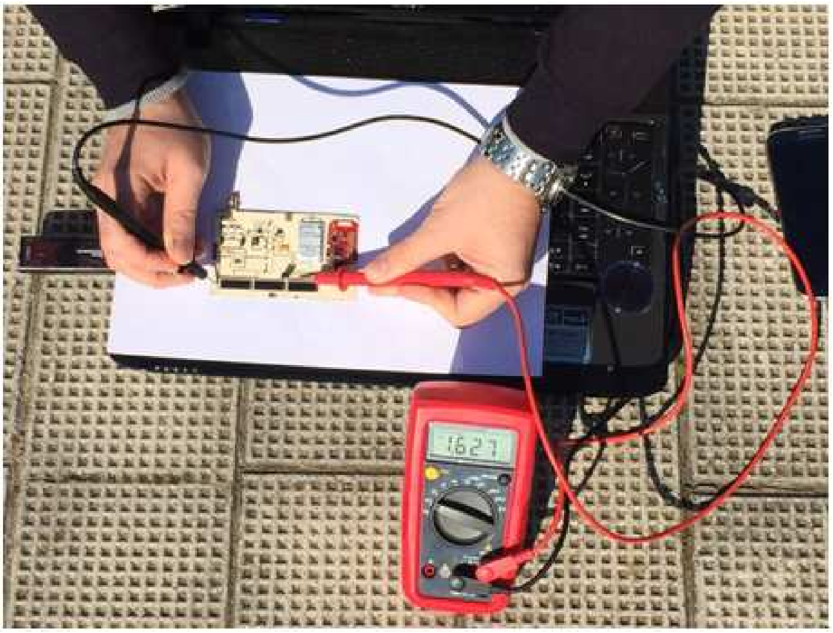

Fig.5.37 Solar energy harvester prototype with WST load in outdoor environment .

In such conditions, output voltages coming from the series of the three cells is 1.627 V. The sensor is immediately turned on (exactly as simulations), measuring an outdoor temperature of 17.7 °C. The C_{STORE} capacitor (140mF) reaches the maximum voltage 5.5V after 4 minutes.

Once loaded the back-up capacitor, the prototype was taken to a room where the solar cells were covered. Every second, the sensor measured the temperature of the room. The WST is powered by the energy stored by C_{STORE} capacitor for a time of 2 hours and 35 minutes.

In fact, the V_{STORE} voltage measured is lower than the V_{LAOD} voltage and then, the C_{STORE} ends to supply the load. For C_{STORE} values larger, the standby time of the sensor is extended.

The same measures are also carried out considering the WSG load. In particular, since such a sensor has a lower power consumption compared to the WST, the autonomy time was 4 hours and 15 minutes.

Both cases show how the TLC3108 regulator, manage efficiently the power harvested.

5.5.3 Hybrid system performance

In order to evaluate the performance of the hybrid system, all control pins present on the prototype, have been enabled. This system has been tested both outdoor and indoor environment. Also in this case, WST and WSG were employed as a load for the hybrid system prototype.

As we expected, thanks to the back-flow diodes (see Figure 5.22), the two harvesting circuits are completely independent each other. For this reason, and especially also considered the different amount of recoverable energy, measurements and tests performed on the entire hybrid system are completely identical to those carried out on the two energy harvesting sub-system. In particular, it was observed that when there are both sources (sun and GSM1800 / UMTS / Wi-Fi signals), the contribution of SEHS is much greater than the RFEHS.

Appendix A

Antenna Miniaturization Using Artificial magnetic Conductor Surfaces

Artificial Magnetic Conductor surfaces (AMC) are periodic structures that can be used to give a refection response similar to a PMC (Perfect Magnetic Conductor). This characteristic is limited to a range of frequencies and the AMC surface works like a regular metallic ground plane outside of its bandwidth. As shown in Figure A1, a conventional metallic ground plane reflects the electromagnetic waves with 180° phase shift (Γ=-1). On the other hand, the AMC surface can reflect the wave with zero degree phase shift (Γ=1) at a particular band that can be controlled with its unit cell (i.e. the smallest building block of the periodic structure) parameters. If positioned below a patch antenna, the AMC surface changes the image current decreasing the mutual impedance of the antenna and its image. For this reason, reactive impedance surface (RIS) is a common way that is often used for this structure [87].Because of this property, the RIS can provide an increased bandwidth performance. In addition, the interaction between the antenna and the RIS has been shown to result in antenna miniaturization and increased front to back radiation ratio [87-89].

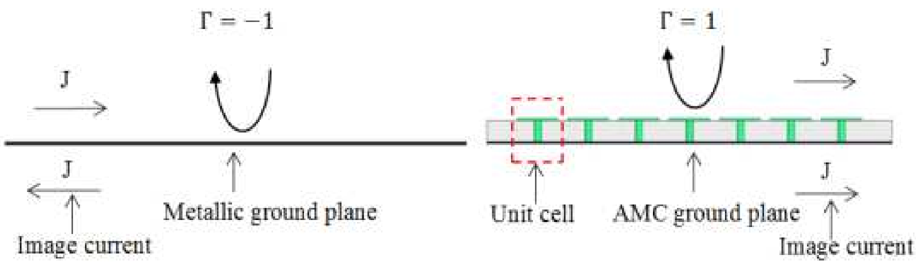

Fig. A1: Conventional metallic vs. AMC ground plane

The bandwidth of the AMC, in general, is defined as the frequency range where the phase of the reflection coefficient changes from -90° and 90°. The

AMC surface gives a phase reflection coefficient of zero at the center frequency. The center band frequency and bandwidth can be designed through the geometrical parameters of the AMC unit cell. o improve the bandwidth characteristics of the AMC cells many different geometries have been tested in recent literature [90-93].

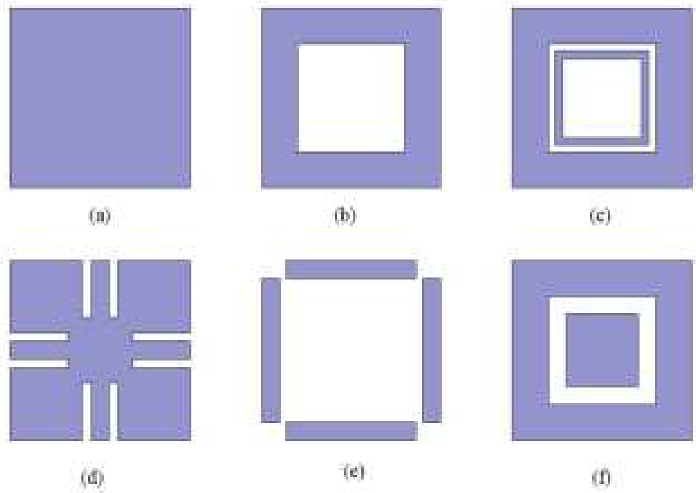

Fig. A2: Example of different metallization patterns employed in AMC unit cell design

Our purpose is to find ways of decreasing geometrical dimensions of wide-band microstrip antenna using AMC surfaces. In particular, starting from a polygonal antenna with a UMTS and Wi-Fi working band, the aim is to dimension the AMC cells (inserted inside the substrate) in order to work the antenna at lower frequencies (GSM1800) maintaining the bandwidth of departure. In this way, not by changing the size of the antennas, the one with the AMC cells electrically is smaller.

A1 Polygonal Patch Antenna

Starting from the UMTS-Wi-Fi polygonal patch antenna [94] designed on a substrate with a h= 9mm and εr= 3.9, the final dimensions are optimized in order to achieve a bandwidth equal to 900MHz (1700MHz-2800Mhz). The final dimensions are shown in Table A1. Considering a future translation of the working band towards the low frequencies, the increase of the bandwidth has been necessary to guarantee the antenna with the AMC cells to work at a frequency of 2.45 GHz (Wi-Fi).

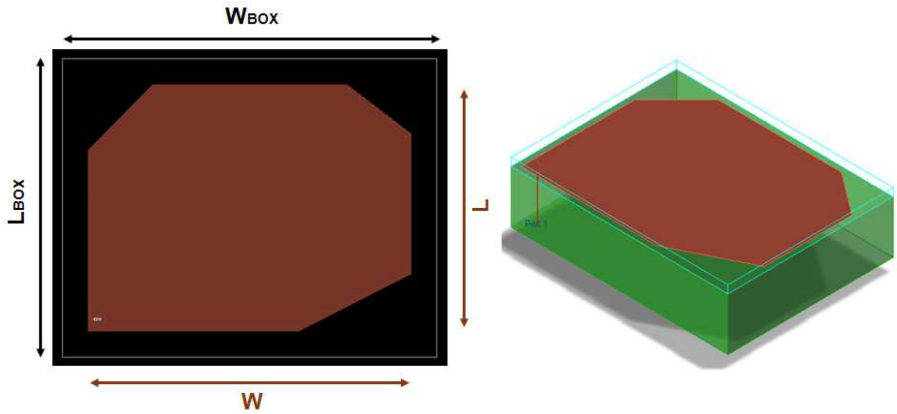

Fig. A3: UMTS-Wi-Fi Polygonal patch antenna.

The trend of the parameter S11 that defines the antenna working band (at -10 dB), and the one of gain, are shown in figure A4 and A5.

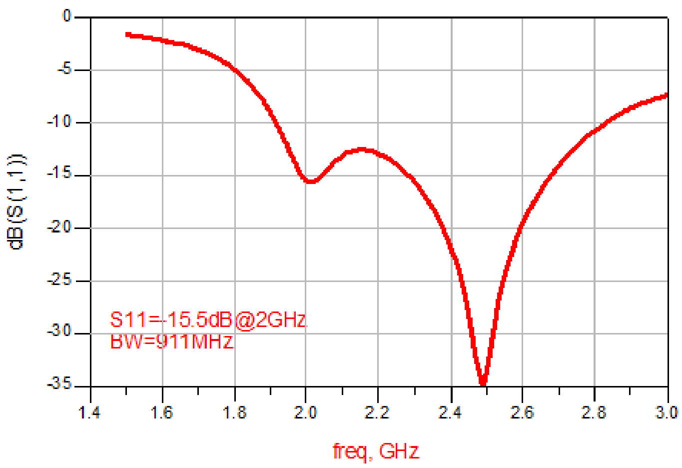

Fig. A4: Reflection coefficient magnitude of antenna (without AMC cells).

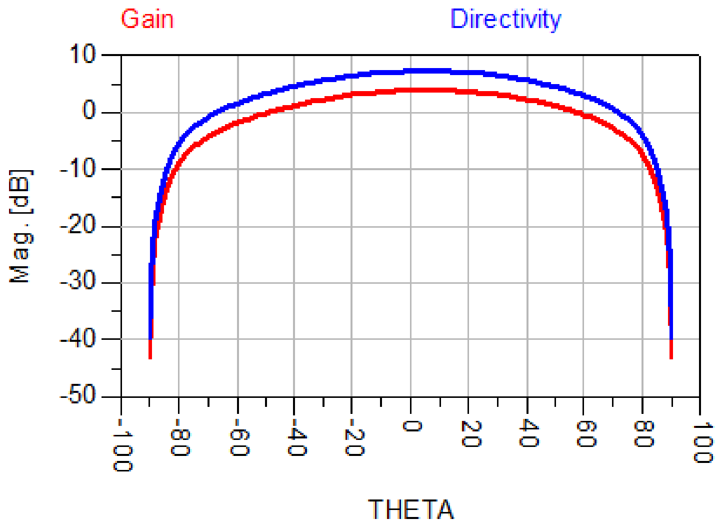

Fig. A4: Gain and directivity of antenna (without AMC cells).

A2 Polygonal Patch Antenna with AMC cells

The AMC unit cell considerate is composed by two dimensional periodic metallic patches printed on a grounded substrate. The periodicity of the metallic patches is much smaller than the wavelength. Considering a single cell illuminated with a TEM plane wave, PEC and PMC boundaries can be established around the cell as shown in figure A5. The resulting structure can be modeled as a parallel LC circuit where the edge coupling of the square patch provides a shunt capacitor and the short-circuited dielectric loaded transmission line can be modeled as a shunt inductor.

The impedance then can be obtained [95] as:

$$Z_{RIS} = \frac{X_L X_C}{X_L - X_C} \tag{A1}$$

$$X_L = jZ_d tan\, k_0 \sqrt{\varepsilon_r} h_2 \tag{A2}$$

$$X_C = \frac{1}{j\omega C_{RIS}} \tag{A3}$$

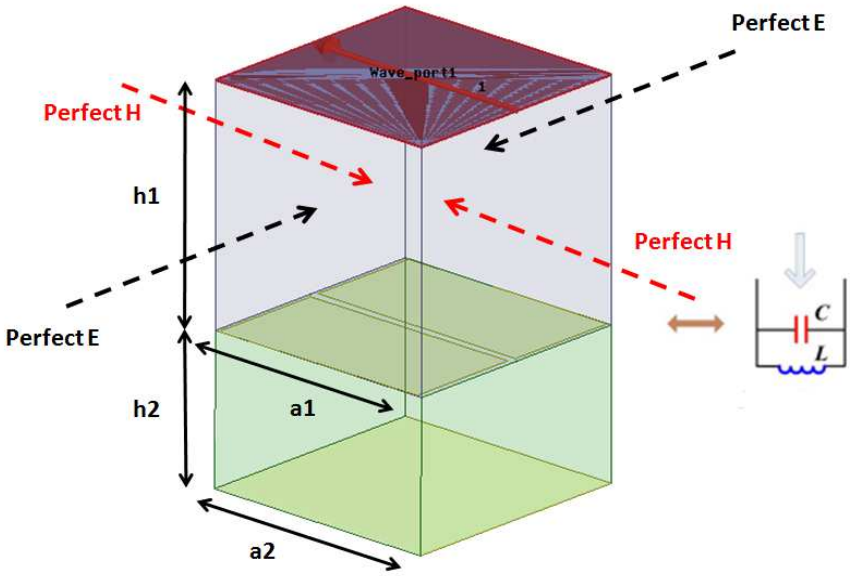

Fig. A5: HFSS model for reflection phase computation of the AMC cell.

The variation of the patch size and slot width mainly changes the capacitor value while the substrate thickness and dielectric constant mainly affects the inductance value, all of which can be used to control the resonance frequency. It is possible to achieve both an inductive RIS (under the RIS surface frequency) or a capacitive RIS (above the PMC surface frequency) with dependence of the operating frequency and the geometry [95].Note that since the near field generated by the patch antenna is not a uniform plane wave and the AMC is size-limited far from being periodic, the design of a radiating patch over the AMC using the unit-cell analysis shown. The last figure is just an approximation to qualitatively explain its working principle. An inductive RIS can store the magnetic energy which increases the inductance of the circuit. Then, this permits of miniaturizing the size of a patch type antenna which is essentially an RLC parallel resonator. In addition, the inductive RIS can give a wider matching bandwidth, then it is particularly fit for antenna application.[95]. Because of the capacitive coupling between the adjacent unit cell patches, enlarging the AMC patch produces the reduction of the zero phase reflection frequency.

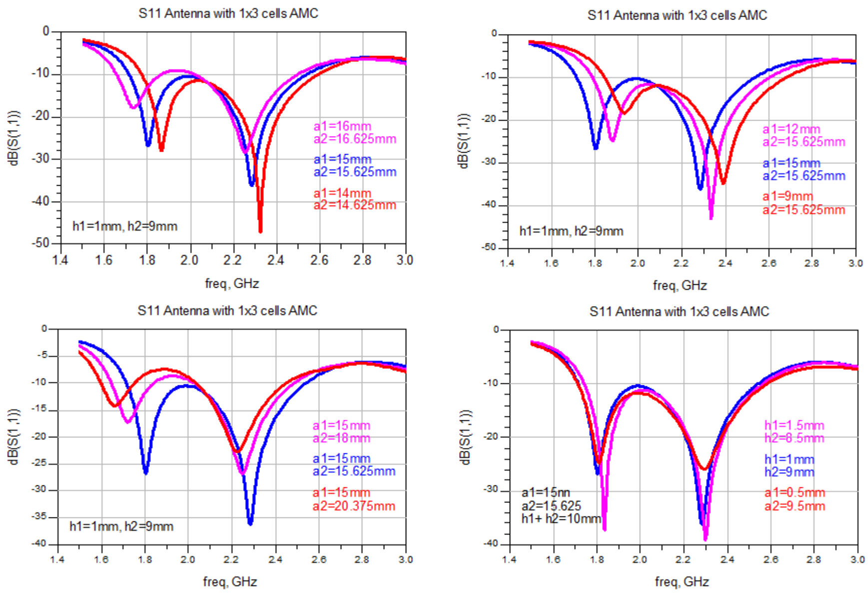

Fig. A6: A parameter study on the AMC for the proposed antenna.

Because the periodicity (a2) of the metallic patches must be much smaller than the wavelength, it was chosen initially a2= 15.625mm and a1=15mm. Once the height of the substrate (h1=0.5mm, h2=9.5mm) is set, it is noticed that keeping constant the gap between two adjacent patches (0.625mm), the resonance frequency of the antenna decreases with the increase of a1.

Furthermore, fixed the substrate and the periodicity (a2), decreasing the size of the patch (a1), the resonance frequency of the antenna increases.

Conversely, fixed the substrate and the size of the patch (a1), increasing the periodicity (a2), the resonance frequency of the antenna decreases but at the same time, increase the size of the antenna proposed.

Finally, fixed the total thickness substrate h (h1+h2=10mm) and the [a2, a1] parameters, increasing h1 (decreasing h2), the resonance frequency of the antenna increases (decreases).

Considering all this, the best AMC unit cell has the following features:

- a1=15mm
- a2=15.625mm
- h1=0.5mm
- h2=9.5mm

The resonance frequency of the single AMC unit cell is 2.4GHz and the AMC surface will absorb ~5% of the incident power due to the metallic and dielectric loss.

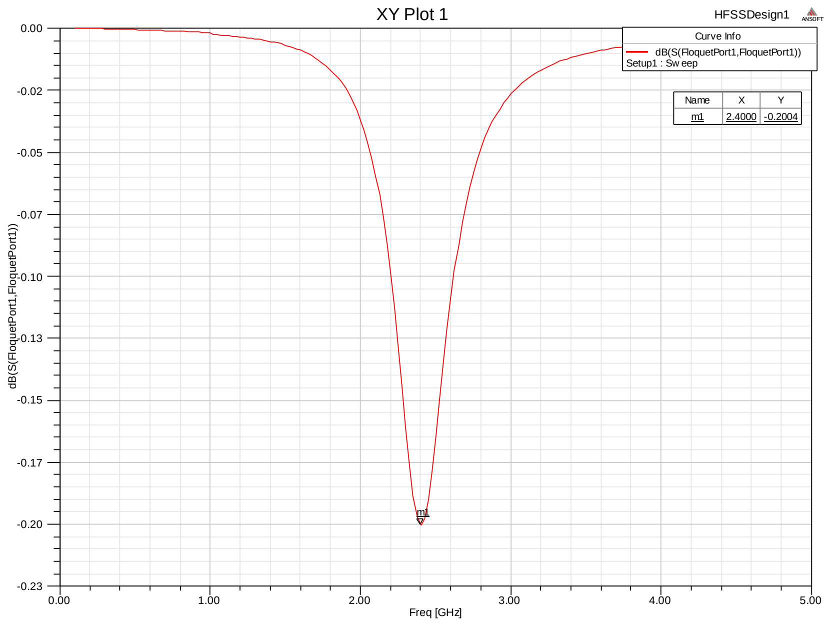

Fig. A7: Magnitude phase of the AMC surface.

The designed AMC exhibits a zero phase reflection with a bandwidth of 425 MHz for normally incident wave.

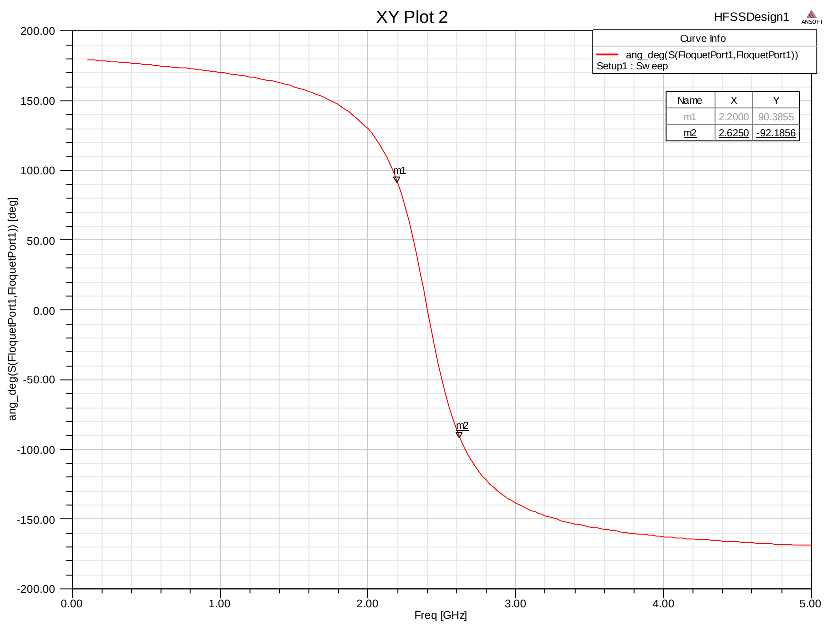

Fig. A8: Reflection phase of the AMC surface.

Defined the number and the AMC parameters, the polygonal microstip antenna with AMC cells (yellow color), is show in figure A9. The dimensions of the AMC cell and antenna, are reported in table A.1

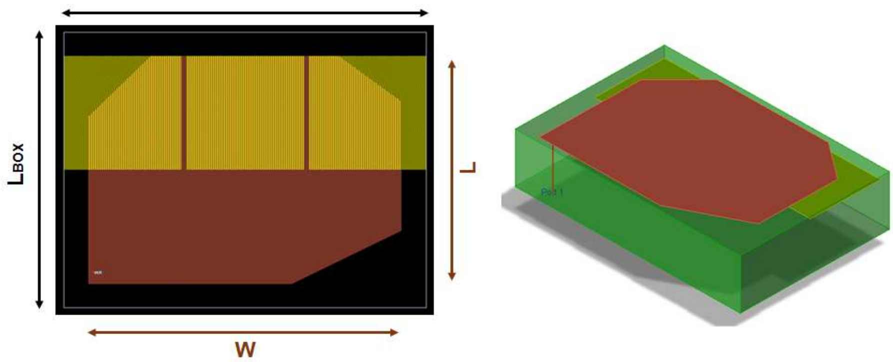

Fig. A9: GSM1800, UMTS-Wi-Fi Polygonal patch antenna with AMC.

Parameters	Antenna without AMC cell	Antenna with AMC cell
Fo [MHz]	2000	1810
εr	3.9	3.9
h1 [mm]	0.5	0.5
h2 [mm]	9.5	9.5
L [mm]	30	30
W [mm]	70	70
L_{BOX} [mm]	36.25	36.25
W_{BOX} [mm]	46.25	46.25
Area [mm^2]	1676.5	1676.5

Tab. A1: Comparison antenna parameter with and without AMC cells.

The reflection coefficient magnitude at the input port, reported in figure A10, shows a frequency band of operation (<-10dB) from 1700 to 2600 MHz, while the gain antenna is reported in figure A11.

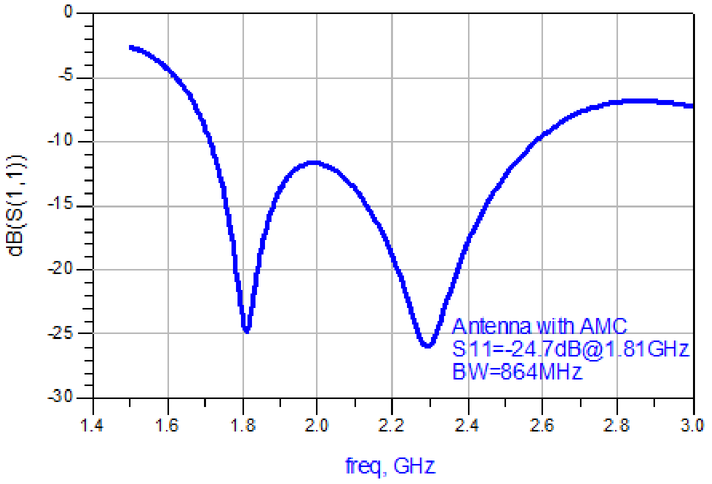

Fig. A10: Reflection coefficient magnitude of antenna (with AMC cells).

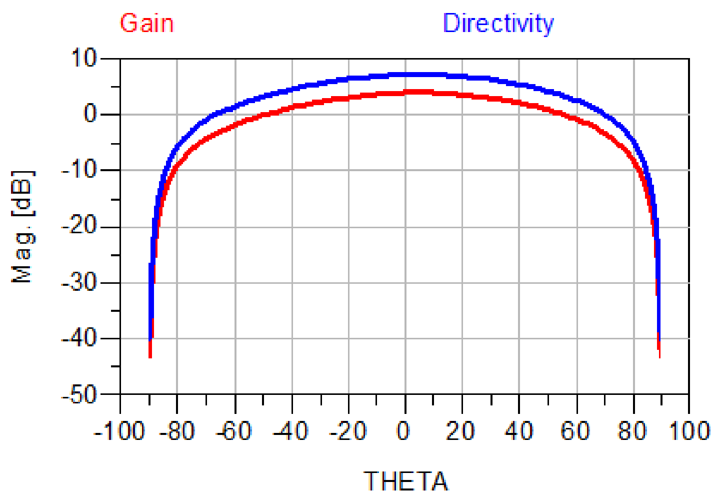

Fig. A11: Gain and directivity of antenna (with AMC cells).

Comparing the antennas with and without AMC cells (figure A3 and A9), the gain and the directivity are the same, while these present different S11 parameters. In particular, as shown in figure A12, the antennas have the same bandwidth but the antenna without AMC cells has a frequency band of operation (<-10dB) from 1900 to 2800 MHz, while the antenna with AMC cells from 1700 to 2600 MHz. This means that the inclusion of the AMC cell causes a move to lower frequencies of the working band, In particular, the translation is approximately 200MHz which ensures the antenna to work also in GSM1800 band. Finally, because the two antenna have the same dimensions, the antenna with AMC cells, is electrically smaller than antenna without AMC cell.

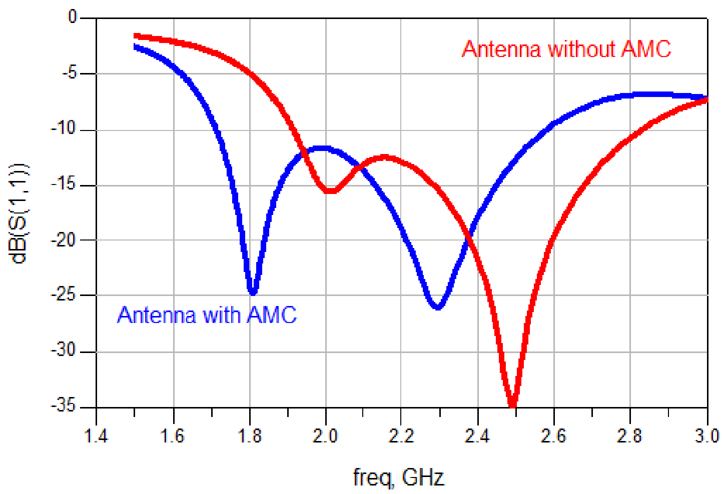

Fig. A12: Comparison between the reflection coefficient magnitude of antennas (with and without AMC cells).

Appendix B

An Energy Harvesting Application: Surveillance of Wide Zones with Unattended Ground Sensors

The growing interest for Unattended Ground Sensors (UGS) has stimulated the development of ultra low-power circuits that permit a bigger medium lifetime for the same systems. In fact, the main limit is the energetic one, given by the battery lifetime and by the energy required from the device. In order to ensure the efficiency of the device for long times, the solution is the employ of Energy Harvesting techniques, that recharge the battery also when the sensor is in an hostile environment where the device cannot be feed with traditional power sources.
In this appendix, we describe the experimental work and present an algorithm for vehicle and human detection using seismic and acoustic sensors. This algorithm aims to decrease the computational cost respect to the ones utilized in traditional techniques, so that the energetic need of the sensors could decrease, with the cost of an acceptable loss of efficiency.

B1 Introduction

Nowadays warfare scenarios always more often are complex city environments. Surveillance there is very difficult using traditional stand-off sensors. An approach with increasing popularity is the one of using a large amount of ground sensors distributed (or unattended) in the area of interest. These sensors have typically performances very limited both in terms of processing capability and battery life. Then, traditional approaches to recognition, identification, and tracking have to be reconsidered in this environment.
Previous work have been based on acoustic and seismic sensors because of their relatively low cost. Much of this work has been performed in relatively open spaces with specific military targets that have strong harmonic signatures. In urban areas, instead, the acoustic noise environment can be

quite dynamic, requiring a highly adaptive approach. In addition, typical targets may not be military vehicles, but civilian's passenger cars and trucks or simply people.

B2 Vehicle Detection Algorithm for the Acoustic Seismic Sensor

Previous works have shown that background noise for acoustic and seismic sensors is strongly non-stationary and non- Gaussian [96]. Under weather calm conditions the noise background is quite stable, but wind can produce dramatic and rapidly changing noise levels that are very hard to compensate for. Other common noise sources include animal sounds, construction equipment, thunder, rain, aircraft, etc.

Because we can have really large variations in noise background and target signatures, we need a really robust detection algorithm that can easily adapt to changing conditions. A procedure used often working with such a non-homogeneous environment is of employing an order statistic constant false alarm rate (OS-CFAR) detection algorithm. In an OS-CFAR algorithm, the samples in an assigned window size are taken by increasing magnitude. The k^{th} value is then employed as a test statistic. One virtue of this procedure is that it can be quite easily implemented through a *median filter*. In the definitive implementation we made many uses of order statistics to obtain both the noise power and the change in the noise power over time. This resulted in a very robust and flexible algorithm that could be easily reutilized in different domains. The data was collected using a SM-7 10 Hz Geophone and a SMM310 Microphone with a minimum sample rate of 64 samples/sec. We collect data in continuous blocks. We then evaluate the median of the absolute value of each block. The median filter provides further robustness against non-Gaussian data as well as being computationally efficient [97]. The median of each snippet is then used in a secondary running median filter. This permits us of estimating the noise. Since each block is reduced to only a single value, the running median filter can be relatively long (corresponding to a significant duration in time) without using an excessive amount of memory. This allows us to adjust the algorithm to be more or less responsive to changes in background noise level according as our operational needs. An additional filter (with running median) is also employed on the variance between the current block median and the regime noise estimate. This gives us an approximate measure of the mean and standard deviation of background distribution (although we are using order statistics rather than sample averages). We can then use these estimated values as a basis for a CFAR detector. Estimation of the mean and standard deviation allows the use of a CFAR detector. We choose between the two hypothesis H_0 = no target present and H_1 = target present using

$$m_n - b \quad \underset{H_0}{\overset{H_1}{\gtrless}} \quad T\sigma \tag{B1}$$

where m_n is the median of the absolute value of the n^th block, b is the current background estimate, T is a user defined threshold value (typically 3.0), and finally, σ is the median deviation of the background. To reduce false alarms we require 3 blocks to surpass the threshold before having a detection event. Moreover, the algorithm is robust against the unexpected "spike" false alarm.

B3 Human Detection Algorithm for the Seismic-Acoustic Sensor

We considered the problem of personnel detection using a single geophone and microphone used above. Here we discuss a method to tell footsteps apart from and other seismic and acoustic signals using the single component sensor. A footstep signature is caused by the impact on the ground. Each footstep has a characteristic shape that can be used to distinguish it from other noise. The main feature of the footstep when comparing time series data for footsteps to other seismic signatures is the series of sharp "spikes" generated by each impact. This differs from the random noise induced by the winds over the ground and from vehicle noise. The problem is how to quantitatively distinguish the shape of a footstep signature from other seismic or acoustic signatures. We make this distinction through a statistical measure of the amplitude of the signature, the kurtosis. Kurtosis is ratio of the 4th to 2nd moment of the amplitude distribution of the signature. For each snippet, composed from N samples of data, the kurtosis is calculated:

$$m_n - b \quad \underset{H_0}{\overset{H_1}{\gtrless}} \quad T\sigma \tag{B2}$$

where μ is the mean, computed over N samples. The kurtosis value compared for a sample sequence is much higher in the presence of impulsive events than it is in the presence of Gaussian or sinusoidal signatures [98]. Note that the method depends only on the shape of the signature and not the amplitude. The magnitude of kurtosis tends to be higher for the raw signature, and we will use it herein. In the [98], kurtosis value measured is between 13 and 6 varying the distance between the personnel and sensor. Kurtosis values computed for sinusoids are less than 2 and for Gaussian noise are approximately 3 [98]. When the vehicle is near to the sensor, the vehicle signature dominates, and the kurtosis is ~3, while as the vehicle moves away the kurtosis increases [98]. The kurtosis itself varies with target, time and distance and its value for vehicles and background noise the kurtosis is low. From the kurtosis distribution we can construct ROC (Receiver Operating Characteristic) curves [99]. These curves are normally constructed assuming Gaussian distribution of signal amplitude. It is also possible to consider the non Gaussian distribution of the kurtosis. The "noise" distribution can be obtained from the measure of ambient noise, or from that of the vehicle signature. The "signal" distribution can be that of any combination of walker and jogger. For each kurtosis level, the probability of false alarm is the integral under the tail of the "noise" distribution. The probability of right detection is the corresponding (much larger) integral under the signal distribution. In [98], the process is illustrated.

B4 Experimental Results

This section will demonstrate the algorithm presented in previous sections. The field test was a one day test near Selex-ES in Giugliano (NA) during the daytime hours. In that day, the weather was clear and the temperature was 32°C with low wind. The field test consisted of vehicle and personnel pass-bys closed (two meters) at two sensors on the paved road. The seismic and acoustic signals acquired with 44.100 sample/sec are showed respectively in figure B2a and in figure B4a. After, these signals have been sampled with a sampling frequency of 64 Hz because this value is a good compromise between accuracy (low false alarm) and power consumed (due at processing of data acquired). The data have been collected in continuous snippets, each of duration of half second and analyzed 5 snippets at time. In this situation, the threshold will update every 5 snippets that is every 2.5 second. In the vehicle detection, in order to reduce false alarms, we further require 3 snippets to exceed the detection threshold before declaring a detection event. Instead, in the human detection, the Kurtosis threshold value, in order to declare the detection has been fixed at 6.5 [98]. The block diagram of the algorithm for the vehicle-human detection is showed in figure B1.

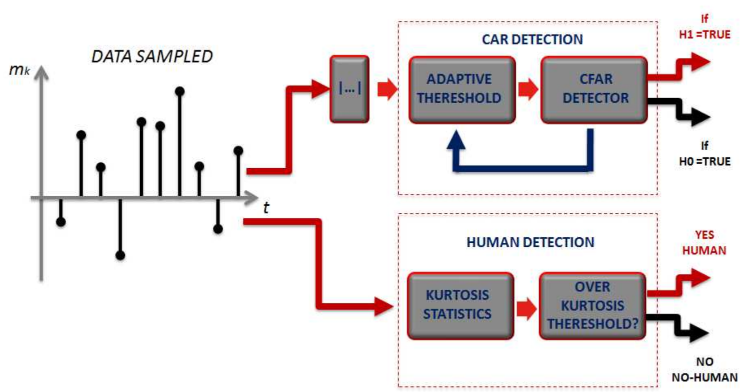

Fig. B1: Block diagram of the algorithm for the vehicle-human detection.

An example of the detection process, with geophone sensor, is show in figure B2 and figure B3. In particular, in figure B3a shows the estimated background noise level and the noise threshold for vehicle detection while in figure B3b the relative kurtosis function varying the number of samples for second. The final detection result is shown in figure B2b where the red lines represent the human detection while the black linen that for the vehicle.

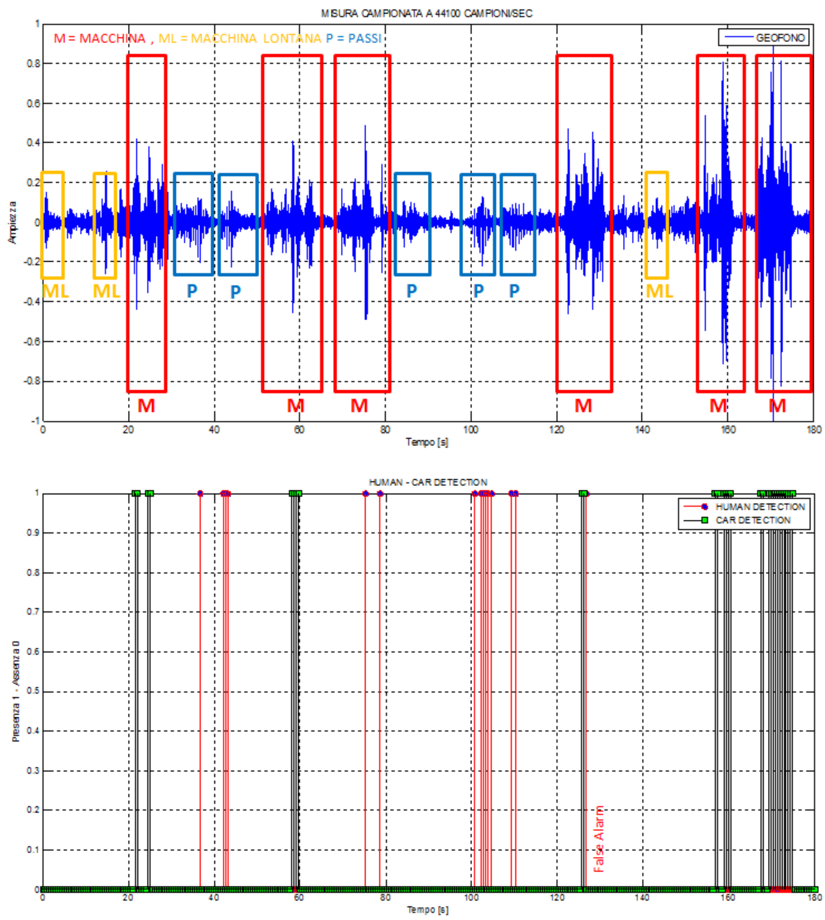

Fig. B2: (a) Geophone signal during the transit of the vehicle and the personnel and (b) the relative detection by the algorithm presented.

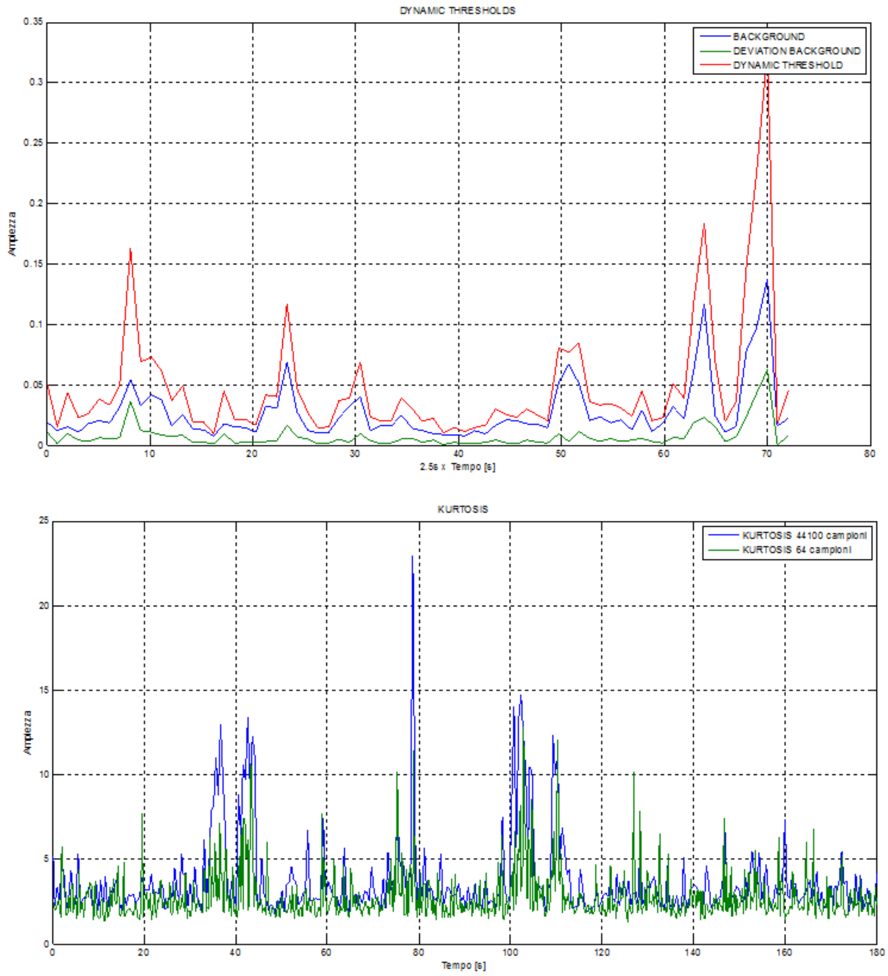

Fig. B3: (a) Background estimate and dynamic threshold for the vehicle detection and (b) the trend of the Kurtosis chancing the sample rate for the human detection considering a seismic signal.

As before, an example of the detection process, with microphone sensor, is show in figure B4 and B5. In particular, in figure B5a shows the estimated background noise level and the noise threshold for vehicle detection while in figure B5b the relative kurtosis function varying the number of samples at second. The final detection result is shown in figure B4b where the red lines represent the human detection while the black linen that for the vehicle.

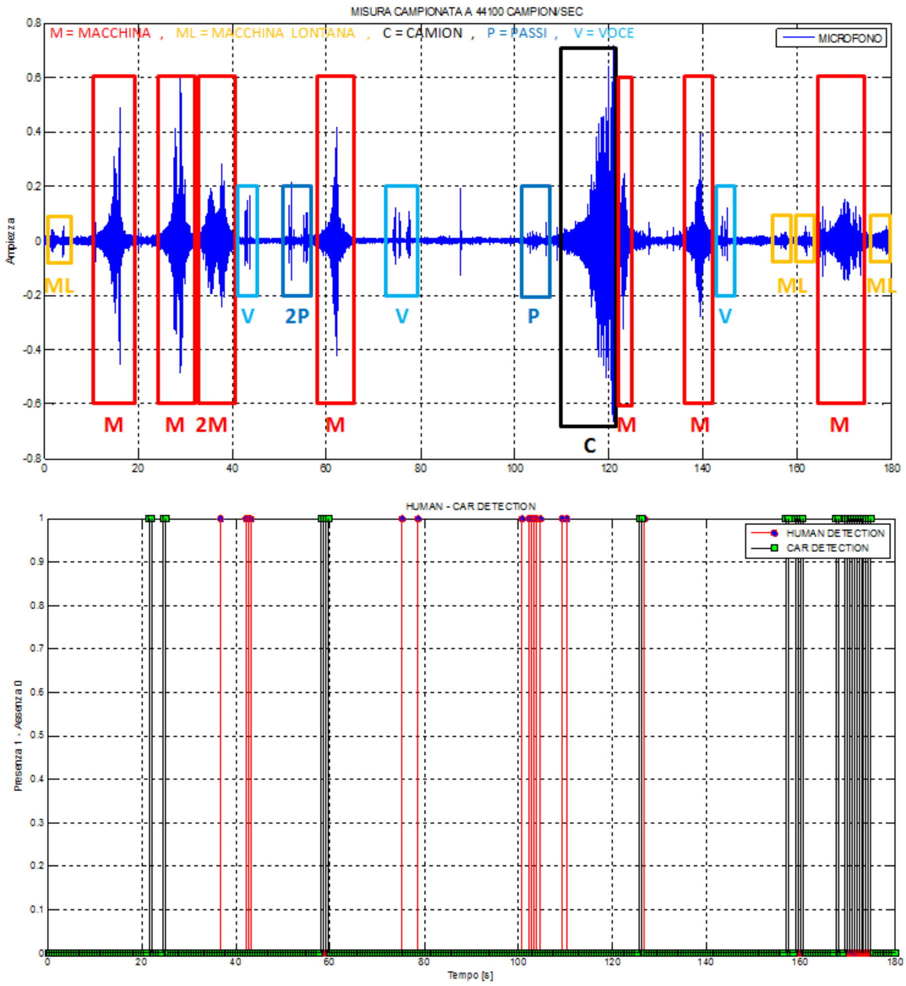

Fig. B4: (a) Microphone signal during the transit of the vehicle and the personnel and (b) the relative detection by the algorithm presented.

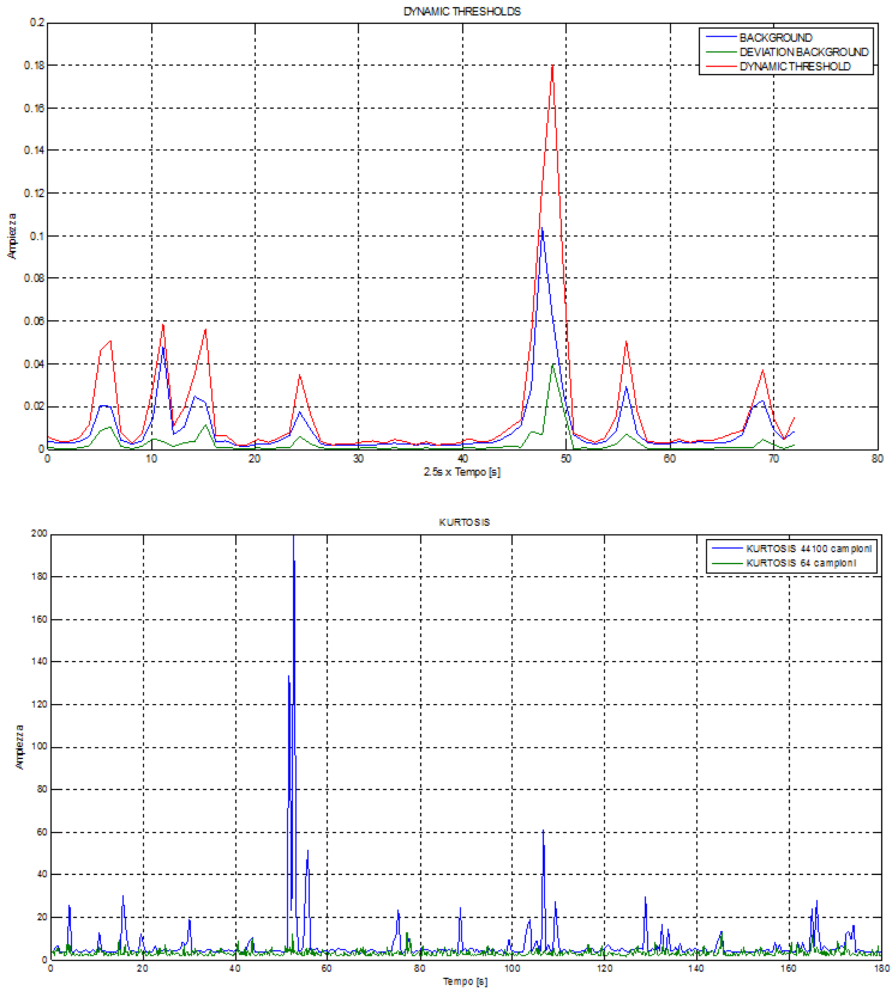

Fig. B5: (a) Background estimate and dynamic threshold for the vehicle detection and (b) the trend of the Kurtosis chancing the sample rate for the human detection considering an acoustic signal.

The results demonstrate that, although a few sample for second, the algorithm present only two false alarm (at 130 second utilizing the geophone and at 170 second for the microphone). Fewer than 64 sample for second the algorithm manifest numerous false errors while, increasing the number of the samples, the performance improves at the expense of the higher power consumption.

6
Conclusions

This thesis has presented energy harvesting techniques for energy-autonomous wireless sensor network nodes or ultra low power devices.

In particular, a hybrid energy harvesting system is developed to harvest simultaneously electric power from solar and radio frequency signals (GSM1800, UMTS, Wi-Fi), allowing self-sustained operation.

For the Solar Energy Harvester and the RF Energy Harvester, the energy conversion devices were respectively a small solar cell and a flexible wideband metamaterial inspired antenna.

In the first harvester, in order to improve the performance, maximum power point control has been evaluated and applied.

In the second harvester, high efficiency RF/DC using a new wideband rectifier topology has been found.

Potential types of energy reservoirs for the wireless sensors such as supercapacitors was investigated. The power management circuit responsible to manage the energy recovered and the charge of supercapacitor has been implemented. This supercapacitor, once loaded from power management, has the aim to supply the wireless senor node when the energy sources references are not present. This capacitor is loaded when there is a surplus input energy.

The hybrid prototype design was capable to recover enough energy from the two harvesters in order to sustain the wireless sensor nodes at a minimum operating duty-cycle of 1%.

References

[1] http://www.ti.com/tool/gassensorvm, 2015.

[2] http://www.ti.com/tool/ez430-rf2500, 2015.

[3] S. Roundy, BP. Otis, Y. Chee, J.M. Rabaey, *Power sources for wireless sensor networks*, in Proceedings of the 1st European Workshop on Wireless Sensor Networks(EWSN), Berlin, Germany, 2004.

[4] N. Shenck, J. Paradiso, *Energy scavenging with shoe-mounted piezoelectrics*, IEEE Micro, 21(3):30–42, 2001

[5] V. Raghunathan, A. Kansal, J. Hsu, J.Friedman, M. Srivastava, *Design considerations for solar energy harvesting wireless embedded systems*, Proceedings of the 4th International Symposium on Information Processing in Sensor Networks 2005 (IPSN 2005),1:457–462, 2005.

[6] C. Alippi, C. Galperti, *An Adaptive System for Optimal Solar Energy Harvesting in Wireless Sensor Network Nodes*, Transactions on Circuits and Systems I: Regular Papers, Volume: 55 , Issue: 6 , Page(s): 1742 – 1750, 2008. IEEE.

[7] S. Bader, B. Oelmann, *Enabling Battery-Less Wireless Sensor Operation Using Solar Energy Harvesting at Locations with Limited Solar Radiation*, Fourth International Conference on Sensor Technologies and Applications (SENSORCOMM), Page(s): 602 – 608, 2010. IEEE.

[8] P. Lee, Zhi Ang Eu; Mingding Han, H. Tan, *Empirical modeling of a solar-powered energy harvesting wireless sensor node for time-slotted operation*, Wireless Communications and Networking Conference (WCNC), Page(s): 179 – 184, 2011. IEEE.

[9] S. Bader, B. Oelmann, *Short-term energy storage for wireless sensor networks using solar energy harvesting*, 10th IEEE International Conference on Networking, Sensing and Control (ICNSC), Page(s): 71 – 76, 2013. IEEE.

[10] A.A.A. Rahman, N.A. Rashid,A.S.A. Aziz, G. Witjaksono, *Design of autonomous micro-solar powered energy harvesting system for self-powered batteries-*

less wireless sensor mote, Electronics Goes Green 2012 (EGG), Publication Year: 2012 , Page(s): 1 – 4, 2012. IEEE.

[11] K.V. Naveen, S.S Manjunath, *A reliable ultra capacitor based solar energy harvesting system for Wireless Sensor network enabled intelligent buildings*, 2nd International Conference on Intelligent Agent and Multi-Agent Systems (IAMA), Page(s): 20 – 25, 2011. IEEE.

[12] S. Gopi Nambiar, P. Ranjan, *Energy harvesting system for deployment of Wireless Sensor Networks in Nuclear Fusion Reactor*, 2012 International Conference on Green Technologies (ICGT), Page(s): 288 – 292, 2012. IEEE.

[13] A. Liberale, E. Dallago, A.L. Barnabei, *Energy harvesting system for wireless body sensor nodes*, Biomedical Circuits and Systems Conference (BioCAS), Page(s): 416 – 419, 2014. IEEE.

[14] H. Nishimoto, Y.Kawahara, T Asami, *Prototype implementation of ambient RF energy harvesting wireless sensor networks*, Sensors, Page(s): 1282 – 1287, 2010. IEEE.

[15] L. Xiao, P. Wang, D. Niyato, D. Kim, Z. Han,. *Wireless Networks with RF Energy Harvesting: A Contemporary Survey*, Communications Surveys & Tutorials, Volume: PP , Issue: 99 , Page(s): 1, 2014. IEEE.

[16] A. Bharathidasan, V.A.S Ponduru, *Sensor networks: An overview*, IEEE Potentials, 22(2):20–23, 2003.

[17] I. F. Akyldiz, W. SU, Y. Sankarasubramaniam, E. Cayrci. *A Survey on Sensor Net-works*. IEEE Communications Magazine, 40:102–114, Aug. 2008.

[18] http://www.ti.com , 2015.

[19] A. Cuadras, M. Gasulla, A. Ghisla, V. Ferrari, *Energy harvesting from pzt pyroelectric cells*, Proceedings of the IEEE Instrumentation and Measurement Technology Conference (IMTC 2006), 1:1668–1672, 2006.

[20] K. Vijayaraghavan, R. Rajamani, *Active control based energy harvesting for batteryless wireless sensors*, Proceedings of the American Control Conference (ACC '07),1:3106–3111, 2007.

[21] R. Ang, Y. Tan, S. Panda, *Energy harvesting for autonomous wind sensor in remote area*, Proceedings of the 33rd Annual IEEE Industrial Electronics Society Conference (IECON '07), 1:2104–2109, 2007

[22] W. Wu, Y. Chen, Y. Chen, C. Wang, Y.Chen, *Smart wireless sensor network powered by random ambient vibrations*, Proceedings of the IEEE International Conference on Systems, Man and Cybernetics (SMC '06), 4:2701–2708, 2006.

[23] A. Kansal, J. Hsu, S. Zahedi, M.B. Srivastava, *Power management in energy harvesting sensor networks*, ACM Transactions on Embedded Computing Systems (TECS), 6(32):1–9, 2007.

[24] J. Jensen, B. Sørensen, *Fundamentals of energy storage*, Canada: John Wiley & Sons, Inc, 1984.

[25] http://www.cap-xx.com

[26] S. Flipsen, *Alternative power sources for portables & wearables*, Technical Report, Delft University of Technology, Netherlands, 2005.

[27] P.Z. Peebles, T.A. Giuma, *Principles of Electrical Engineering,* McGraw-Hill, 1991.

[28] S. Priya, D.J. Inman, "*Energy harvesting technologies*," New York: Springer, 2009.

[29] G. Yang, Z. Yukan, Q. Qinru, *Improving energy efficiency for energy harvesting embedded systems*, 18th Asia and South Pacific Design Automation Conference (ASP-DAC), Page(s): 497 – 502, 2013. IEEE.

[30] R.J.M. Vullers, R. van Schaijk, I. Doms, C. Van Hoof, R. Mertens, *Micropower energy harvesting*, Solid-State Electronics 53, 684–693, 2009.

[31] M. Renaud, et al., *Piezoelectric harvesters and MEMS technology: fabrication, modeling and measurements*, IEEE Solid–State Sensors, Actuators and Microsystems Conference, pp. 891–894, June 2007.

[32] M. Marzencki, S. Basrour, B. Charlot, S. Spirkovich, M. Colin, *A MEMS piezoelectric vibration energy harvesting device*, Power MEMS Conference, pp. 45-48, Nov. 2005.

[33] W. Wang, V. Leonov, P. Fiorini, C. Van Hoof, *Micromachined thermopiles for energy scavenging on human body*, IEEE Solid–State Sensors, Actuators and Microsystems Conference, pp. 911-914, June 2007.

[34] H. Ostaffe, *RF energy harvesting enables wireless sensor networks*, [Online]. Available: http://www.sensorsmag.com

[35] http://www.chiron-project.eu /, 2015.

[36] C. Park, P.H. Chou , *AmbiMax: Autonomous Energy Harvesting Platform for Multi-Supply Wireless Sensor Nodes*, Sensor and Ad Hoc Communications and Networks, 2006. IEEE

[37] J. Xiaofan, J. Polastre, D. E. Culler, *Perpetual environ- mentally powered sensor networks*, in Proceedings of the Fourth International Symposium on Information Processing in Sensor Networks, IPSN 2005 UCLA, Los Angeles, California, USA, April 25-27 2005, pp. 463–468, 2005

[38] F. Simjee, P. H. Chou, *Everlast: long-life, supercapacitor operated wireless sensor node*, in ISLPED '06: Proceedings of the 2006 international symposium on Low power electronics and design, New York, NY, USA, 2006, pp. 197–202, ACM Press, 2006.

[39] M. Veefkind, *Industrial design and pv-power, challenges and barrieres*, in proceedings of the ISES Solar World Congress , 2003.

[40] A. Decker, *Solar energy harvesting for autonomous field devices*, Wireless Sensor Systems, Volume: 4 ,Issue: 1, Page(s): 1 – 8, 2014. IET.

[41] J. Schmid, T. Gaedeke, T. Scheibe, W. Stork, *Improving Energy Efficiency for Small-Scale Solar Energy Harvesting*, Proceedings of 2012 European Conference on Smart Objects, Systems and Technologies (SmartSysTech), Page(s): 1 – 9, 2012. VDE.

[42] K. Kadirvel, Y. Ramadass, U. Lyles, J. Carpenter, V. Ivanov, V. McNeil, A. Chandrakasan, B. Lum-Shue-Chan, *A 330nA energy-harvesting charger with battery management for solar and thermoelectric energy harvesting*, International Solid-State Circuits Conference Digest of Technical Papers (ISSCC), Page(s): 106 – 108, 2012 IEEE.

[43] Q. Brogan, T. O'Connor, Dong Sam Ha, *Solar and thermal energy harvesting with a wearable jacket*, International Symposium on Circuits and Systems (ISCAS), Page(s): 1412 – 1415, 2014. IEEE.

[44] K. Gudan, S. Chemishkian, J.J. Hull, S.J. Thomas, J. Ensworth, M.S. Reynolds, *A 2.4GHz ambient RF energy harvesting system with −20dBm minimum input power and Ni-MH battery storage*, RFID Technology and

Applications Conference (RFID-TA), Page(s): 7 – 12, 2014. IEEE.

[45] H, Jabbar, Y.S. Song, T.T. Jeong, *RF energy harvesting system and circuits for charging of mobile devices*, Transactions on Consumer Electronics, Volume: 56, Issue: 1, Page(s): 247 – 253, 2010. IEEE.

[46] P. Nintanavongsa, U. Muncuk, D.R. Lewis, K.R. Chowdhury, *Design Optimization and Implementation for RF Energy Harvesting Circuits*, Journal on Emerging and Selected Topics in Circuits and Systems, Volume: 2 , Issue: 1, Page(s): 24 – 33, 2012. IEEE.

[47] Xi Shao; Bo Li;N. Shahshahan, N. Goldsman, T.S. Salter, G.M. Metze, *A planar dual-band antenna design for RF energy harvesting applications*, International Semiconductor Device Research Symposium (ISDRS), Page(s): 1 – 2, 2011. IEEE.

[48] G.P Ramesh, A. Rajan, *Microstrip antenna designs for RF energy harvesting*, International Conference on Communications and Signal Processing (ICCSP), Page(s): 1653 – 1657, 2014. IEEE.

[49] D. Pavone, A. Buonanno, M. D'Urso, F. D. Corte, *Design Considerations for Radio Frequency Energy Harvesting devices*, Progress In Electromagnetics Reaserch B, Vol. 45, 19-35, 2012.

[50] www.powercast.com

[51] F. Zhang, X. Liu, F. Meng, Q.Wu, J.C. Lee, J. F. Xu, C. Wang, and N.Y. Kim, *Design of a Compact Planar Rectenna for Wireless Power Transfer in the ISM Band*, Hindawi Publishing Corporation International Journal of Antennas and Propagat., Volume 2014

[52] T. Peter, T. A. Rahman, S. W. Cheung, R. Nilavalan, H. F. AbuTarboush, A. Vilches, *A Novel Transparent UWB Antenna for Photovoltaic Solar Panel Integration and RF Energy Harvesting*, IEEE Trans on Antennas and Propagat., Volume:PP , ISSUE: 99, 2013.

[53] Z. Popović, S. Korhummel, S. Dunbar, R. Scheeler, A. Dolgov, R. Zane, E. Falkenstein, J. Hagerty, *Scalable RF Energy Harvesting*, IEEE Trans. Microw. Theory Tech, Volume:PP , ISSUE: 99, 2013.

[54] D. Pavone, A. Buonanno, M. D'Urso, F. D. Corte, *Design Considerations for Radio Frequency Energy Harvesting devices*, Progress In Electromagnetics Reaserch B, Vol. 45, 19-35, 2012.

[55] http://www.powercast.com

[56] J. Yi, W.-H. Ki, and C.-Y. Tsui, *Analysis and Design Strategy of UHF Micro-Power CMOS Rectifier for Micro-Sensor and RFID Applications*. IEEE Transactions on Circuit and Systems, I: Regular Papers, 54(1):153–166, Jan. 2007.

[57] Z. Zhu, B. Jamali, and P. H. Cole. *Brief Comparison of Different rectifier structures for HF and UHF RFID* (Phase II). Auto-ID Labs, 2003.

[58] Decree of President of the Council of Ministers July 8, 2003.

[59] G. Bertin, B. Piovano, R. Vallauri, F. Bilotti, L. Vegni, *Metamaterial-inspired antennas for telecommunication applications*. Presented at European Conference on Antennas and Propagation (EUCAP), Annual Meeting, March, 2012

[60] E. S. Pires , G. Fontgalland , M. A. B.Melo , R. R. M. Valle , and S. E. Barbin, *Metamaterial-Inspired Wire Antennas*, IEEE Trans. On Magnetics, vol. 49, n. 5, May 2013.

[61] S. Kim, Y. Kawahara, A. Georgiadis, A. Collado, and M. Tentzeris, *Low-Cost Inkjet-Printed Fully Passive RFID Tags Using Metamaterial-inspired Antennas for Capacitive Sensing Applications*, Microwave Symposium Digest (IMS), June 2013.

[62] F. Bilotti, A. Alù, L. Vegni, *Design of miniaturized metamaterial patch antennas with -negative loading*, IEEE Trans. Antennas Propagat., vol. AP-56, no. 6, pp. 1640–1647, 2008.

[63] C. Caloz, T. Itoh, *Electromagnetic Metamaterials, Transmission Line Theory and Microwave Applications*. Hoboken-Piscataway, NJ: Wiley-IEEE Press, 2005.

[64] M. A. Antoniades and G. V. Eleftheriades, *A folded-monopole model for electrically small NRI-TL metamaterial antennas*, IEEE Antennas Wireless Propagat. Lett., vol. 7, pp. 425–428, 2008.

[65] R. W. Ziolkowski and A. Erentok, *Metamaterial-based efficient electrically small antennas*, IEEE Trans. Antennas Propagat., vol. 54, pp. 2113–2130, 2006.

[66] A. Alù, F. Bilotti, N. Engheta, and L. Vegni, *Sub-wavelength, compact, resonant patch antennas loaded with metamaterials*, IEEE Trans. Antennas Propagat., vol. 55, no. 1, pp. 13–25, 2007.

[67] R. E. Barnett, J. Liu, and S. Lazar, *A RF to DC Voltage Conversion Model for Multi-Stage Rectifiers in UHF RFID Transponders*. IEEE Journal of Solid-State Circuits, 44(2):354–370, Feb.2009.

[68] E. Bergeret, J. Gaubert, P. Pannier, and J. M. Gaultier. *Modeling and Design of CMOS UHF Voltage Multiplier for RFID in an EEPROM Compatible Process*. IEEE Transactions on Circuit and Systems, 54(10):833–837, Oct. 2007.

[69] A. Shameli, A. Safarian, A. Rofougaran, M. Rofougaran, and F. D. Flaviis, *Power Harvester Design for Passive UHF RFID Tag Using a Voltage Boosting Technique*. IEEE Transactions on Microwave Theory and Techniques, 55(6):1089–1097, Jun. 2007.

[70] T. Umeda, H. Yoshida, S. Sekine, Y. Fujita, T. Suzuki, and S. Otaka, *A 950-MHz Rectifier Circuit for Sensor Network* Tags With 10-m Distance. IEEE Journal of Solid-State Circuits, 41(1):35–41, Jan. 2006.

[71] J. Yi, W.-H. Ki, and C.-Y. Tsui, *Analysis and Design Strategy of UHF Micro-Power CMOS Rectifier for Micro-Sensor and RFID Applications,* IEEE Transactions on Circuit and Systems, I: Regular Papers, 54(1):153–166, Jan. 2007.

[72] J. F. Dickson, *On-Chip High-Voltage Generation in Integrated Circuits Using an Improved Multiplier Technique*. IEEE Journal of Solid-State Circuits, SC-11(3):374–378, Jun. 1976.

[73] G. De Vita, G. lannaccone, *Design criteria for the RF section of long range passive RFID systems*, Norchip Conference, 2003. Proceedings, pp. 107 – 110, Nov. 2003.

[74] H. Yan, J.G. Macias Montero, A. Akhnoukh, L.C.N. de Vreede, J.N. Burghart, *An Integration Scheme for RF Power Harvesting*, The 8th Annual Workshop on Semiconductor Advances for Future Electronics and Sensors, Veldhoven, Netherlands, 2005.

[75]http://www.avagotech.com/pages/en/rf_microwave/diodes/schottky/hsms.2850/

[76] Hewlett-Packard Journal, "Zero Bias Detector Diodes for the RF/ID Market, Dec. 2005.

[77] B. Razavi, *RF Microelectronics*, Prentiee Hall PTFL 1997, pp. 74-93.

[78] http://www.linear.com/product/LTC1540

[79] B. L. Pham, Anh-Vu Pham, *Triple Bands Antenna and High Efficiency Rectifier Design for RF Energy Harvesting at 900, 1900 and 2400 MHz* ,Microwave Symposium Digest (IMS), IEEE, 2013.

[80] http://en.m.www.wikipedia.org/wiki/Photovoltaic_effect , 2015.

[81] J. Shadrach Roundy, *Energy Scavenging for Wireless Sensor Nodes with a Focus on Vibration to Electricity Conversion*, Berkeley 2003

[82] *Solar cells efficiency tables version 36* http://onlinelibrary.wiley.com/doi/10.1002/pip.1021/pdf

[83] T. Huang, J. Jiang, Y. Hsiao, C. Chen, *Maximum power tracking for photovoltaic power systems*, Tamkang Journal of Science and Engineering, 8:147–153, 2005.

[84] http://www.ixys.com/ProductPortfolio/GreenEnergy.aspx# , 2015.

[85] www.linear.com/product/LTC3105 , 2015.

[86] www.linear.com/product/LTC3108, 2015.

[87] H. Mosallaei, K. Sarabandi, *Novel artificial reactive impedance surface for miniaturized wideband planar antenna design: concept and characterization*, Antennas and Propagation Society International Symposium, 2003. IEEE , vol.2, no., pp. 403- 406 vol.2, 22-27 June 2003.

[88] L. Ukkonen, L. Sydanheimo, M. Kivikoski, *Patch antenna with EBG ground plane and two-layer substrate for passive RFID of metallic objects*, Antennas and Propagation Society International Symposium, 2004. IEEE , vol.1, no., pp. 93- 96 Vol.1, 20-25 June 2004.

[89] J. Liang, *Analysis of a Proximity Coupled Patch Antenna on a Metalized Substrate*, Antennas and Propagation Society International Symposium 2006, IEEE , vol., no., pp.2287-2290, 9-14 July 2006.

[90] Y. Alvarez, R.C. Hadarig, F. Las-Heras, *Novel SHF-Band Uniplanar Artificial Magnetic Conductor*, Antennas and Wireless Propagation Letters, IEEE , vol.9, no., pp.44-47, 2010.

[91] J. R Sohn, K. Y. Kim, H.-S. Tae, *Comparative study on various artificial magnetic conductors for low-profile antenna*, Progress In Electromagnetics Research, PIER 61, 27-37, 2006.

[92] L. Calhau, P. Pinho, *Low profile multi-band antenna for mobile communications*, Antennas and Propagation (EuCAP), 2010 Proceedings of the Fourth European Conference on , vol., no., pp.1-4, 12-16 April 2010.

[93] F. Grange, C. Delaveaud, K. Madhjoubi, *Miniaturization of artificial magnetic conductors,* Antennas and Propagation Society International Symposium (APSURSI), 2010 IEEE , vol., no., pp.1-4, 11-17 July 2010.

[94] F. Biliotti, *Esempi di progetto di antenne a patch per terminali*, Roma Tre, 2006.

[95] M. Hossein, S. Kamal, *Antenna Miniaturization and Bandwidth Enhancement Using a Reactive Impedance Substrate*, IEEE Transcations on Antennas and Propagation, Vol.52, n.9, September 2004.

[96] A. Quach, K. Lo, *Automatic target detection using a ground-based passive acoustic sensor*, Proceedings of the 1999 Conference on Information, Decision and Control , pp. 187–192, 1999.

[97] A.M. Zoubir, V. Koivunen, Y. Chakhchoukh, and M. Muma, R*obust Estimation in Signal Processing",* IEEE Signal Processing Magazine, Jul. 2012.

[98] G. Succi, G. Prado, R. Gampert, T. Pedersen, and H. Dhalival, *Footstep Detection and Tracking*, *Proceedings of SPIE*, 4393, pp.22-29, April 2001.

[99] Urick, *Principles of Underwater Sound*, McGraw Hill, 1967.